Magneto-optical tweezers with super-resolution fluorescence microscopy

Zhaokun Zhou

Doctor of Philosophy

University of York
Physics
June 2017

Abstract

This thesis describes the design, construction and application of a novel magneto-optical tweezers with super-resolution fluorescence microscopy for manipulation, force/torque measurement and imaging of single biomolecules. The optical tweezers component offers force or position clamping in three dimensions. The 3D-printed magnetic tweezers is designated for rotation in the vertical plane. The separation of rotation from force transduction results in the capability of precise torque measurement. The filamentous biomolecules to be used in the device will lie in a transverse direction in the imaging plane to allow fluorescence imaging with techniques including Blinking assisted Localisation Microscopy (BaLM) and total internal reflection fluorescence microscopy (TIRF). Also included are features such as acousto-optic deflection and multiplexing of laser traps, interferometry based tracking with quadrant photodiode and piezoelectric actuated nanostage for active feedback. These tweezers have been developed to enable direct observation of molecular topological transformation and protein binding event localisation with mechanical perturbation, which traditional tweezers could not achieve.

Contents

List of Figures

List of Tables

List of publications

List of published journal articles stemming from my PhD work

- Miller, Helen, Zhaokun Zhou, Adam JM Wollman, and Mark C. Leake. "Superresolution imaging of single DNA molecules using stochastic photoblinking of minor groove and intercalating dyes." *Methods* 88 (2015): 81-88.
- Wollman, Adam JM, Helen Miller, Zhaokun Zhou, and Mark C. Leake. "Probing DNA interactions with proteins using a single-molecule toolbox: inside the cell, in a test tube and in a computer." *Biochemical Society Transactions* (2015): 139-145.
- Zhou, Zhaokun, Helen Miller, Christoph Baumann, and Mark C. Leake. "Combined Magneto-Optical Tweezers and Super-Resolution Fluorescence Imaging for Probing Dynamic Single-Molecule Topology of DNA, and Protein Machines that Manipulate DNA Topology." *Biophysical Journal* 110, no. 3 (2016): 499a.

List of published book chapters

- Zhou, Zhaokun, and Mark C. Leake. "Force spectroscopy in studying infection." *Biophysics of Infection*, pp. 307-327. Springer International Publishing, 2016.

List of journal articles under review

- Miller, Helen, Zhaokun Zhou, Jack Shepherd, Adam JM Wollman, and Mark C. Leake. "Single-molecule techniques in biophysics: a review of the progress in methods and applications." *arXiv preprint arXiv*:1704.06837 (2017).

List of posters

- Zhaokun Zhou, Christoph Baumann and Mark C. Leake. "Transverse magnetic tweezers and optical tweezers with nanoscale fluorescence imaging to visualize activities on single DNA molecules." Poster presented at: Microscience Microscopy Congress 2014 of the Royal Microscopy Society; 2014 June 30 - July 1; Manchester, UK
- Zhaokun Zhou, Helen Miller, Adam JM Wollman and Mark C. Leake. "Magneto-optical tweezers and superresolution fluorescence imaging for probing dynamic single-molecule topology of DNA, and protein machines that manipulate DNA topology." Poster presented at: Second Year Postgraduate Conference of the University of York; 2015 February 15; York, UK
- Zhaokun Zhou, Christoph Baumann and Mark C. Leake. "Combined magneto-optical tweezers and superresolution fluorescence imaging for probing dynamic single-molecule topology of DNA, and protein machines that manipulate

DNA topology." Poster presented at: Biophysical Society 60th Annual Meeting of the Biophysical Society, February 27 - March 2; Los Angeles, USA

- Zhaokun Zhou, and Mark C. Leake. "Force spectroscopy in studying infection" Poster presented at: Winter BPSI Symposium of the Biological Physical Sciences Institute; 2016 December 1; York, UK

List of List of invited conference talks

- Zhaokun Zhou, Christoph Baumann and Mark C. Leake. "Transverse magnetic tweezers and optical tweezers with nanoscale fluorescence imaging to visualize activities on single DNA molecules." Talk given at: Microscience Microscopy Congress 2014 of the Royal Microscopy Society; 2014 June 30 - July 1; Manchester, UK

Acknowledgements

I would like to express my sincere gratitude to my supervisor Professor Mark Leake for the continuous support of my PhD study, for his patience and encouragement. His guidance has been helpful throughout research and the writing of this thesis. I could not have imagined having a better supervisor and mentor for my PhD study. I also thank Dr Christoph Baumann and Dr Stephen Cross for the detailed technical support they gave me. I drew many of my flashes of inspiration from their advices.

Jack Shepherd was often the only other person present in the lab, which allowed me precious human interaction during lab time. The many hours in the window-less lab would have been much less entertaining if it were not for him. Helen Miller pushed through the first several experiments in my PhD with me, when I was new to the trade and was pretty clueless, which is of immense value to me. Dr Adam Wollman tirelessly helped me with any issues I had in research. Many a time Jack Shepherd and I would ask him rather than Googling a question. Dr Erik Hedlund's allergy to walnuts and normality kept me amused and high-spirited for years. So THANK YOU all!

I am grateful to the University of York and the Biological Physical Sciences Institute for funding my study at the University of York. I also would like to show my gratitude for receiving stipendiary funding in my final months of PhD from the Research Councils UK and Wellcome Trust.

Declaration

I declare that this thesis is a presentation of original work and I am the sole author. This work has not previously been presented for an award at any university. All sources are acknowledged as references. I am solely responsible for all the research work described in this thesis except for the following collaborations:

- In section 2.3, the bead height was jointly measured by Jack Shepherd and myself. The correction module was solely assembled by Jack Shepherd.
- In chapter 4, the excitation and emission optics were solely constructed and tested by Helen Miller and the fluorescence imaging experiments were jointly conducted by Helen Miller and myself.
- In chapter 4, the ADEMS code used for the analysis of the image data was solely written by Adam Wollman and the analysis was performed by Adam Wollman and Helen Miller.
- In chapter 4, the excitation beam was re-walked by Jack Shepherd to co-align the laser trap.

Chapter 1

Introduction

Force spectroscopy in the context of single molecule biophysics refers to the class of technologies that allow the mechanical manipulation of single biological molecules. Examples include optical tweezers, magnetic tweezers, atomic force microscopy, flow manipulation and micro-pipette manipulation.

This thesis describes the development of bespoke magneto-optical tweezers for the manipulation of axial biological molecules such as DNA and microtubules with added super-resolution microscopy capabilities.

This chapter discusses the need for force spectroscopy in the investigation of biological molecules, particularly their mechanical and dynamic properties. Then the physics of spectroscopy is briefly described. Finally, the magneto-optical tweezers are introduced in more detail.

1.1 Biological motivation

In this section I discuss the need for single molecule techniques to interrogate molecular biology and the need for spectroscopy tools in studying molecular forces, the motion of motor proteins and the elastomechanical properties of biological polymers. Since the magneto-optical tweezers arising from this PhD has the added capability of super-resolution fluorescence microscopy, the need for such microscopy will also be explained.

1.1.1 Single *vs* ensemble measurement

Single molecule techniques measure or manipulate biomolecules individually, either one at a time or several in parallel, but even in the latter case the resolution is at a single molecule level. This is in contrast with ensemble methods to determine the molecular structures of biological macromolecules, which act on a collection of the same molecules arranged in patterns to form an object large enough for bulk measurements. The two most used ensemble methods are X-ray crystallography [1] and nuclear magnetic resonance (NMR) spectroscopy [2]. Although ensemble methods are excellent and, in some cases, the only methods to determine the structure and function of many biological molecules, they are averaging-based so they are intrinsically unable to measure the heterogeneity in biomolecules. Also, molecules are removed from their cellular context and packed in a periodic pattern or spread uniformly in a solution so time-dependent interactions with

other molecules cannot be characterised. On the other hand, experiments with single molecule methods are performed in conditions much closer to native cellular environments with the molecules allowed to interact with other functional groups. Step-wise events, molecular navigation in the cell, heterogeneity and rare events can thus be observed.

1.1.2 The role of forces in the cell

Many molecular biological activities are mechanical in nature so they are suitably investigated from the perspective of forces. As a few examples of molecular forces, myosin is a motor protein that pulls against actin filaments to cause muscle contraction [3]; kinesin, another motor protein, carries cellular cargos and walks along microtubule [4, 5]; when DNA replicates, the coiling of the double helix builds up due to the unzipping of the double strands, which topoisomerases uncoils by introducing negative twists [6, 7]; ATP synthase creates ATP from ADP by rotating its gamma subunit [8]. In the investigation of molecular forces, spectroscopy is able to measure the forces exerted by individual molecules thus providing a description of the magnitude of interactions in catalytic cycles. In addition, controlled perturbations can be applied to disrupt the native molecular interactions for further interrogation.

Molecular motions are another phenomenon that is found in many biological processes including the transportation of cellular cargos and muscle contraction. They are all driven by forces so the two are closely related. Force spectroscopy tools are equipped with high resolution imaging modules to allow the monitoring of movement. Specialised transducers combined with a laser as the light source can reach Angstrom level precision, which enables the monitoring of small step-size motions such as those of DNA and RNA processing proteins [9–11]. The knowledge of movement step-sizes, speed, direction and pauses allows the modelling of motor molecule action mechanisms.

Another focus of research is the elastic properties and conformational changes of long molecules such as DNA. Notable force/torque application experiments in the literature include the force-extension curve of B-DNA [12, 13], structural changes when the DNA is overstretched [14, 15] and plectoneme formation [16–18]. Stretched and positively/negatively supercoiled DNA also natively exist as a result of local confinement of DNA and DNA-protein interactions where forces and torques from the proteins change DNA from their relaxed conformations [19–21]. Investigations of protein-induced DNA-conformational changes include DNA wrapping around histones [22, 23], DNA bridge formation [24], DNA helicase separating double strands [25, 26], topoisomerase unwinding supercoils [6, 7] and so on.

1.1.3 Super-resolution fluorescence microscopy

Super-resolution fluorescence microscopy is a light microscopy technique that achieves resolutions beyond the diffraction limit of wide field optical microscopy of approximately 200-700 nm, which is above the dimension of some subcellular structures and all biomolecules. In general, this method uses fluorophores to label biomolecules in question. Fluorophores absorb excitation light, which excites orbital electrons in the fluorophores, and emit light of longer wavelengths upon the falling of the electrons back into their ground state. Fluorophores are chosen or engineered so that excitation and emission lights

are of narrow wavelength windows offset from each other so that dichroic filters can be used to stop excitation and background light outside the emission band from reaching the camera. Methods to harness fluorophores bring imaging resolution about 10 times better than classical microscopy. Some examples of them are near-field scanning optical microscopy (NSOM) [27, 28], stimulated emission depletion (STED) microscopy [29–33], reversible saturable optical linear fluorescence transitions (RESOLFT) microscopy [34, 35], saturated structured-illumination microscopy (SSIM) [36], stochastic optical reconstruction microscopy (STORM) [37], photoactivated localization microscopy (PALM) [38], fluorescence photoactivation localization microscopy (FPALM) [39], binding-activated localization microscopy (BALM) [40], and bleaching/blinking assisted localization microscopy (BaLM) [41], Förster resonance energy transfer (FRET) [42], fluorescence recovery after photobleaching (FRAP) [43, 44], and fluorescence loss in photobleaching (FLIP) [45]. These techniques can potentially be used in combination with the tweezers setup but only the ones used in my work will be described in detail in later chapters. Imaging is a direct and sometimes the only method to probe the biology studied with force spectroscopy. For example, in DNA supercoiling, non-imaging experiments infer the formation of plectonemes through the shortening of the DNA, which can be measured with the displacement of the probe bead. However, no information is obtained regarding the position, shape, size, number and dynamics of loops. Fluorescently tagging the DNA contour has proved to be able to yield some of the lacking information [46] and my effort is in developing further the chimera of super-resolution imaging with innovative force spectroscopy instruments.

1.1.4 DNA

DNA, or deoxyribonucleic acid, will be the molecule of main research focus with the instrument arising from this PhD project. Many design features of the instrument are aimed specifically at interrogating the mechanical, dynamical properties of DNA as well as the interaction of DNA with proteins or other DNA. Therefore I include known facts about topological and mechanical properties of DNA here.

Naturally-occurring DNA molecules are a polymer formed by joining a sequence of deoxyribonucleoside triphosphates (dNTPs): deoxyadenosine triphosphate (dATP), deoxyguanosine triphosphate (dGTP), deoxycytidine triphosphate (dCTP) and deoxythymidine triphosphate (dTTP), whose molecular formulae are shown in figure 1.1 (a). These nucleotides are joined to their neighbours by ester bonds between the sugar base of one nucleotide and the phosphate group of the adjacent nucleotide. See figure 1.1 (b) for an example of a phosphodiester bond joining a dATP and a dGTP. A double stranded DNA (dsDNA) molecule is formed by two linear sugar-phosphate backbones that twist around each other in a helical shape along a common axis. The nucleotides in one strand are paired up with the nucleotides in the other strand with dATP matched to dTTP and dGTP matched to dCTP, bonded by double or triple hydrogen bonds respectively to stabilise the dsDNA, which are negatively charged due to the formation of the phosphodiester bond - see figure 1.1 (b) for the negative charge on the oxygen atom. For an isolated dsDNA in an aqueous environment, the repulsion due to the like charges and the attraction from the hydrogen bonds are in a constant tug of war. High temperature makes it energetically favourable for the dsDNA to unwind and separate into single-stranded DNA (ssDNA).

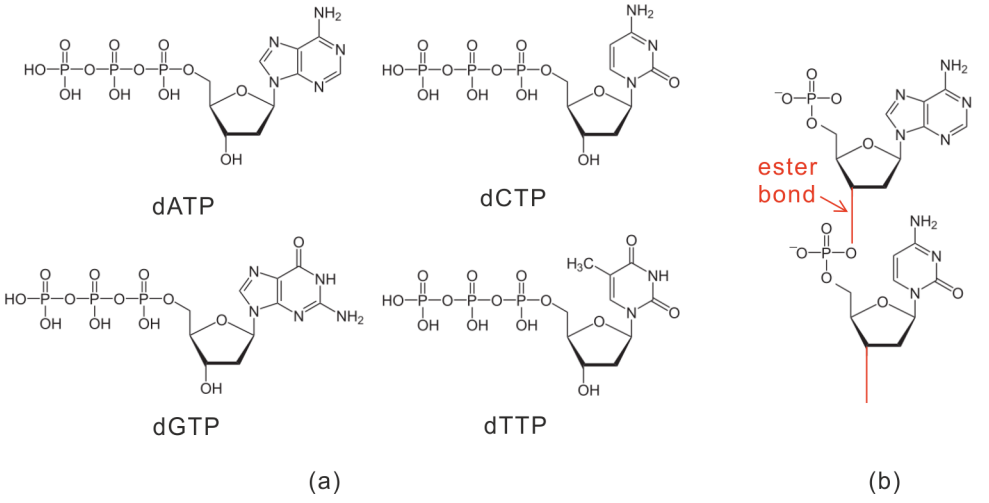

Figure 1.1: (a) Chemical composition of dATP, dGTP, dCTP and dTTP. (b) The ester bond is formed when the hydroxyl group in phosphoric acid reacts with the hydroxyl group on the sugar. Is is highlighted in red. Two of the ester groups form a phosphodiester bond.

When half of the DNA strands are in the ssDNA state, the temperature is called the melting temperature (T_m). CG content (the percentage of dGTP and dCTP among all dNTPs in the DNA) affects T_m as a CG pair (the pair of nucleotides formed by dGTP and dCTP) has three hydrogen bonds (so stronger) whereas an AT pair has two. Thus, a high GC content increases T_m. Salt concentration also affects the melting temperature because the positive ions from the salt shield the negative charges on the phosphates and reduce repulsion. Thus, in high salt, a given DNA will melt at a higher temperature than in a lower salt concentration. Assuming 50 nM dsDNA, 50 mM NaCl, and pH 7.0, the approximate expression for T_m for sequences with fewer than 14 base pairs is (the Wallace rule [47]):

$$T_m = 2(A+T) + 4(G+C) \tag{1.1}$$

where A, T, G, C are the number of the bases dATP, dTTP, dGTP and dCTP in the sequence respectively and T_m is in degree Celsius. For sequences longer than 15 base pairs,

$$T_m = 64.9 + 41 \times (G+C-16.4)/(A+T+G+C) \tag{1.2}$$

The dsDNA have a diameter of 22 to 26 Angstroms. Each nucleotide pair has a height of 3.3 Angstroms along the axis of the DNA. The double helical strands have spaces between them called grooves. The strands are not symmetrical so the grooves are unequally sized. In B form dsDNA, the larger groove is 22 Angstroms wide whereas the smaller groove is 12 Angstroms wide [48]. These grooves provide a space for proteins that process DNA to bind to the base pairs and they also allow artificial fluorophores to attach to the stands. For example, minor groove binding dyes include DAPI [49], SYBR Green I [50] and the Hoechst dyes [51], etc. Major groove binding dyes include methyl green [52] etc. For completeness, I also mention here dyes that bind to other places on the DNA: intercalating dyes (eg. ethidium bromide and propidium iodide) bind between adjacent pairs of nucleotides; external binder to the side of the DNA and bis-intercalator to two adjacent base-pair gaps. See figure 1.2 (a) for an illustration of all these dyes.

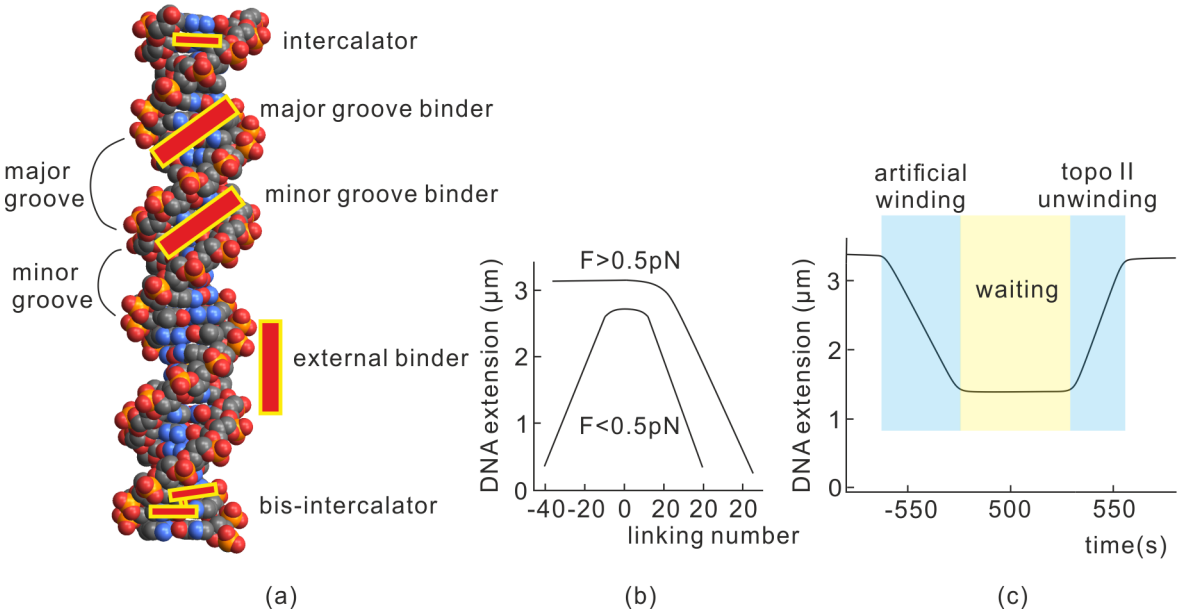

Figure 1.2: (a) A B-DNA molecule with random sequence to show the major and minor grooves and where major- and minor-groove binding dyes will attach to the DNA. For completeness, other types of dyes are also illustrated: intercalators, external binders and bis-intercalators. The atomic positions are generated with 3D-DART [53] to which a random sequence is supplied. (b) DNA extension as a function of linking number (the number of times a strand of DNA winds in the right-handed direction around the helix axis) introduced into the DNA. At a pulling force <0.5 pN, when linking number is above 5 or under -5, plectonemes (loops of helices) form and the DNA extension reduces at higher speed [7]. At high force, the negative supercoiling denatured the DNA so no reduction in DNA extension is recorded. (c) DNA extension is reduced by introducing twists into the DNA. Then, after a while, topoisomerase II is introduced and the supercoiling is undone.

DNA exist either as a linear or a circular polymer *in vivo*. Circular DNA are ones whose tail joins their head to form a closed loop, which are found in viral genomes [54] and bacterial plasmids [55]. Linear DNA usually wrap around histones, which (in eukaryotic cell nuclei) package the DNA into compact structures so the DNA take up minimum volume and are ordered. As a result, both linear and circular DNA are torsionally constrained in the sense that twists introduced locally into the DNA by proteins or other sources will not dissipate out of the DNA but result in the DNA supercoiled. A torsionally relaxed DNA (a DNA that has no angular strain in the double strands) circle the axis of the double helix once every 10.4 base pairs. When twists are introduced, the DNA become more tightly or more loosely wound. The former is termed positive supercoiling and the latter negative supercoiling.

DNA supercoiling sees functions in genome packaging and gene expression. The former mainly involves compacting the long DNA into a spatially minimised structure so can be contained in the cell, which is often orders of magnitude smaller than the extent of the DNA. This packing and wrapping around histones also mean processes such as DNA replication or transcription that require locally uncoiling and separating double strands will result in building-up of positive supercoiling in the vicinity. These are relaxed by enzymes such as

topoisomerases to allow the action to continue. In gene expression, the CG content affects the DNA's response to supercoiling, which in turn affects the speed of protein read-out and this may be a means to regulate gene expression [56].

The mechanical properties of DNA and the interaction between DNA and proteins have been extensively studied with spectroscopy. From the stretching and melting of DNA under tension to super- and under-coiling under tension [7]. When the DNA molecule is stretched, the force-extension curve can be approximately described with the worm-like-chain model [57,58] - see figure 1.3 (f), and the expression below:

$$\frac{FA}{kT} = \frac{1}{4}(1 - x/L)^{-2} - \frac{1}{4} + x/L \tag{1.3}$$

where $A \approx 50\,\mathrm{nm}$ is the persistence length. If the stretching force exceeds ~65 pN, three phenomena co-exist: peeled ssDNA, melting bubbles, and S-DNA. These are observed with fluorescence microscopy [14] and single molecule calorimetry [15].

1.2 Physics of spectroscopy

This section introduces the physics underlying optical and magnetic tweezers. For completeness, the physics of other spectroscopy tools will also be briefly mentioned.

1.2.1 Photonic force and torque

All forces and torques in spectroscopy are electromagnetic in nature. Optical tweezers transduce force through the fact that photons carry linear and angular momenta. When photons are reflected, deflected or absorbed by an object, their momenta transfer to the object, resulting in a force/torque applied on the object. The radiation force $\mathbf{F}_{OT}$ exerted on a fully reflective surface is [59]

$$\mathbf{F}_{OT} = 2\frac{P}{c}\hat{\mathbf{n}} \tag{1.4}$$

where P is the power of the light, c is the speed of light in vacuum and $\hat{\mathbf{n}}$ a unit vector in the direction of the force. This sets the upper limit of radiation force. Multiple methods can be used for optical torque transduction [60] but, similarly to force application, all utilise the transfer of angular momentum from light to the particle with conservation of momentum as the principle. As an example method, if a light beam shines on a birefringent probe, the electric field $\mathbf{E}$ in the light wave induces a polarisation $\mathbf{P}$ in the probe. Any misalignment between $\mathbf{E}$ and $\mathbf{P}$ will cause a torque $\boldsymbol{\tau}_{OT}$ [61]:

$$\boldsymbol{\tau}_{OT} = \int d^3x \mathbf{P} \times \mathbf{E} \tag{1.5}$$

1.2.2 Magnetic force and torque

The idea of magnetic forces is similar to that of optical forces but the concept is more straightforward. Magnetic tweezers use a magnetic field $\mathbf{B}$ to manipulate a magnetised probe. The magnetic force $\mathbf{F}_{MT}$ is proportional to and in the direction of the field gradient [62] and the torque $\boldsymbol{\tau}_{MT}$ aligns and scales with the field itself [63]:

$$\mathbf{F}_{MT} = (\mathbf{M_b} \cdot \nabla)\mathbf{B} \tag{1.6}$$

$$\boldsymbol{\tau}_{MT} = \alpha m_b |\mathbf{M}| \hat{\mathbf{p}} \times \mathbf{B} \cos\theta \tag{1.7}$$

where α is the constant of proportionality that quantifies the magnetisation along the preferential axis, m_b is the mass of the magnetic bead, $\mathbf{M}$ is the magnetisation per unit mass, $\hat{\mathbf{p}}$ is the direction of the preferential axis and θ is the angle between the magnetisation along the preferential axis and the background magnetic field. See equations 3.8 and 3.9 for more details. Figure 1.5 (a) and (b) depict force and torque transduction onto a magnetised bead. Both can be applied at the same time if the bead is in a misaligned field with a nonzero gradient. The probe is tethered to the biomolecule so any manoeuvring of the probe is passed to the molecule. Another category of tools is the electric equivalent of magnetic tweezers in which electric field is used to manipulate probes with dielectric properties [64, 65]. Mechanical forces have also been used in the cases of micro-needle manipulation [66] and flow-induced stretching [67]. The combination of Van der Waals attraction and Coulomb repulsion has been harnessed in the case of atomic force microscopy (AFM) [68, 69]. More recently, liquid vibration driven by standing sound waves has shown to trap and sort microspheres, which gives rise to acoustic tweezers [70–74].

1.3 Optical tweezers (OT)

This section describes the optical system design common to most optical tweezers as well as bespoke designs, then a few high profile experiments using OT, and finally the calibration of OT. Some aspects of the calibration directly relevant to designing and calibrating my design are left to chapter 2 where my optical tweezers are described.

1.3.1 Design of OT

Optical tweezers are formed when a high numerical aperture (NA) objective lens focuses a collimated laser beam to a diffraction limited spot, which has a potential energy minimum for the trapped object along the optical axis and slightly downstream of the focus. Figure 1.3 (a) shows a basic laser tweezers setup in which the collimated beam slightly overfilling the objective entrance pupil is formed with a telescope beam expander. The light then passes through the condenser and eventually images on a QPD (quadrant photodiode) to allow bead position information to be extracted (more on bead tracking below). Figure 1.3 (b) shows the bead in the equilibrium as well as displaced positions with respective net forces applied on the bead. Ray optics are used for the gradient and scattering forces analysis. Three rays in each case are selected and the force due to each ray marked with a black arrow. Full analysis can be found in [75, 76]. One can move the bead by moving the laser focus. Near infra-red (NIR) lasers usually serve as the light source as they cause less photodamage to biological molecules compared to visible wavelength light due to less heat absorption and less oxygen-species free radical creation (although heat absorption in water is higher) [77]. Bespoke OT make modifications that improve specific aspects of trapping. For example, top-hat [75] and doughnut shaped (Laguerre-Gaussian mode [78]) beams [79] can replace Gaussian profile beams to increase the trapping stiffness along the axial direction, which, without this modification, is lower than the lateral stiffness. Another modification is using Bessel beams [80], which has self-healing property [81], to form a tunnel trap so multiple traps stack axially for high-throughput experiments [82] and bead

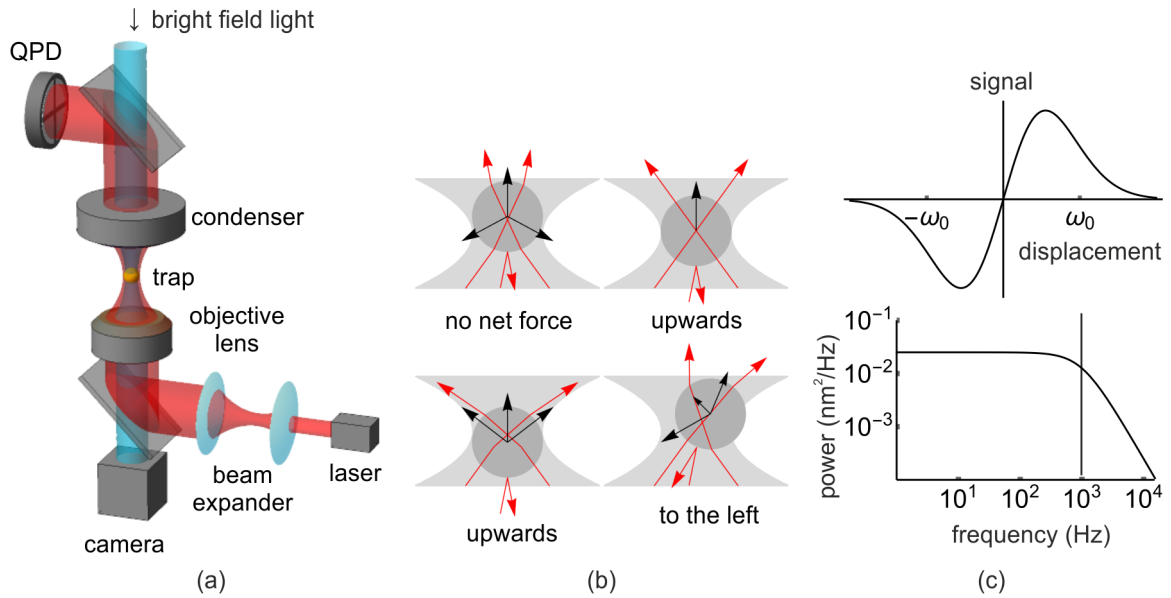

Figure 1.3: Optical tweezers setup, mechanism and calibration. (a) The optical diagram of OT with only key functioning parts shown. The laser is expanded with a pair of positive lenses (the beam expander). The objective focuses the laser to a diffraction limited spot, which traps the bead. The condenser re-collimates the emerging beam and the quadrant photodiode (QPD) images the beam, which is used for interferometry tracking of the bead. (b) Forces on the bead due to the position of the bead. Analysis in this instance is based on ray optics. Red arrows are representative rays. Two refracted and one reflected rays are selected in each case. Black arrows are forces due to the selected rays. (c) Upper panel: the QPD signal due to displacement of the bead along one axis from its equilibrium position [93]. ω_0 is the $1/e$ radius of the waist. The relationship is approximately linear near the origin. Lower panel: the power spectrum density of the time trace of a trapped bead. The corner frequency is labelled with a vertical line on the Lorentzian curve.

assembly and movement [83, 84]. Other extensions include optical torque tweezers to rotate the bead [85], holographic optical tweezers to trap massive number of beads [86] and sorting [87] and arranging materials [88, 89]. More recent developments include lab-on-a-chip (LOC) optical tweezers, which is a miniature portable optical tweezers potentially having clinical uses. In LOC OT, dielectric nanostructures shape the light to form the trap rather than a high NA objective lens so flexibility is compromised for portability [90–92].

1.3.2 Interferometry tracking with QPD

Interferometry is the method of choice for bead position measurement. The trapping laser or a separate tracking laser (almost coinciding the trapping laser) can be used. The part of the laser light that passes the bead unaffected by it and the part which is scattered by the bead interfere to form an interference pattern at the back focal plane of the condenser. An imaging lens projects this pattern onto a quadrant photodiode (QPD). Any movement of the trapped bead relative to the trap centre will cause shifts in the interference pattern. Figure 1.3 (a) depicts the arrangement of optical components with the imaging lens omitted. A QPD is a 2×2 array of photodiodes. It outputs three voltage signals: (1) V_{TB} is the

difference between the top two photodiodes and the bottom two, effectively quantifying the vertical positioning of the impinging light; (2) V_{LR} is the difference between the left two and right two photodiodes, quantifying the horizontal positioning; (3) V_{SUM} is the total of the four photodiodes. The reason for using QPD to track the bead rather than a camera is QPD's high temporal resolution - its bandwidth is (the frequency at which the response drops to 50% of its value at DC) typically higher than 10 kHz, capturing high frequency motion due to Brownian force. QPD also has high sensitivity, which allows Carter et al. to stabilise their microscope stage to 0.1 nm [94]. The high resolution of QPD allows the calibration of the trap using interferometry.

1.3.3 Calibration of OT: the equipartition theorem method

The region close to the trap centre can be modelled as having a parabolic energy potential along all three spatial dimensions. The bead is then treated as being attached to Hookean springs in a thermal bath. Calibration of the trap involves evaluating the stiffness, k, of the spring. The equipartition theorem method is introduced in this section.

Equating spring potential energy with kinetic energy in one direction (the equipartition theorem says that kinetic energy in one direction is one-third the total kinetic energy):

$$\frac{1}{2}k < x(t)^2 >= \frac{1}{2}k_B T \tag{1.8}$$

where k_B is Boltzmann's constant, T is the absolute temperature and $< x(t)^2 >$ is the mean value of $x(t)^2$ measured over a long period of time τ:

$$< x(t)^2 >\equiv \lim_{\tau\to\infty} \frac{1}{\tau} \int_{-\tau/2}^{\tau/2} x(t)^2 dt \tag{1.9}$$

Rearrange equation 1.8 to get the trap stiffness:

$$k = \frac{k_B T}{< x(t)^2 >} \tag{1.10}$$

Since the QPD signals are electric voltage, they need to be converted to displacement. A look-up-curve is established experimentally and its expected shape is shown in Figure 1.3 (c) top panel with the theoretical expression [93]

$$\frac{V_{LR}}{V_{SUM}} \approx \frac{16}{\sqrt{\pi}} \frac{k'\alpha}{\omega_0^2} \exp(-2(x/\omega_0)^2) \int_0^{x/\omega_0} \exp(y^2) dy \tag{1.11}$$

where k' is the wavenumber, α a constant and ω_0 is the $1/e$ radius of the waist (ω_0 at other places in this thesis has different meanings).

Physically, the above equipartition theorem method relates the trap stiffness to the mean vibrational amplitude of the bead: trapped in the parabolic potential and bombarded by water molecules, the bead jiggles. The stronger the trap, the less the amplitude of the jiggling and vice versa. The drawback of this method is its inability to exclude irrelevant energy sources that affect the bead displacement signal, such as acoustic noise and instrumental drift. The power spectrum method introduced below elegantly excludes them.

1.3.4 Calibration of OT: the power spectrum method

An alternative method to calibrate the OT is by converting the displacement signals into the frequency domain and fitting the power spectrum to the theoretical curve, from which one can read out the trap stiffness. The bead motion is given by the Langevin Equation:

$$m\ddot{x} + \gamma\dot{x} + kx = F(t) \tag{1.12}$$

where γ is the hydrodynamic drag coefficient ($\gamma = 6\pi\eta r$, where η is the viscosity of the medium and r the radius of the bead) and $F(t)$ is the Langevin force. The power spectrum of such a bead approximately follows a Lorentzian distribution, the definition of which is quoted below:

$$L(x) = \frac{1}{\pi}\frac{\frac{1}{2}\Gamma}{(x - x_0)^2 + (\frac{1}{2}\Gamma)^2} \tag{1.13}$$

The formulations that follow have all been deduced previously (for example see [95]) but I include them here for completeness. We obtain the power spectrum for the trapped bead by applying Fourier transform to equation 1.12:

$$(-m\omega^2 + i\gamma\omega + k)x(\omega) = F(\omega) \tag{1.14}$$

The following theorem has been used to obtain equation 1.14:

$$\mathcal{F}\left\{\frac{d^n x(t)}{dt^n}\right\} = (i\omega)^n x(\omega) \tag{1.15}$$

Define $\omega_0 \equiv \sqrt{\frac{k}{m}}$ and $\beta \equiv \frac{\gamma}{m}$ and rearrange equation 1.14:

$$(\omega_0^2 - \omega^2 + i\beta\omega)x(\omega) = \frac{F(\omega)}{m} \tag{1.16}$$

$$|x(\omega)|^2 = \frac{|F(\omega)|^2/m^2}{(\omega_0^2 - \omega^2)^2 + \beta^2\omega^2} \tag{1.17}$$

The one-sided power spectral density is defined as:

$$\text{PSD}(x, \omega) \equiv \lim_{\tau\to\infty}\frac{1}{\tau}2|x(\omega)|^2 \tag{1.18}$$

Substitute equation 1.17 into 1.18:

$$\text{PSD}(x, \omega) \equiv \lim_{\tau\to\infty}\frac{1}{\tau}2\frac{|F(\omega)|^2/m^2}{(\omega_0^2 - \omega^2)^2 + \beta^2\omega^2} \tag{1.19}$$

We next need to express the Brownian force term $|F(\omega)|^2$ in terms of measurables, such as temperature and bead diameter. First, integrate PSD w.r.t. ω. Since $|F(\omega)|^2$ is uniform over

the whole frequency range, it can be dragged out of the integration sign:

$$\int_0^\infty \text{PSD}(x,\omega)d\omega = \lim_{\tau\to\infty}\frac{1}{\tau}\frac{|F(\omega)|^2}{m^2}\int_0^\infty 2\frac{1}{(\omega_0^2-\omega^2)^2+\beta^2\omega^2}d\omega \tag{1.20}$$

$$= \lim_{\tau\to\infty}\frac{1}{\tau}\frac{|F(\omega)|^2}{m^2}\int_{-\infty}^\infty \frac{1}{(\omega_0^2-\omega^2)^2+\beta^2\omega^2}d\omega \tag{1.21}$$

$$= \lim_{\tau\to\infty}\frac{1}{\tau}\frac{|F(\omega)|^2}{m^2}\frac{\pi}{\beta\omega_0^2} \tag{1.22}$$

Then, associate the integrated PSD with the variance of the displacement and thus temperature and spring constant:

$$\int_0^\infty \text{PSD}(x,\omega)d\omega = \lim_{\tau\to\infty}\frac{1}{\tau}\int_0^\infty 2|x(\omega)|^2 d\omega \tag{1.23}$$

$$= \lim_{\tau\to\infty}\frac{1}{\tau}\int_{-\infty}^\infty |x(\omega)|^2 d\omega \tag{1.24}$$

$$= 2\pi\lim_{\tau\to\infty}\frac{1}{\tau}\int_{-\tau/2}^{\tau/2} |x(t)|^2 dt \tag{1.25}$$

$$= 2\pi < x(t)^2 > \tag{1.26}$$

$$= 2\pi\frac{k_BT}{k} \tag{1.27}$$

Equation 1.25 is obtained with Parseval's theorem:

$$\int_{-\infty}^\infty |x(t)|^2 dt = \frac{1}{2\pi}\int_{-\infty}^\infty |X(\omega)|^2 d\omega \tag{1.28}$$

and equation 1.27 is from equation 1.8. Equation 1.22 and 1.27 combine to give:

$$\lim_{\tau\to\infty}\frac{1}{\tau}\frac{|F(\omega)|^2}{m^2}\frac{\pi}{\beta\omega_0^2} = 2\pi\frac{k_BT}{k} \tag{1.29}$$

$$\Rightarrow \lim_{\tau\to\infty}\frac{1}{\tau}\frac{|F(\omega)|^2}{m^2} = 2\pi\frac{k_BT}{k}\frac{\beta\omega_0^2}{\pi} = \frac{2k_BT\beta}{m} \tag{1.30}$$

Substitute 1.30 into 1.19 to get the final expression for PSD:

$$\text{PSD}(x,\omega) = \frac{2k_BT\beta}{m}2\frac{1}{(\omega_0^2-\omega^2)^2+\beta^2\omega^2} \tag{1.31}$$

The bead has a low Reynolds number, so the inertial term can be neglected. Equation 1.12 simplifies to:

$$\gamma\dot{x} + kx = F(t) \tag{1.32}$$

Following the same reasoning as above, the PSD for equation 1.32 is:

$$\text{PSD}(x,\omega) = 2k_BT\gamma 2\frac{1}{k^2+\gamma^2\omega^2} \tag{1.33}$$

Figure 1.3 (c) bottom panel shows a log-log plot of PSD *vs* f with typical values for the parameters involved. The corner frequency f_0 is the frequency at which the power drops to

half the power at $f = 0$. The stiffness is related to the corner frequency by

$$k = f_0 2\pi\gamma \tag{1.34}$$

Substitute equation 1.34 into equation 1.33 to express PSD in terms of f and f_0:

$$\text{PSD}(x, f) = 4k_B T\gamma \frac{1}{(f_0 2\pi\gamma)^2 + \gamma^2(2\pi f)^2} \tag{1.35}$$

$$= \frac{k_B T}{\gamma\pi^2} \frac{1}{(f^2 + f_0^2)} \tag{1.36}$$

The power spectrum method does not require the establishment of a QPD signal *vs* bead displacement look-up-curve. Also, low frequency data in the power spectrum plot is usually not as flat as the theoretical curve due to sources of noise in the lab. These are ignored by fitting the data to a Lorentzian curve so the stiffness measurement is more accurate than that obtained with the equipartition theorem method. In practice, the two methods are often used together so their results can be compared.

1.3.5 Example assays

Here I list a few key historical experiments to exemplify the use of OT in the interrogation of proteins and DNA.

Kinesin transports cellular cargos along microtubules [99]. OT were used to unveil the walking pattern of kinesin [4]. As shown in Figure 1.4 (a) upper panel, the OT place a kinesin-coated bead onto a microtubule. The kinesin translocates along the microtubule track, which pulls the bead. The stroke-release model (brief detachment from the microtubule) and hand-over-hand model (continuous attachment to the microtubule) were proposed for the motion of kinesin and the OT experiment could determine that the former matched the actual motion. Later experiments also applied resistance to kinesin up to 5-6 pN [5] so kinesin velocity under load is measured.

Myosins are also motor proteins but they move along actin filaments. Ensemble studies established that myosin-V moves multiple steps before detaching from the actin filament. Figure 1.4 (b) upper panel shows a 'dumbbell' (dual trap) OT assay where the myosin is tethered to the coverslip via a bead. The myosin step size is measured to be 36 nm [96]. One of the traps oscillates with a triangular wave, shown in figure 1.4 (b) lower panel. The myosin pulls the actin taught when it moves along the actin, so the envelope of the detected bead oscillation retreats, from which the amount by which the myosin has moved can be deduced. This method reveals step size, translocation velocity of an individual myosin-V in real time.

DNA are perhaps the most studied molecules with OT because of the axial shape that is particularly suited to OT studies and their importance in biology. Early experiments explored the extension as a response to applied force and resulted in 'force-extension curves', which theories use worm-like-chain to model [57, 58] - see figure 1.4 (c) lower panel. In a typical experiment, the dsDNA is tethered to a bead on one end and to the coverslip surface on the other [97]. The flow cell is then moved to pull the DNA and force and extension in the DNA measured. This is shown in figure 1.4 (c) upper panel.

Measuring the stepping of RNA polymerases along DNA was a milestone in OT

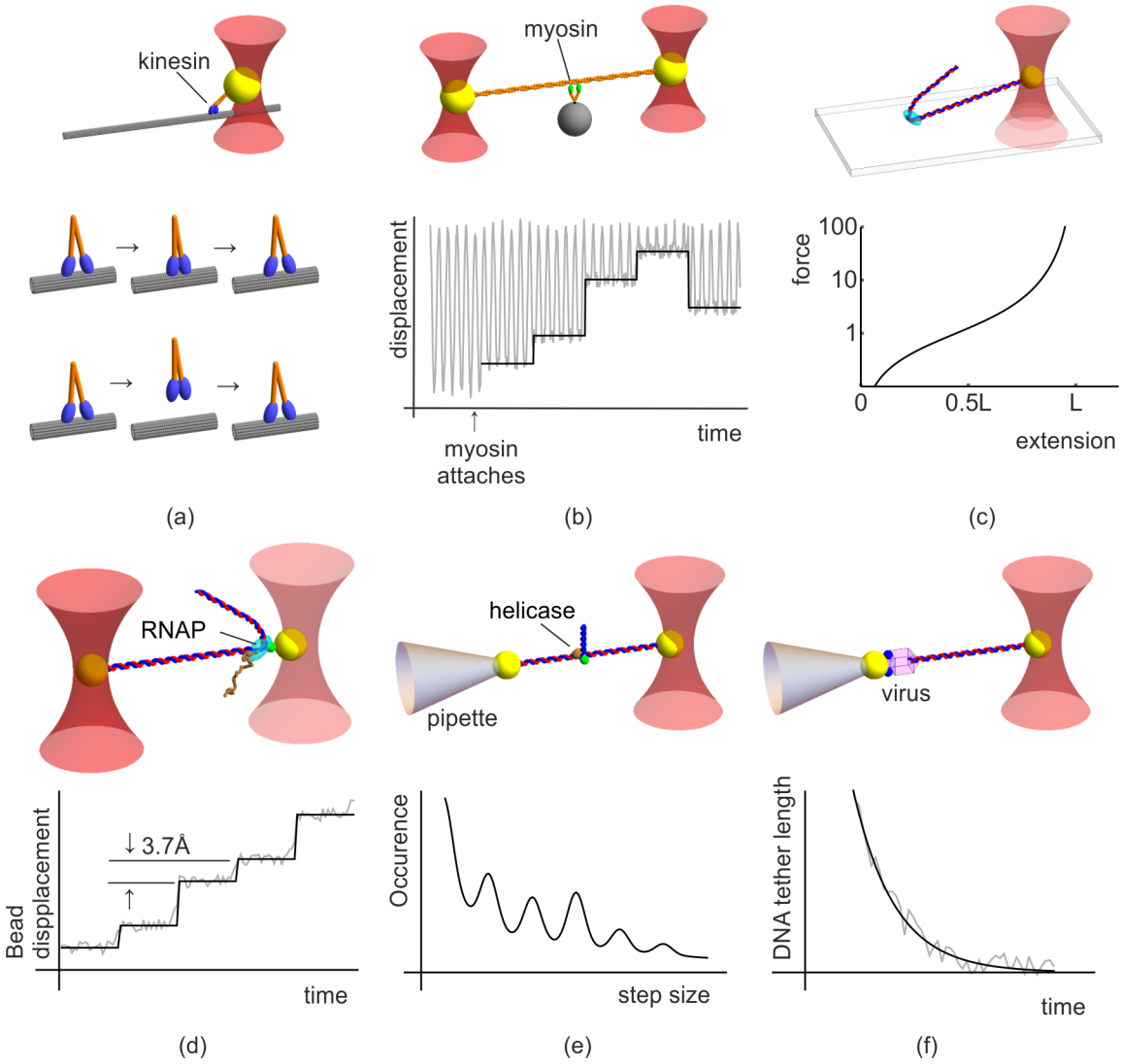

Figure 1.4: Historically important experiments performed with optical tweezers. (a) Upper panel: the optical tweezers assay to investigate the molecular-motor kinesin [4]. Lower panel: the conclusion drawn regarding the walking model of kinesin. On the top is the hand-over-hand model in which kinesin stays attached to the fibre for multiple cycles. Underneath is the stroke-release model, in which kinesin momentarily detaches from the fibre and diffuses back to carry on the movement. (b) Upper panel: the dumbbell optical tweezers assay to investigate the molecular-motor myosin-V [96]. Lower panel: trace of the bead displacement relative to the trap centre. The trap is set to oscillate triangularly. When myosin attaches to the actin, the oscillation traces are severed. Myosin displacement along the actin can then be determined (the thick line). (c) Upper panel: coverslip-DNA-bead tether to investigate DNA force-extension relationship. Lower panel: worm-like-chain model of DNA extension as a response to applied tension predicted by theory [57, 58] and verified experimentally [97]. (d) Upper panel: the dumbbell assay to monitor RNA polymerases movement. Lower panel: 3.7 Angstrom step size is resolved [10]. (e) Upper panel: another architecture involving a micro-pipette suction on one bead to monitor helicase movement. Lower panel: step size distribution [25]. (f) Upper panel: setup to measure virus DNA packaging. Lower panel: packing trace [98].

applications as the step size is only 3.7 Angstrom, approximately the rise size of a pair of nucleotides. The measurement is only possible with the dumbbell configuration shown in figure 1.4 (d) upper panel in which all stage-related noises are decoupled from the DNA filament. The bead displacement trace also reveals pause time, speed and other features of movement [10].

Figure 1.4 (e) shows an OT experiment to study helicase processivity. The use of a micro pipette tip to hold one end of the dsDNA molecule is similar to tethering the DNA end to the coverslip surface. The authors plotted the number of occurrences of various step sizes [25].

A similar configuration to the above is used to measure virus DNA packaging rate. Figure 1.4 (f) shows the setup [98]. The DNA outside the capsid is shortened over time as motor proteins tuck the genome into the capsid and generalised data of the shortening is plotted in figure 1.4 (f) lower panel.

1.4 Magnetic tweezers (MT)

Forces from magnetic tweezers operate at biologically relevant values of tens of pN. For example, the muscle protein titin contains Ig and Fn domains which unfolds at an applied force of 20 to 30 pN [100, 101] and dsDNA overstretches at around 65 pN [13]. The floor of applicable force is also important since it determines whether the smallest biological forces can be measured. In the case of MT, this value can be arbitrarily low so it is set ultimately by Brownian forces. The ability to easily and efficiently apply torque and rotation is the key strength of MT. Compared to optical tweezers, the construction and implementation of MT is more straightforward as it does not require the alignment of optical components yet the instrument is more robust as it is an infinite-bandwidth force clamp over a large sample volume [102]. Biological values of torque are in the range of a few to a few tens of $\mathrm{pN\,nm}$. Molecular machines unravel and separate the two strands of the DNA double helix with a $\sim 9\,\mathrm{pN\,nm}$ torque [103]. The ATP synthase F_1 motor and the associated membrane integrated F_O rotary motor, generates a torque $\sim 40\,\mathrm{pN\,nm}$ to transform the rotation into chemical potential energy locked into newly manufactured molecules of adenosine triphosphate (ATP). Early designs of MT struggled to produce a low enough torsional stiffness so the torque can be measured, but this has recently been overcome with specialised magnet geometries and electromagnets. The MOT arising from this PhD is significantly motivated by the need to measure torque applied on biomolecules.

This section introduces the many designs of magnetic and electromagnetic tweezers that are developed in the past two decades to meet mass and niche experimental needs. Also, the calibration of MT and a selection of notable historical experiments will be introduced. Just like the treatment of optical tweezers, I will leave some calibration details directly relevant to designing and calibrating my design to chapter 3 where my magnetic tweezers design is described.

1.4.1 Design of MT

MT are similar to OT in that they both manipulate a probe bead in single molecule experiments, which in turn is tethered to a biomolecule. Qualitatively, both techniques can apply and measure forces and torques onto single molecules whilst monitoring their

transformation and dynamics with imaging modules or interferometry tracking. However, there are features unique to MT that have consequences to their designs. For one thing, the equilibrium position for the magnetic bead is at the local $\mathbf{B}$ field gradient maximum, which is inside the magnet or electromagnet so the bead cannot be positioned at the equilibrium. As a result, the magnetic forces do not "trap" the bead per se but provides a directional force and relies on a counter force provided by the biomolecule to hold the assay in place - see figure 1.5 (c). The MT can also hold the bead in position by feedback loops that constantly adjust the field directions and strengths to keep the bead back at a set position.

Another character of the MT is the great varieties in which shapes and arrangements of permanent magnets in MT and copper coils in electro-MT come. Cubic, bar, cylindrical and horseshoe magnets mounted on motorised stages to move the magnets closer to or further away from the sample or to rotate the magnets have been implemented. The simplest design, a single bar magnet, provides a non-zero smooth field gradient so in theory can pull and rotate the bead along its axis. A much more common design involves the combination of two bar magnets placed side by side, which allows easy control of the field gradient by changing the separation between the magnets. Figure 1.5 (c) shows this classic arrangement of magnets. The arrows indicate the pulling and rotation of the biomolecule, which is limited to only one axis. Thus, a balancing force, usually from the biomolecule being tethered to the sample chamber but can also be hydrodynamic (figure 1.5 (d)), needs to counter the magnetic force. One disadvantage of this design is the enormous torque applied to the bead, which prevents measurement of the torque by the equipartition theorem method or indeed any other method to be used as the angular position of the bead follows the $\mathbf{B}$ field so closely that the angular offset between the bead and $\mathbf{B}$ is beyond the measurement precision. It is true that by bringing the magnets further away from the bead, the $\mathbf{B}$ field and thus the torque decreases, but so does force, which will drop below the required level. So force and torque transduction need to be separated. Cylindrical magnets arise from the effort of decoupling torque and force application from magnets. Figure 1.5 (e) illustrates the mechanism: the net gradient underneath the centre of the ring magnet is upwards so the pulling force still exists just as in (c). However, $\mathbf{B}$ integrated over the volume of the bead points vertically, so the bead is free to rotate along the azimuthal angle. This means although the torque in the biomolecule can be monitored, the magnet itself cannot apply torque. Offsetting the centre of the cylindrical magnets and the bead does allow torque to be applied as then the net $\mathbf{B}$ has a radial component. This is implemented in figure 1.5 (f). The authors also added a rod to amplify the angular displacement of the bead. Alternatively, a "side-magnet" as shown in figure 1.5 (g) breaks the circular symmetry of the geometry, which introduces a small $\mathbf{B}$ component for torque application. Apart from the limited flexibility, the disadvantages of permanent magnets include the vibrational noises from the motorised stage that needs to stay on the same optical table as the microscope and the flow cell. Nevertheless, these MT have elucidated the elasticity and interactions of some biological molecules.

Early designs of electro-MT featured copper coils wrapped around pole pieces whose tips reach close to the sample volume to maximise $\mathbf{B}$ for a given current. This allows the operation to be at low current and thus low generated heat. Electro-MT have the advantage of being able to selectively "turn-off" the coils or individually set the strength as function of time of each coil. Therefore, multiple poles can be installed whilst the currents in the

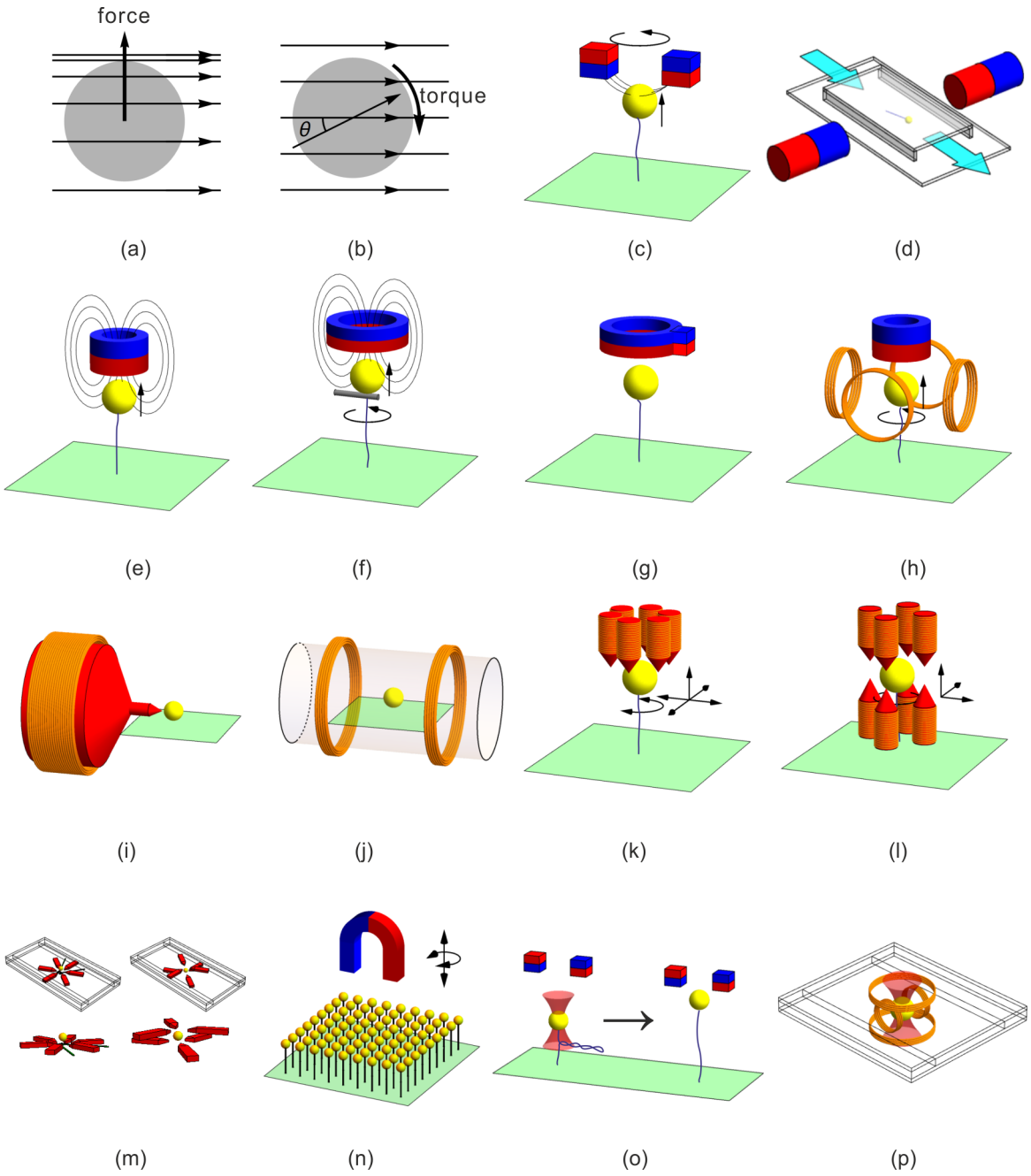

Figure 1.5: Schematic diagrams of magnetic tweezers. (a) Magnetic field gradient applies a magnetic force on a magnetised bead [63]. (b) Magnetic field and magnetisation of the bead misalign by angle θ, giving rise to a magnetic torque on the bead [63]. (c) Two-magnet setup to pull and rotate the bead [16]. (d) Magnets apply force in one direction while the liquid flow applies force in the orthogonal direction [12]. (e) The simplest magnet configuration which can apply a pulling force [104]. (f) A rod magnifies the angular position signal of the bead [105]. (g) A weak side magnet enables the application of a measurable torque [106]. (h) The side magnet in (g) is replaced by two Helmholtz coil pairs [107]. (i) Very strong magnetic field can be brought about with an electromagnet with many turns and a core piece close to the sample [108]. (j) Electromagnets composed of one Helmholtz coil pair, capable of oscillation in one dimension [109]. (k) A six-coil electromagnet capable of force application in 3 dimensions (excluding -z) [110] and torque [63]. (l) Coils both above and below the sample, enabling true 3-dimensional manipulation (ie. including -z) [111, 112]. (m) Microscopic electromagnets nanoprinted into the microscope slide with six pieces in one plane and two planes [113, 114].

Figure 1.5: Continued caption. (n) Lithographic printing to place samples in periodic fashion on the coverslip, allowing high-throughput experiments [115]. (o) Combination of magnetic tweezers and optical tweezers, which allows the instant removal of optical forces by turning off the laser [17]. (p) Combination of electromagnetic tweezers and optical tweezers, decoupling force and torque application/measurement [116].

electromagnets are individually controlled to generate a full two dimensional force in the horizontal plane in addition to a uni- or bi-directional vertical force - see figures 1.5 (k) and (l) respectively. However, these designs do not evade the large torsional stiffness problem associated with MT except when sophisticated fast-rotation methods that explore nonlinear angular velocity response are used [63] but that poses a big calibration challenge. Just like the case of permanent magnet MT, the key to torsional stiffness lies in the separation of torsional and force transduction. For example, a torsion-less cylindrical magnet can apply the force while a group of Helmholtz coils apply torque. Helmholtz coils generate a near-uniform magnetic field so the $\mathbf{B}$ field from them can be considered force-less. Figure 1.5 (h) utilises such a design. Note that this particular choice of two pairs of Helmholtz coils can only rotate the bead along one axis. It takes three pairs for full three directional rotation [117]. Such coils can also be combined with optical tweezers rather than a cylindrical magnet for force application - see figure 1.5 (p). Such a combination is the what my MOT design will base on.

An interesting configuration is one pair of Helmholtz coils, which cannot rotate the beads but it has found applications in oscillating them - see figure 1.5 (j). Electro-MT with a single coil - the simplest possible electro-MT - has also been designed, see figure 1.5 (i). This time it provides just a pulling force. The motivation behind such a design is the huge $\sim 1000\,\mathrm{pN}$ scale forces the tweezers are able to apply to the beads.

Another design consideration is spatial constraints: a typical commercial microscope has limited space available in the vicinity of the sample volume. Even in the case of all coils placed to one side of the flowcell, as in figure 1.5 (k), the compromise of removing the condenser has to be made. In the case of coils arranged at both sides of the flowcell for full three-dimensional control, bespoke microscopes are usually used [112] with the exception where the coils are far apart to leave space for the microscope components and the core tips are thin and long to reach the sample [111]. Efforts to efficiently use space also leads to nanofabricated micro-electro-MT [113, 114] which are small enough to fit into the flow cell but have the full 3-dimensional transduction capability.

Attempts have also been made to rotate the molecule along the rotational axis of the magnet pairs and then the arm holding the magnets can be moved sideways so that the molecule attached to the magnetic bead lies in the transverse plane. Loenhout et al. [258] used such an approach to supercoil a DNA molecule and extend it in the transverse plane for fluorescence imaging.

1.4.2 Calibration of MT: the equipartition theorem method

Just as in the calibration of optical tweezers where the stiffness of the laser trap is measured, here the stiffness of the magnetic field, k_θ, is measured. I will focus on the angular stiffness as in this project the MT I have built will be used to apply torque and not force. The magnetic

bead has a magnetisation component along its preferential direction - more on this can be found in chapter 3 - for now we pretend this is the bead's sole magnetisation and it scales linearly with $\mathbf{B}$ at low field and plateaus at high field. If this magnetisation is at an angle θ to the magnetic field, the angular potential in the vicinity of the equilibrium position is quadratic so for small θ, the torque applied to the bead by the magnetic field is

$$\tau = k_\theta \theta \tag{1.37}$$

where k_θ is the angular spring constant. Indeed, this is the angular version of the Hooke's law. Two methods can be used to evaluate k_θ: the (angular) equipartition theorem and the angular retardation method. It may seem natural that an angular version of the power spectrum method should apply here since so far all analysis of MT mirror those of the OT (indeed there is a retardation method for OT as well, though it is beyond the scope of this thesis). But an estimation of the corner frequency reveals the problem. The angular motion of a spherical Brownian particle from fluctuating hydrodynamics is expressed with the rotational Langevin equation [118]:

$$I\ddot{\theta} + \zeta\dot{\theta} + k_\theta\theta = \tau_B(t) \tag{1.38}$$

where I is the moment of inertia of the bead, $\zeta = 8\pi\eta R^3$ is the angular hydrodynamic drag coefficient [119], R is the radius of the magnetic bead, $\tau_B(t)$ is the Brownian torque. The power spectral density thus is (the inertia term in equation 1.38 is neglected, since the bead operates in the low Reynolds number regime):

$$\mathrm{PSD}(\theta, f) = \frac{k_B T}{\zeta \pi^2} \frac{1}{(f^2 + f_0^2)} \tag{1.39}$$

and the corner frequency given by

$$f_0 = \frac{k_\theta}{2\pi\zeta} \tag{1.40}$$

If we choose $k_\theta = 100\,\mathrm{pN\,nm\,rad^{-1}}$, the corner frequency evaluates to:

$$f_0 = \frac{100 \times 10^{-21}}{2\pi \times 8\pi \times 8.9 \times 10^{-4} \times (1.5 \times 10^{-6})^3} = 0.2\,\mathrm{Hz} \tag{1.41}$$

Signal having corner frequency of such low values is well buried in the noises surrounding the assay so cannot be tracked.

Now I begin discussing the equipartition theorem, the angular version of which reads:

$$k_\theta = \frac{k_B T}{< \theta^2 >} \tag{1.42}$$

Equation 1.42 allows the evaluation of k_θ. In the case of MT, angular displacement due to rotational Brownian motion cannot be obtained with measuring the interference pattern between the laser and the bead at the back focal plane of the condenser because the measurement will inevitably contain signal due to linear Brownian motion so video microscopy is used to measure the rotation. The magnetic bead is noticeably rotating on the camera but to implement algorithmic read-out of the angular displacement from video data, extra asymmetry needs to be introduced onto the surface curvature of the bead. This

can be done with a fiducial bead with a small diameter of tens of nanometres being chemically tethered to the magnetic bead. Since the fiducial bead is below the optical resolution, it needs to be fluorescent and rotation videos are taken in fluorescence rather than bright field. Alternatively, a larger bead can be used so videos can be taken in bright field but this will increase the rotational drag on the bead which limits the rotation speed when it is needed. Either way, the marker bead will be non-magnetic so it does not contribute to the magnetic torque (or force) applied on the dual bead complex. A ring with a thickness that encompasses the trace of the marker bead is cut out of the image series and the pixel intensity is summed along the radial directions to obtain a sum intensity value as a function of angle. Depending on how out of focus the marker bead is (it can be set deliberately out of focus in some systems), the marker bead will appear brighter or darker than its surrounding and thus contribute to the intensity-sum positively or negatively. The centre of the marker bead will correspond to the peak or trough of the intensity *vs* angular position plot, which is used to determine the angular displacement of the marker bead. This method has been reported to track a 1 µm fiducial bead tethered to a 3 µm magnetic bead with resolution of $0.1°$. Assuming $k_\theta = 100\,\mathrm{pN\,nm\,rad^{-1}}$, the resolution in torque measurement is $0.2\,\mathrm{pN\,nm}$.

The above data analysis applies to rotation along the vertical axis. However, in my transverse-DNA assay, the rotation axis will be horizontal, as shown figure 1.6 or 2.1. To modify the above calibration, I will select a marker bead which is approximately in the centre of the trapped bead as seen on the camera. Figure 1.6 (a) shows the bead centred exactly on the magnetic bead. The rotation along the magnetic field rotational axis is denoted θ, shown in (c). The positions of the marker bead in the video are 2D projections of the 3D positions so θ corresponds to $(R + r)\sin(\theta)$ in the video, where R and r are the radii of the magnetic and marker bead respectively. In reality an angular offset of ϕ from the centre is inevitable, as shown in (b). This reduces the displacement to $(R + r)\sin(\theta)\cos(\phi)$. The measurement will have variations both in ϕ and θ. The former will be treated as measurement errors while the latter used to obtain the stiffness.

1.4.3 Calibration of MT: angular retardation method

The angular retardation method involves rotating the magnetic-marker bead complex with a constant speed but at varied $\mathbf{B}$ field strengths. The idea is that there will be an angular offset between the bead's magnetisation and the $\mathbf{B}$ field due to the angular drag applied on the bead by the solution. Since the drag is constant at constant rotational speed, increasing $\mathbf{B}$ will result in a reduced θ to keep the resulting magnetic torque constant. This time, it will not be straightforward with video microscopy to measure θ but the QPD signals come to rescue. Assuming V_{LR} is in the direction of the fiducial bead movement, V_{LR} will be a function of θ - ideally it will be a sine wave if there is one marker bead attached, shown in 1.6 (d), the black curves. We will see in chapter 3 that the measured curves are quite distorted but they are periodic, which is enough to extract the phase. The phase difference between V_{LR} and the $\mathbf{B}$ field can be plotted and a linear line fit - see 3 (e), the slope of which is then used to find the torsional stiffness.

The viscous torque applied on a sphere is $\zeta\omega = 8\pi\eta R^3\omega$, where ω is the angular speed (not to be confused with the angular frequency in equation 1.14). The magnetic torque

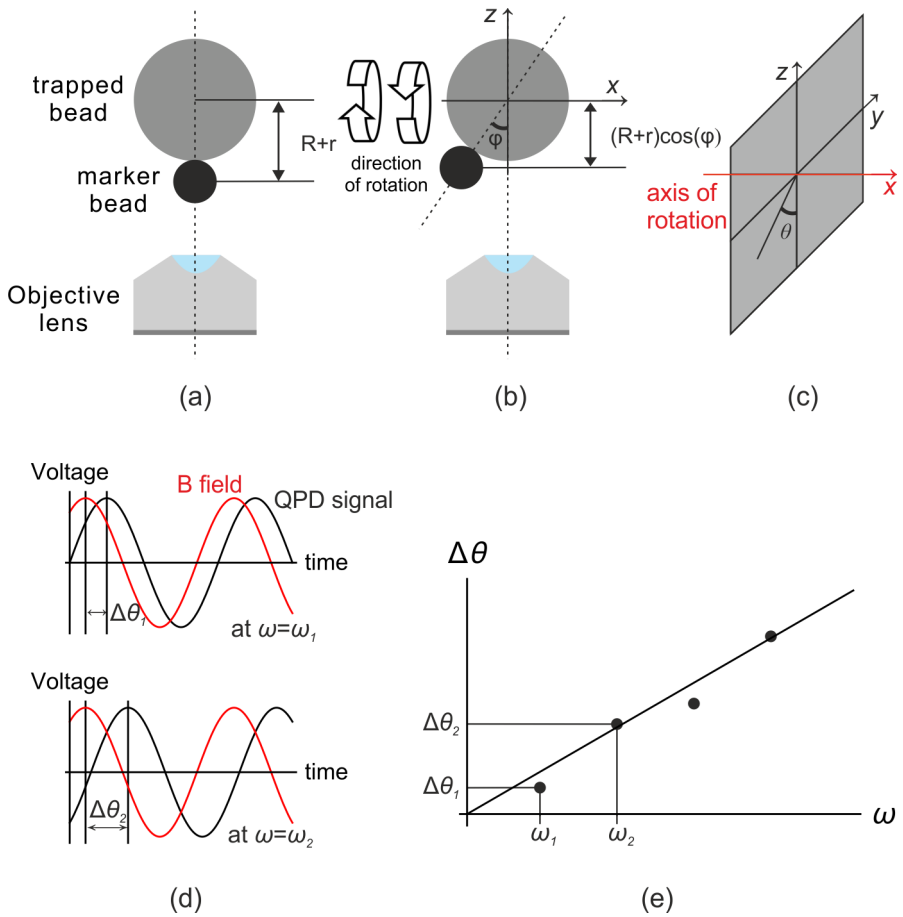

Figure 1.6: Magnetic tweezers calibration to obtain the torsional stiffness. (a) to (c) illustrate the equipartition theorem method. The positions of the marker bead is read-out with video microscopy in either bright field or fluorescence. The complication with my instrument is the transverse rotational axis, which results in the marker bead videos being 2D projection of the bead's 3D movement. The video images show $(R + r)\sin(\theta)\cos(\phi)$, where ϕ is the deviation of the marker bead from the plane perpendicular to $\mathbf{B}$ field rotation, labelled as the grey plane in (c). (d) and (e) show calibration by retardation method. (d) QPD voltage signal and B field *vs* time. The offset between them is a function of $\mathbf{B}$ field strength. (e) Plot of $\Delta\theta$ *vs* ω allows the determination of k_θ. Data points are fictitious for the illustration of the method.

balances out the viscous torque:

$$k_\theta \theta = 8\pi\eta R^3 \omega \tag{1.43}$$

Rearrange to get

$$\theta = \frac{8\pi\eta R^3}{k_\theta}\omega \tag{1.44}$$

The periodic QPD signal does not offer the determination of θ, but it does offer the determination of the phase difference between θ and a reference phase, such as the phase of the $\mathbf{B}$ field. Figure 1.6 (d) illustrates this. The top plot shows QPD signal (black curve) when the $\mathbf{B}$ field (red curve) is rotated at ω_1; the bottom plot shows the corresponding signals at ω_2. These two points are labelled in (e). This is also why $\Delta\theta$ rather than θ is plotted in (e).

The angular retardation method has been used to obtain $k_\theta = 3500\,\mathrm{pN\,nm\,rad^{-1}}$ at $\mathbf{B} =$

$4.8\,\mathrm{mT}$ and $R = 2.6\mu\mathrm{m},$. The resolution (minimum detectable torque) is $200\,\mathrm{pN\,nm\,rad^{-1}}$.

1.5 Noises and errors

The single molecular nature of the experiments performed with the magneto-optical tweezers in this project grants the consideration of noises particular importance. The biomolecules are in an aqueous solution *in vivo* or *in vitro* during measurements and thus are constantly bombarded with water molecules. In spectroscopy, the resulted Brownian motion poses huge challenges to the measurement of the molecule's topology, elasticity and dynamics. However, the Brownian motion has also been utilised as a means to calibrate the stiffness of the optical traps and the magnetic field by the equipartition method or the power spectrum method - see section 1.3 and 1.4.

In fluorescence microscopy, the Brownian motion of the observed molecules continues to complicate the interrogation of molecular properties and there is the extra challenge of detecting the often dim fluorophore emissions buried in background light.

In this section I will briefly discuss the noises that challenge as well as assist single molecular experiments. On a different note, I will also explain my treatment of measurement errors, which are universal to all experiments.

1.5.1 Noises in spectroscopy

In force spectroscopy, noise is the fundamental limit on measurement precision for a given measurement bandwidth. Ultimately, Brownian noise sets the celling of measurement resolution. The measurement precision is inversely proportional to the Brownian noise level. Recent advances in instrumentation and methodology have largely focused on reducing sources of noises such as air currents, mechanical vibration, thermal expansion and electrical noise in sensors, etc. The aim is to reduce the noises sufficiently so molecular signals can be read out.

Optical tweezers measurement with sub-nm resolution is now routinely achieved in temperature-controlled ($\pm 0.2^{\circ}\mathrm{C}$), acoustically-isolated rooms [120]. Controlling instruments with motorised moving parts such as laser drivers and PCs are typically housed in a separate room. To reduce mechanical vibration, spectroscopy instruments sometimes have a bespoke reinforcement skeleton added to the setup. For example, the microscope condenser pillar was strengthened with an aluminium trapezoid in [120], or the condenser mount can be replaced with heavy-duty versions [121].

For measurement of protein motions within the frequency range of noise induced by air currents, optical components have been enclosed in boxes filled with helium gas, which has lower refractive index than air, and thus cause less deflection of the laser beam. This method has been used to decrease noise spectral density to 10% the level without helium replacement [10]. A more convenient way to suppress air currents not involving replacing air with helium is to simply enclose optical components in boxes although this achieves less noise reduction. Optical tweezers often use a near infra-red (NIR) laser for trapping. The water absorption coefficient at NIR wavelengths is approximately $1\ \mathrm{cm^{-1}}$, which is 2 to 4 orders of magnitude higher than that in the visible range. Some designs of electromagnetic tweezers, particularly high-force ones, generate significant amount of heat.

A 1°C temperature gradient potentially causes mechanical drift of optical components on the order of 100 nm [102] on a time scale of seconds to minutes. In comparison, the step size of kinesin is 8 nm [10], DNA base pair thickness is 0.34 nm, which defines the minimum step size of DNA processing proteins and the unfolding of protein domains are 20-30 nm [122, 123]. Thermal expansion can be efficiently removed from measurement data by marking the flow cell with a fiducial bead and subtracting the displacement of the bead from the data. This has been shown to achieve 0.1 nm stabilisation of the flow cell along all 3 spatial axes [94].

Brownian noises in displacement measurement of the trapped bead (for example by optical tweezers) which immerses in liquid can be quantified by rearranging equation 1.8 to get

$$< x >= \sqrt{\frac{k_B T}{k}} \tag{1.45}$$

Assuming $k = 50\,\mathrm{pN\,\mu m^{-1}}$ and $T = 300\,\mathrm{kelvin}$, we get $< x > \approx 10\,\mathrm{nm}$. This resolution may allow the measurement of the unfolding of protein domains but is a far cry from measuring kinesin or RNA polymerase step sizes. However, the resolution can be improved by reducing the measurement bandwidth. Brownian noises average to zero over a long time so slower measurement results in less noise amplitude. From a different perspective, the area under the power spectral density plot (figure 1.3 (c), bottom panel) is equal to $< x >^2$. Reducing the measurement bandwidth to $f_{measure}$ amounts to integrating the power density up to $f_{measure}$ rather than infinity, so $< x >^2$ is less. $< x >$ can be expressed as

$$< x >= \sqrt{\frac{4\gamma k_B T f_{measure}}{k^2}} \tag{1.46}$$

Again assuming $k = 50\,\mathrm{pN\,\mu m^{-1}}$ and $T = 300\,\mathrm{kelvin}$, and $f_{measure} = 10\,\mathrm{hertz}$, we get $< x > \approx 1.3\,\mathrm{nm}$, which is a ten-fold improvement on high-bandwidth measurement. The caveat is the loss of temporal resolution. In this example it is 100 ms so processes quicker than this time frame cannot be measured. From equation 1.46, it can be seen then increasing trapping stiffness and using a smaller bead (so lower drag) can also reduce noise.

1.5.2 Noises in fluorescence microscopy

If we model the fluorophore as a point light source, the point spread function (PSF) of the fluorophore's image on the camera will be:

$$PSF(r) = \left(2\frac{J_1(r)}{r}\right)^2 \tag{1.47}$$

where r is the normalized radial coordinate and J_1 is the Bessel function of the first kind. The PSF is pixelated due to the finite smallness of the camera pixel. The centre of the fluorophore can be algorithmically found by finding the centre of the PSF, which is often approximated with a Gaussian distribution. Noises in fluorescence microscopy result in the uncertainty in the determination of the centroid of a fluorophore. For now we ignore the fact that the fluorophore does not exactly coincide the tagged molecule (ie. fluorophore position is not equal to the biomolecule position), and we ignore any possible Brownian motion of the

fluorophore. The uncertainty in fluorophore centroid is [124]:

$$< \Delta x >= \sqrt{\frac{s^2 + a^2/12}{N} + \frac{4\sqrt{\pi}s^3b^2}{aN^2}} \tag{1.48}$$

where Δx is the uncertainty in localisation, s is the standard deviation of the PSF, a is the size of the camera pixel edge length, b is background noise and N is the number of detected photons. To reduce localisation error, one can increase the number of collected photons, decrease the standard deviation of the PSF, decrease background noise and/or decrease pixel size. For fluorescence imaging, the emission wavelength differs from that of the excitation wavelength so an emission filter can be used to block out all but a $\sim$50 nm window of light so noises are significantly blocked out. Nevertheless, noises still challenge fluorescent microscopy. Innovations have tackled all of the parameters in equation 1.48. High numerical aperture objective lenses (even two objectives head to head have been used) are used to minimise the s.d. of the point spread function, the boundaries of camera pixel sizes have been pushed and ever brighter fluorophores been engineered. Bright fluorophores are needed as the time window to collect photons is rather short in cases of high temporal resolution microscopy. The state of the art now is that the limiting factor on imaging uncertainty is no longer $< \Delta x >$ but the size of labelling probe and the labelling density.

1.5.3 Measurement errors

Here I discuss my treatment of measurement errors in this thesis. Unless stated otherwise, the following procedures apply to all protocols and analysis.

Although this is not always done, the systematic errors are checked by using two different methods. For example, in the characterisation of the optical trap stiffness, the equipartition method and the power spectrum method are used and measurements compared. However, for some measurements, no such cross-checking is performed. For example, I used a thermocouple to measure the temperature rise of the coils in the magnetic tweezers. No other thermometer was used. However, I did compare empirical values to theoretical values. Still, the empirical values are vulnerable to uncharacterised systematic errors. It will be clear from the texts in each instance if cross-checking with two different methods are used.

Random errors are always dealt with by taking two or more repeated measurements and quantified with the square root of the bias-corrected variance among the measurements, expressed as

$$s_{N-1} = \sqrt{\frac{1}{N-1}\sum_{i=1}^{N}(x_i - \bar{x})^2} \tag{1.49}$$

where N is the number of repeated measurements, x_i is the ith repetition and $\bar{x}$ is the arithmetic mean of x_i. The measurement values themselves are taken to be $\bar{x}$. An example of exceptions is the specification of the magnetic bead diameter (see table 3.1), which is supplied by the manufacturer. Coefficient of variation is used. The manufacturer did not explicitly state whether sample standard deviation or the square root of the bias-corrected variance was used to calculate coefficient of variation. These exceptions have all been made clear in the main text. For modelling, errors have not been taken into consideration, as the

values from modelling are treated as guides only.

Chapter 2

Optical tweezers

The implementation of spectroscopy will be described in this chapter and the next. In this chapter, I will describe the optical diagram and calibration of the optical tweezers that are a part of the magneto-optical tweezers are described in detail in this chapter but first I will briefly describe the MOT as a whole and where the OT fit into the big picture. Then magnetic tweezers are left to chapter 3.

2.1 The overall magneto-optical tweezers design

Figure 2.1 shows a cartoon of the magneto-optical tweezers. The biological applications in our lab will involve probing and imaging dynamic single molecule topology of DNA, protein machines that manipulate DNA topology and other filamentous molecules. The imaging capability of the device requires that the tweezers lie the biomolecule in a transverse orientation in the imaging plane for contour-wise imaging. The rotational axis thus is perpendicular to the optical axis. Due to the limits in space posed by the Nikon microscope (Eclipse T*i*-U, Nikon Instruments Ltd.) and the Mad City Lab piezoelectric nanostage (Nano-LPS100), the option of using permanent magnets or electromagnets with multiple cores to generate the magnetic field are ruled out. However, two pairs of Helmholtz coils without pole pieces are small enough to fit in the opening in the nanostage while leaving enough space for mounting the sample. A Helmholtz coil pair composes of two concentric circular loops of the same radius separated by one-radius distance. It is the simplest geometry to generate a uniform magnetic field over a large volume, which suits our purpose of rotating the magnetic bead. Since the MT in this design do not apply forces, optical tweezers are used for positioning and force manipulation. In the flow cell, a super-paramagnet bead is trapped by the laser tweezers and rotated by the optical tweezers concurrently. A DNA molecule is tethered to the bead (micromer®-M, streptavidin, 08-19-303, © micromod Partikeltechnologie GmbH) on one end and a larger polystyrene bead (Anti-Digoxigenin Coated Polystyrene Particles, DIGP-40-2, Spherotech, Inc.) on the other. The polystyrene bead, also referred to as the "anti-DIG bead", is immobilised to the coverslip at multiple points to translationally and rotationally constrain that end of the DNA. Fluorophores bind at random places along the contour of the DNA for imaging.

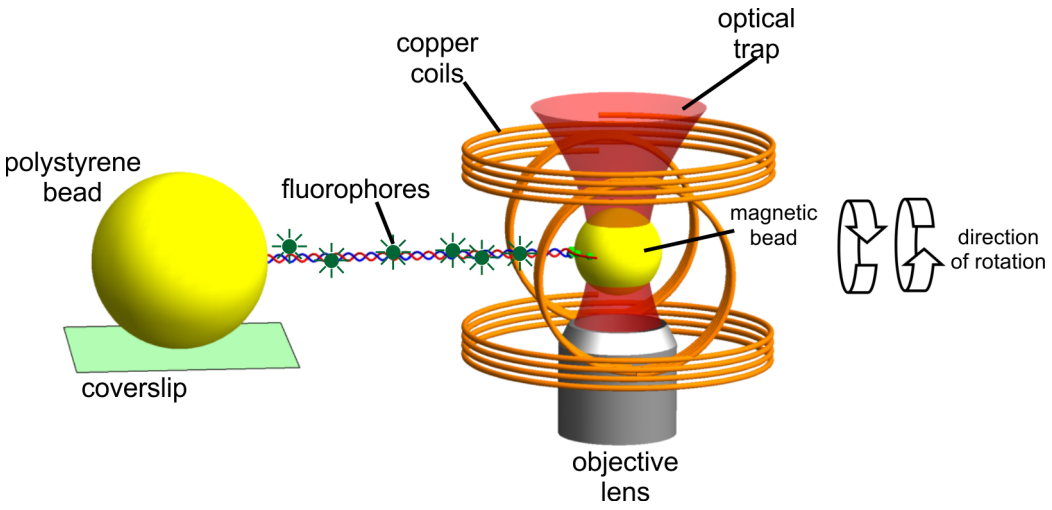

Figure 2.1: Cartoon of magneto-optical tweezers. The components are not drawn to scale.

2.2 The optical system

In this this section I will describe the optical system and the calibration of the OT. Figure 2.2 (a) shows a diagram of the optical components that are parts of the optical tweezers. A near-infrared laser (1064 nm, max output 4 W, Elforlight L3000-1064) sends a beam, which is attenuated with a half-wave plate (WPH05M-1064, Thorlabs Inc.) and a polarisation beam splitter (PBS123, Thorlabs Inc.). Figure 2.2 (b) illustrates the attenuation mechanism: the output of the laser is linearly polarised, the direction of which is not important. The half-wave plate is mounted on a motorised rotational mount (KPRM1E/M) so can be computer controlled. When the light passes it, the direction of the polarisation changes from 0 to 360 degrees, depending on the angling of the half-wave plate. When the beam then passes the polarisation beam splitter, p-polarized light transmits while s-polarized light reflects. The former is let into the microscope whereas the latter is dumped into a beam stop. The power of the transmitted light is a cosine-squared function of the polarisation beam splitter orientation. Figure 2.2 (c) shows a plot of power *vs* angle. The output of the laser has been set to a low value of about 0.15 W to prevent power meter damage. The red crosses are fit with a cosine-squared curve (black). After attenuation, the beam is expanded 10-fold to approximately match the entrance pupil of the objective lens (100x, NA 1.45, oil immersion, model no. MRD01095, Nikon Instruments Inc.) to maximise the trapping stiffness [125,126].

The beam then passes through a dual-axis acousto-optic deflector (AOD, part no. LS110-1064, Isomet), which creates one or multiple time-shared beams with high speed and resolution beam steering for each trap. Figure 2.3 (a) shows the x-axis of the AOD turned on. The laser, which originally is the green spot in the centre, now spreads into an infinite number of diffraction orders. The darkest green spot is selected to be the order of interest and the angling of the AOD device is set to Bragg's angle to maximise the energy that enters the darkest green spot. Higher order spots than the first order are not plotted. (b) shows the pattern when both x and y axis are turned on and the 1st order in both axis (the red spot on bottom left) is selected to be the order of interest. (c) is a photo of the spots when they are projected on a screen a distance away from the AOD. It is worth pointing out that AOD suffers from loss of power into the unused orders. Figure 2.3 (d) shows the measurement of the laser power exiting the AOD. A minority is lost after the AOD crystal

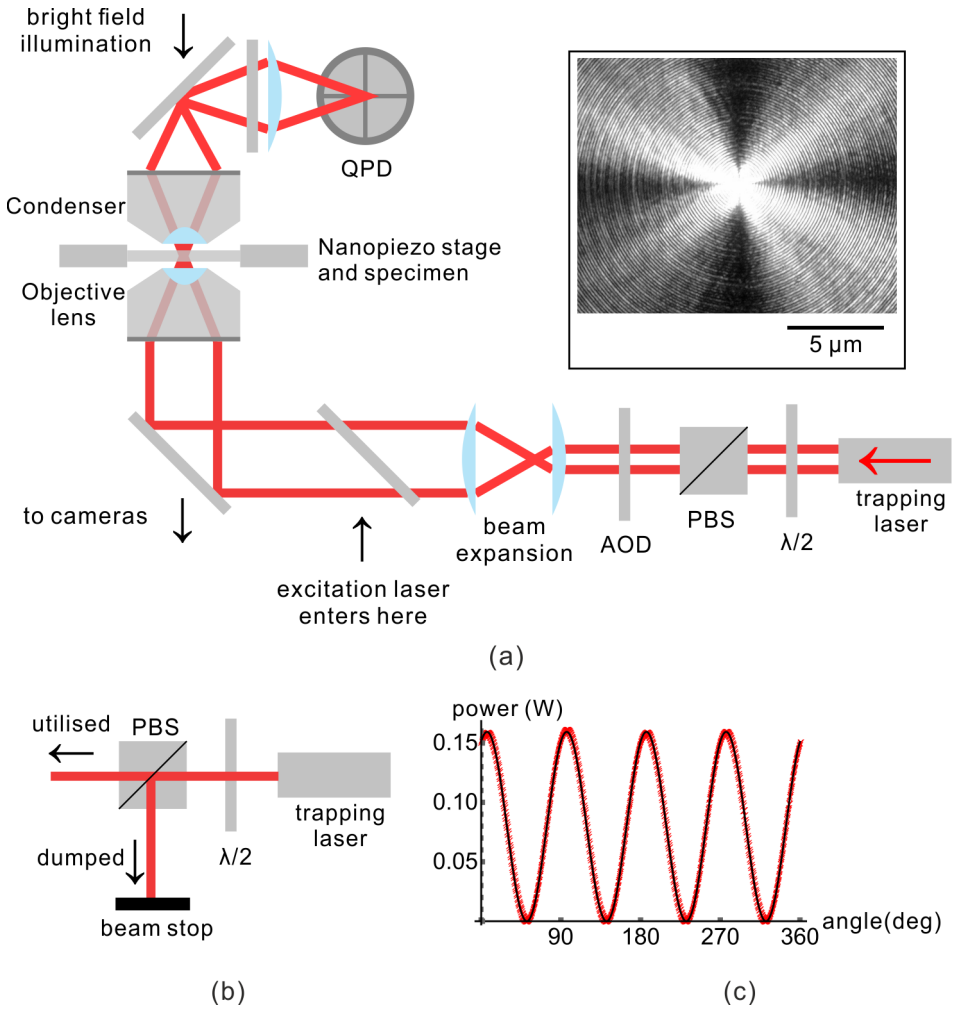

Figure 2.2: Schematics of the optical system that forms the laser trap.

when the AOD is off. About 30% is lost when one axis is turned on and more than 80% lost when both axes are on. Since I have a 4 W laser, this still leaves a little less than 800 mW for trapping in the case of single trap, which is more than enough. In the figure, with and without expansion refers to the 10 times beam expansion being placed before or after the AOD - see figure 2.2. The difference between them is negligible. The centre frequency is 50 MHz and bandwidth is 25 MHz. Test data ranging approximately from 40 to 60 MHz and the corresponding positional changes of the trap in both x and y axis in the sample plane are shown in figure 2.3 (e). The frequency, phase and amplitude instructions are sent through priority Isomet software, the UI of which is shown in figure 2.3 (f). The rise time of the beam steering is set by the ratio of the laser beam diameter to the speed of sound in the crystal, or approximately 2 µs, so the AOD can steer the beam quickly. The beam is then expanded 10 times before entering the objective lens. After the objective, the beam focuses to a diffraction limited spot and diverges again. An oil immersion condenser (NA 1.4, Nikon Instruments Inc.) re-collimates the beam. A pattern due to the interference between the scattered beam (by the bead) and the unscattered beam forms at the back focal plane of the condenser. An imaging lens projects this pattern onto a QPD (QP50-6-18u-SD2, First Sensor) placed at the conjugate plane to the condenser BFP to detect the interference signal (V_{LR}, V_{TB} and V_{SUM}, see Chapter 1 section 1.3.2 for details). An analogue input device (NI 9222 and NI cDAQ-9174) records the signal at 50 kHz. Figure 2.4 shows the LabVIEW code for controlling the cDAQ card and writing the data to text files. The setup can potentially

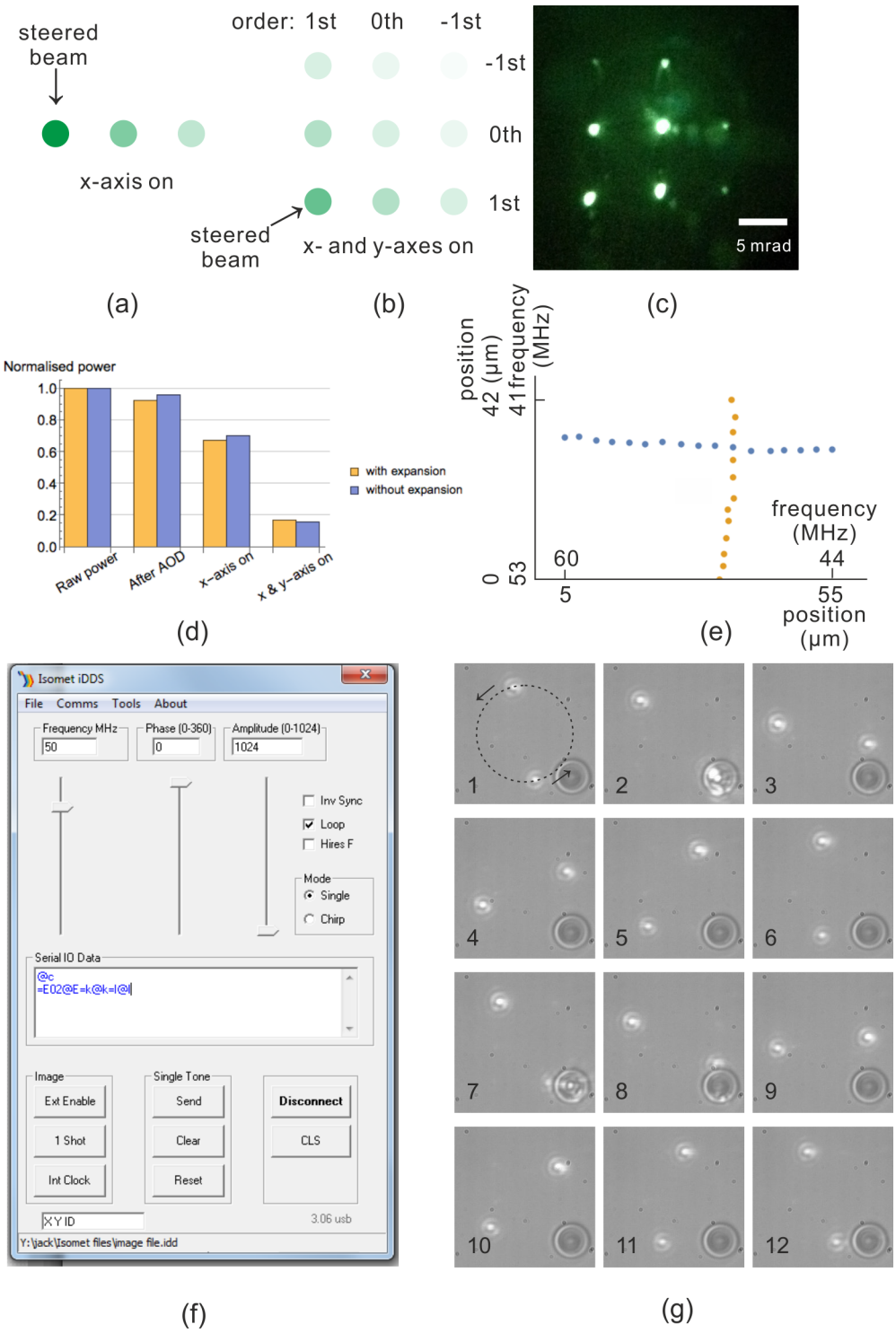

Figure 2.3: The acousto-optic deflector. (a) X-axis of the AOD turned on. The zeroth and first order spots are shown with red and green spots with red being the spot of interest. (b) Both axes turned on. The spot of interest can be any of the four spots in the corner but the bottom left one was chosen. (c) A photo of the spots. The scale bar shows 'arbitrary length' because the actual scale depends on the distance between the AOD and the screen so it is not meaningful. (d) Loss of power when the AOD is off, one axis on and both axes on. (e) The frequencies of acoustic wave and the corresponding trap position in the sample plane. (f) The user interface of the manufacturer supplied software that controls the AOD.

incorporate a second QPD for independent monitoring of the drift of the coverslip with a

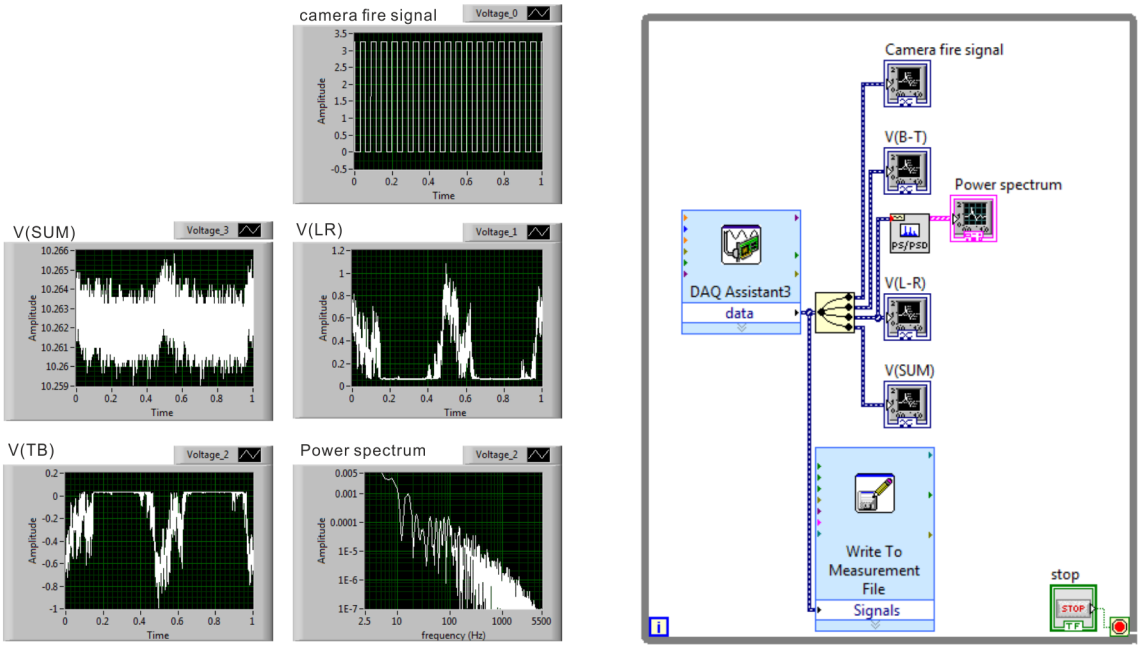

(a) (b)

Figure 2.4: LabVIEW code for reading out the QPD signals into the NI cDAQ card and writing into a text file. Camera fire signal is also wired into the same cDAQ card and recorded so that the camera and the QPD signals can be synchronised. (a) The front panel. (b) The block diagram.

fiducial marker and an auxiliary tracking laser [127] for stabilisation of the sample space.

Air conditioning (MFZ-KA50VA, Mitsubishi Electric) contains the temperature fluctuations in the lab to within $\pm 0.1°\mathrm{C}$. Equipments with motorised moving parts are housed separately from the optical table. The optical system, the microscope and the magnetic coils are mounted on an air-cushioned table (PTQ51504, Thorlabs Inc.) to reduce acoustic and mechanical noise. An aluminium box shields the lasers so no beam is exposed and also air-flow induced beam pointing instability is reduced.

2.3 Calibration of the trap

I calibrate the trap using both the equipartition theorem method (see section 1.3.3) and the power spectrum method (see section 1.3.4). For the former, a look up table/curve is created between the QPD voltages and the bead positions. A flow cell in this case is composed of a slide, a coverslip and two strips of double-sided tape in-between to leave a tunnel between the two glasses. The magnetic bead (see table 3.1) is diluted to 1 in 2000 buffer solution ($1\times$ PBS and 400 mM KCl). The magnetic bead is immobilised to the coverslip surface by non-specific adsorption. Then a bead is moved approximately to the equilibrium position of the laser trap. More on the accurate positioning of the coverslip-immobilised bead along the z direction can be found in chapter 3. It is difficult to position the bead exactly at the laser centre in the x and y directions so I have come up with the idea of scanning the entire surface of a 4 by 4 $\mu\mathrm{m}$ area, line by line, adjacent lines separated by 40 nm so there are 101 lines of scanning in total. The schematics in figure 2.5 (a) top right shows the trace of the bead movement. This way, the scanning closest to the laser centre will be selected as the

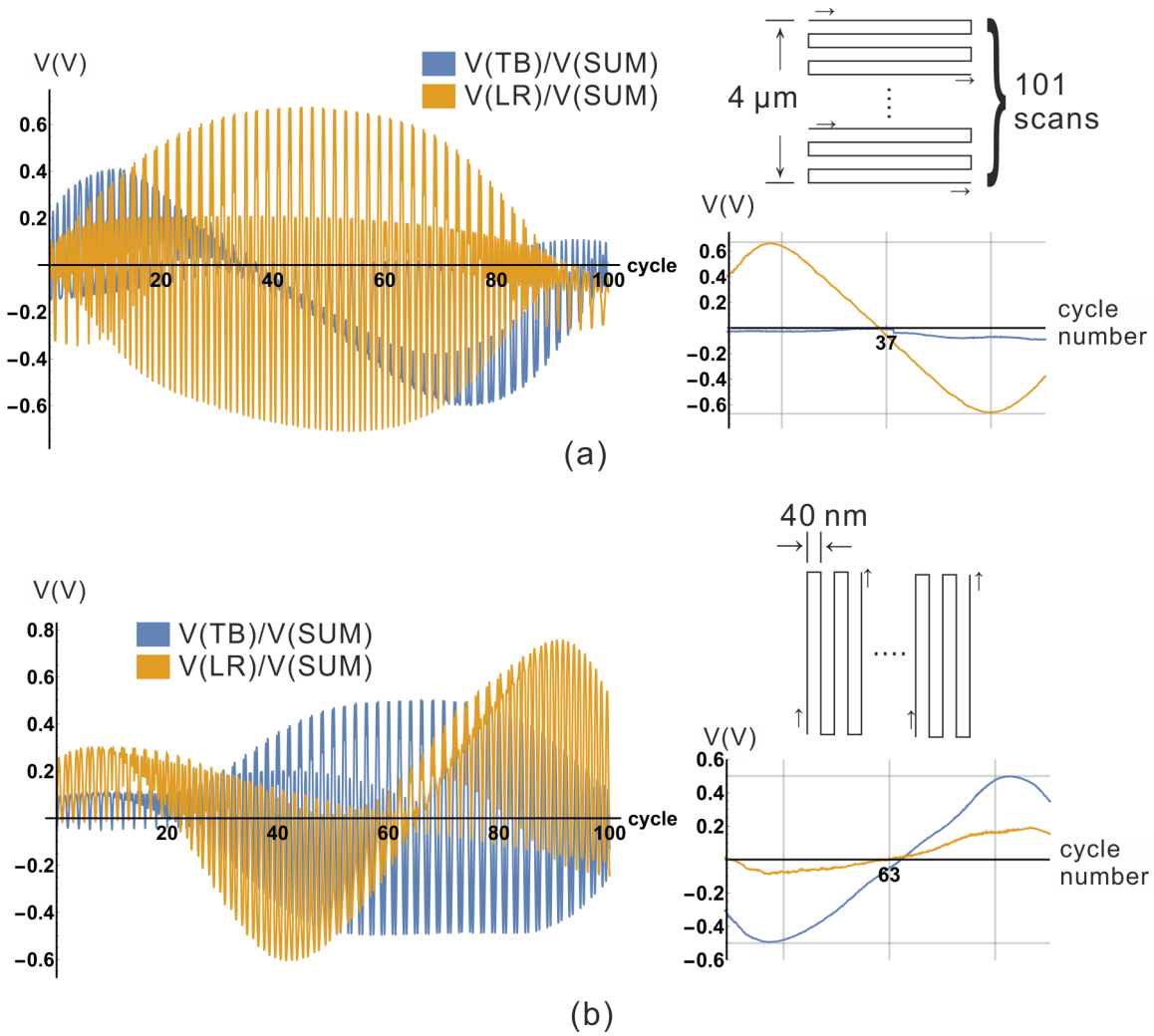

Figure 2.5: QPD voltage *vs* bead displacement calibration. (a) Horizontal scan. The bead starts from top left, namely -2 µm along the x axis and 2 µm along the y axis if the trap centre is at (0, 0). It then moves along the x axis for 4 µm, then the y axis for -40 nm, then the x axis for -4 µm, then the y axis for -40 nm, and so on. The schematic diagram on the top right sketches the trace of the bead movement. It scans 101 horizontal lines. The plot below it is the zoom-in plot on the 37th scan in which the vertical signal is at a minimal, indicating that the 37th scan is closest to the laser trap centre. This plot is used for the calibration. (a) Vertical scan.

calibration trace while all the other 100 scannings are discarded. The trace on the left of figure 2.5 (a) shows V_{LR}/V_{SUM} and V_{TB}/V_{SUM} for the horizontal scan. The blue vertical signal V_{TB}/V_{SUM} is ideally zero when the scan line coincides the trap centre. In the figure the blue signal is never exactly zero but it is at a minimum during the 37th scan. It has been selected as the calibration curve - see the figure to the right. The behaviour of the yellow V_{LR}/V_{SUM} signal also makes sense - when the bead is close to the trap centre, movement of the bead results in maximum V_{LR}/V_{SUM} amplitude (the 37th scan) while lines away from the centre see lower and lower amplitudes. Figure 2.5 (b) shows the vertical 2D scan.

The nanostage displacement is recorded for every QPD voltage reading so the multiplication factor between them can be established in the linear region of the voltage readings:

$$x = \sigma_x \frac{V_{LR}}{V_{SUM}}, \quad \sigma_x = 1.19\,\mu\mathrm{m\,V}^{-1} \tag{2.1}$$

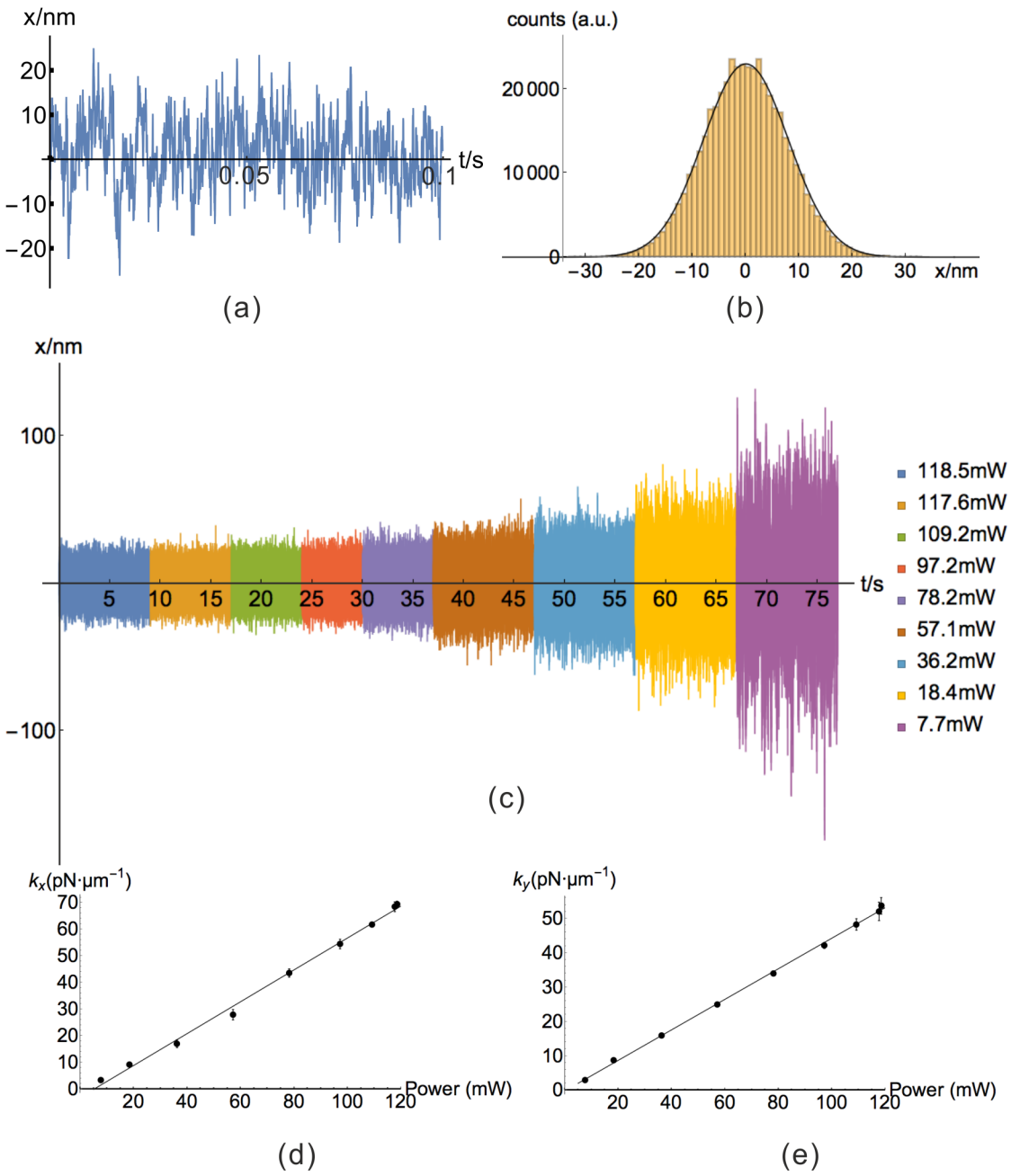

Figure 2.6: Stiffness of the trap obtained with the equipartition theorem method. (a) A small sample of x-displacement data showing the confined Brownian motion of the 3 µm magnetic bead trapped at 6 µm away from the coverslip with 118.5 mW laser power measured at the condenser exit. (b) Corresponding histogram of the positions occupied by the bead, fit with a Gaussian envelope. (c) Displacements of the bead at various laser powers (measured at the bfp of the condenser) are juxtaposed for easy comparison of the amplitude of the bead movement. High laser powers on the left have tighter movement whereas low laser powers on the right see freer movement. (d) The corresponding stiffness is calculated with equation 1.10. (e) The stiffness measurement for the y-axis. The error bars in (d) and (e) are standard deviation over two repetitions of measurement. Note that the linear fits do not pass through the origin due to systematic errors - for example, the diameter of the magnetic bead is 3 µm in the calculations but it actually varies within a Normal distribution.

$$y = \sigma_y \frac{V_{TB}}{V_{SUM}}, \quad \sigma_y = 1.44\,\mu\mathrm{m\,V}^{-1} \tag{2.2}$$

where x and y are displacements relative to the trap centre. From now on, all QPD voltage time series signals will be converted to displacement time series. The LabVIEW code for controlling the nanostage can be found in A.3.

A magnetic bead is trapped at various laser powers and the displacement trace recorded. A typical sample is show in figure 2.6 (a). The bead fluctuates by Brownian motion while its mean position is confined to the trap centre. The distribution of the motion is Gaussian, as can be seen in figure 2.6 (b). Higher laser power reduces the amplitudes of bead Brownian motion. Figure 2.6 (c) shows the least bead motion on the left, which has highest laser power. The motion increases towards the right of the plot due to reduction in laser power. The power is measured next to the condenser back focal plane so the power at the trap will be higher. Increasing the laser power linearly increases the trap stiffness, which is shown in figure 2.6 (d) with the linear fit. The laser is not exactly centred at the QPD centre (due to the beam profile, which in practice is not perfectly circularly symmetrical) so all displacement measurements will have a systematic offset, which is different for different laser powers. This offset needs to be removed. Subtracting the mean of the data from the data can remove the offset. The data are denoted as $x_1, x_2, ..., x_n$ so the mean is

$$\overline{x} = \frac{x_1 + x_2 + ... + x_n}{n} \tag{2.3}$$

and after removal, $x_1 = x_1 - \overline{x}$, $x_2 = x_2 - \overline{x}$, etc. Then the data are used to find the mean squared displacement:

$$< x^2 >= \frac{x_1^2 + x_2^2 + ... + x_n^2}{n} \tag{2.4}$$

Equation 2.4 is then plugged into equation 1.10 to find k_x. Figure 2.6 (e) shows the stiffness-power relationship in the y-direction.

The same QPD signals from the above is used for the power-spectrum method of obtaining the stiffness. The data, $x_1, x_2, ...x_n$ (after subtraction of mean), are first discrete-Fourier transformed into a list $v_1, v_2, ...v_n$ where v_s is:

$$v_s = \frac{1}{\sqrt{n \cdot f_{sample}}} \sum_{r=1}^{n} x_r e^{2\pi i(r-1)(s-1)/n} \tag{2.5}$$

where $f_{sample} = 50\,\text{kHz}$ is the sampling rate. Then v_s is taken absolute value and squared to get the power spectrum discrete series. Only the first $n/2$ data points are taken as the rest are redundant (repetitions of the first $n/2$ data):

$$\text{PSD}(v_s) = \{2|v_1|^2, 2|v_2|^2, ...2|v_{n/2}|^2\} \tag{2.6}$$

The factor of 2 in front of $|v_s|^2$ reflects the fact that the PSD is a one-sided PSD - see equation 1.18. The frequency is obtained by

$$f_s = \frac{s}{T} \tag{2.7}$$

where T is the total acquisition time. Since $T = n/f_{sample} = n/50000$,

$$f_s = 50000\frac{s}{n} \tag{2.8}$$

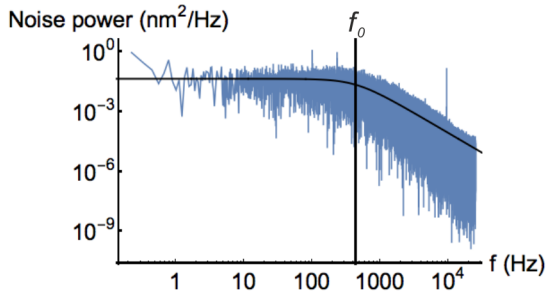

(a)

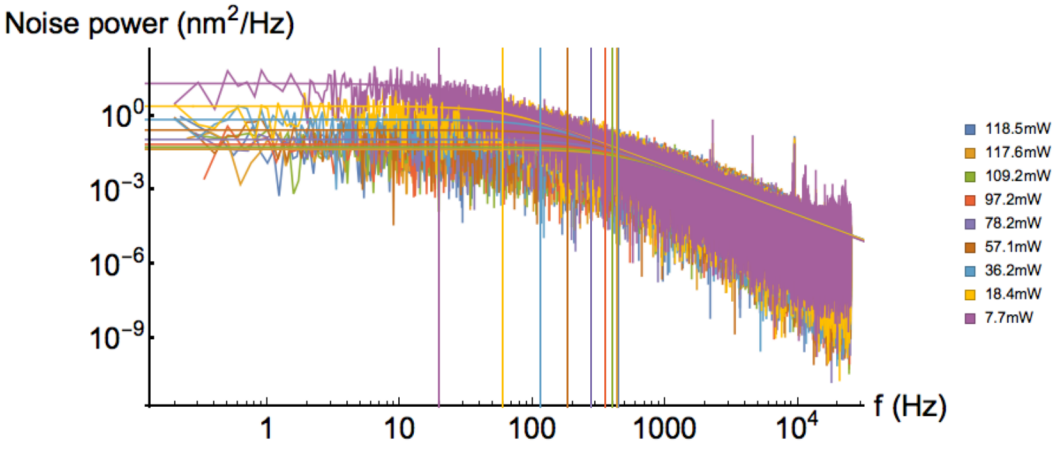

(b)

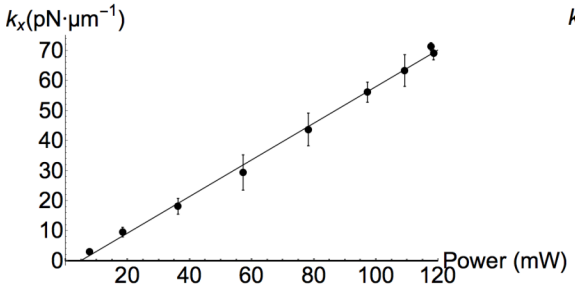

(c)

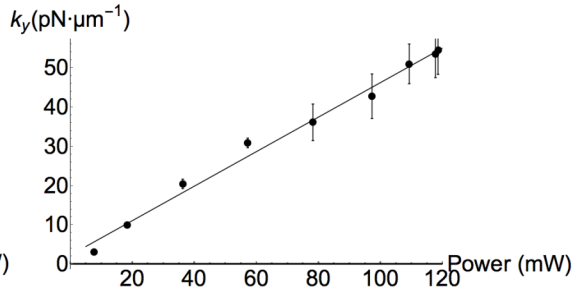

(d)

Figure 2.7: Stiffness of the trap obtained with the power spectrum method. (a) The log-log scale plot of the power spectral density (PSD) *vs* frequency plot of x-displacement data taken on the 3 µm magnetic bead trapped at 6 µm away from the coverslip with 118.5 mW laser power measured at the condenser exit. The corner frequency is labelled with the vertical line. (b) PSD plots of various laser powers with their respective corner frequencies juxtaposed. (c) and (d) are the stiffness *vs* power plot for x- and y- direction measurements. The error bars in (c) and (d) are standard deviation over two repetitions of measurement. See figure 2.6 (d) and (e) for a comparison to the stiffness values obtained with the equipartition theorem method.

Combine f_s with PSD(v_s), we get the plottable data set:

$$\text{PSD}(v_s) = \{(50000\frac{1}{n},\ 2|v_1|^2), (50000\frac{2}{n},\ 2|v_2|^2), ..., (50000\frac{n/2}{n},\ 2|v_{n/2}|^2)\} \tag{2.9}$$

In the above analysis, no windowing function is applied before Fourier transformation and no noise reduction is done. Figure 2.7 (a) shows a typical PSD(v_s) *vs* f_s plot (laser power

= 118.5 mW) in log-log scale. The data are fit with equation 1.36, with fitting parameters $A = \frac{k_B T}{\gamma \pi^2}$ and $B = f_0$:

$$\text{PSD}(x, f) = A \frac{1}{f^2 + B^2} \tag{2.10}$$

The fitting uses Levenberg–Marquardt method for least-squares fit, which is implemented with the built-in function "FindFit" in Wolfram Mathematica. Also, for the fitting, the first 9 PSD data points are ditched as they swing widely. They correspond to signals under 1 Hz so they are mostly due to noises in the lab and to a much less extent due to Brownian motion. The corner frequency (f_0 =438 Hz) is labelled with a vertical line in the plot. Figure 2.7 (b) juxtaposes PSD at various laser powers. It can be seen that the corner frequencies increase with laser power. Only PSDs for the x-axis are shown. Figure 2.7 (c) and (d) are plots of stiffness *vs* laser power with linear fit. See figure 2.6 (d) and (e) for the same plots obtained with the equipartition theorem method - the two methods give nearly the same values.

The fact that with the PSD method of obtaining the stiffness there is no need to calibrate the QPD (ie. to create a look up table between QPD signal and bead displacement) is not only a convenience of using the PSD method but also means that σ_x and σ_y in equations 2.1 and 2.2 can be calculated with A (see equation 2.10) obtained from the fitting. For example, to obtain σ_x,

$$k_x = \frac{k_B T}{< x^2 >} = \frac{k_B T}{< \left(\sigma_x \frac{V_{LR}}{V_{SUM}} \right)^2 >} \tag{2.11}$$

Rearrange the above equation:

$$\sigma_x = \sqrt{\frac{k_B T}{k_x < \left(\frac{V_{LR}}{V_{SUM}} \right)^2 >}} \tag{2.12}$$

Using k_x and k_y obtained from the power spectrum method and voltage values from the QPD, the calculation gives

$$\sigma_x = 1.15\,\mu\text{m}\,\text{V}^{-1} \tag{2.13}$$

$$\sigma_y = 1.40\,\mu\text{m}\,\text{V}^{-1} \tag{2.14}$$

which are close enough to the measured values.

Finally, let's compare the theoretical and experimental values for A. The theoretical A is:

$$A = \frac{k_B T}{\gamma \pi^2} = \frac{1.38 \times 10^{-23} \times 300}{6 \pi \eta r \pi^2} \tag{2.15}$$

If we use the viscosity of water at 25°C, $\eta = 8.9 \times 10^{-4}\,\text{Pa}\,\text{s}$, and radius of bead, $r = 1.5 \pm 0.075\,\mu\text{m}$, then

$$A = 1.67 \pm 0.08 \times 10^{-14} \text{m}^2\,\text{s}^{-1} \tag{2.16}$$

The error is from the standard deviation in the radius of the magnetic bead, which is supplied by the manufacturer - see table 3.1. The experimentally obtained values for the various laser powers have mean and standard deviation of $1.75 \pm 0.08 \times 10^{-14}\,\text{m}^2\,\text{s}^{-1}$, agreeing with the theoretical values. The algorithm to calculate the above can be found in appendix A.1.

I also probed the stiffness as a function of trapping depth into the flow cell. This

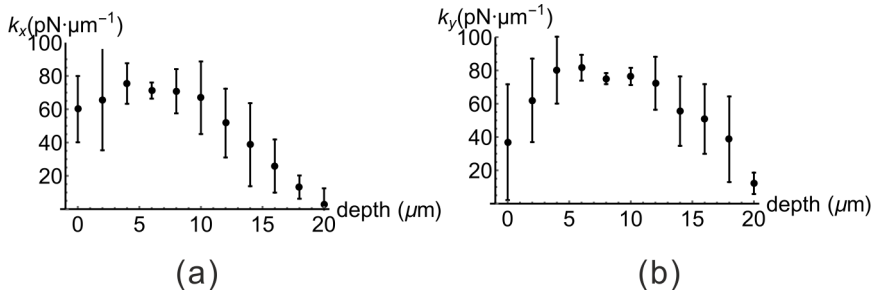

Figure 2.8: Stiffness as a function of trapping depth for the $3\,\mu\mathrm{m}$ magnetic bead in the (a) x- and (b) y- directions.

dependence is due to spherical aberration (the axial rays of a lens refract less than the peripheral rays so they are not brought into the same focus), which in the case of optical tweezers occurs because of a mismatch between the refractive index of the coverslip and the sample solution. The aberration broaden the focus volume mostly axially but also radially, which weakens the optical trap in the axial as well as the radial directions. The decrease of k can be observed when the coverslip is positioned further away from the traps [128, 129]. Using a water immersion objective lens reduces the spherical aberrations, as the mismatch between the oil and the sample solution is reduced [130].

We define the depth d as the separation between the bottom surface of the bead and the top surface of the coverslip. For example, when $d = 0\,\mu\mathrm{m}$, the bead just touches the coverslip. To change d, the laser trap is held stationary and the nanostage is programmed to move along the z-axis. The nanostage is initially positioned such that $d = 0\,\mu\mathrm{m}$. Then the nanostage moves downwards towards the objective lens, in $2\,\mu\mathrm{m}$ steps. The QPD readings are taken at the end of each movement step. Figure 2.8 shows the relationships for both k_x and k_y with a laser power of 120 mW. The peak stiffness is found to be approximately 6 $\mu\mathrm{m}$.

Note that for very low depth the stiffness also decreases because of Faxen's Law, which states that the drag experienced by a bead increases as the bead is close to a surface.

2.4 Bead height

Figure 2.9 shows definitions of bead height and laser focus height. d_3 is referred to in section 2.3 as "bead depth", but it is a different name that has the same meaning as bead height. Reason (i) in the above paragraph demands that $d_3 = 1\,\mu\mathrm{m}$, assuming that the radius of the anti-DIG bead is $5\,\mu\mathrm{m}$ and that of the magnetic bead is $3\,\mu\mathrm{m}$. In reality bead radius varies among individuals so suitable d_3 will be determined experimentally. From section 2.3 we know that $d_3 = 6\,\mu\mathrm{m}$ maximises the trapping stiffness so here I have to make the compromise of trapping at a lower stiffness with $d_3 < 6\,\mu\mathrm{m}$. Bead height needs to be measured and controlled because (i) the DNA needs to lie in the axial plane for fluorescence imaging. One end of the DNA has fixed height due to the immobilisation to the big anchoring bead and height at the other end is set by axial positioning of the trapped bead. (ii) The trapping stiffness varies with bead height as discussed above in section 2.3 so the height needs to be consistent throughout experiments to make sure that the stiffness stays consistent. (iii) The drag force on the particle is described by the Stokes' law with Faxen's law correction [131], which, in summary, says the drag increases when the bead approaches the coverslip. This needs to be consistent and quantified across experiments.

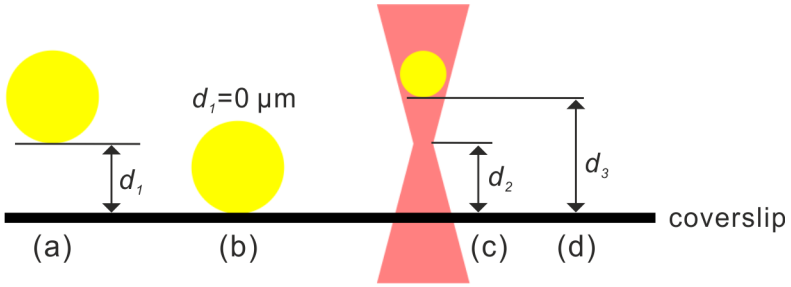

Figure 2.9: Definition of bead height and laser focus height. (a) The separation between the 5 µm polystyrene anti-DIG bead and the coverslip surface, which is always 0 µm, as shown in (b). (c) The separation between the laser focus and the coverslip is denoted d_2. (d) The separation between the 3 µm magnetic bead and the coverslip surface is denoted d_3.

Notably, $d_3 - d_2$ is variable. It is larger when the magnetic content is higher - again there are slight differences among beads. So in summary, I need to be able to quantify d_2, d_3 and $d_3 - d_2$.

The line profile through the centre of the bead is plotted. In a biomolecule experiment, a bead image has its line profile plotted, which is compared to the calibration profiles by least square method to find the height. The measurement is done with camera image analysis. Laser-based height tracking is discussed in chapter 6 discussion though it has not been implemented here. The bead is immobilised to coverslip surface by non-specific adsorption. It then is moved along the z-direction with the nanostage in 50 nm steps for 10 µm so the scanning more than covers the extent of the bead. At the end of each movement step, an image is taken.

I obtain d_3 by evaluating $(d_3 - d_2) + d_2$, of which $(d_3 - d_2)$ is known from above so I will also need to measure d_2, the height of the laser focus above the coverslip. This can be done by repeating the calibration process above but with the anti-DIG bead. We know the anti-DIG bead is fixed on the coverslip, so when it is in focus, the focus is one radius above the coverslip. Other positions can be obtained by measuring the amount by which the anti-DIG bead is out-of-focus. Again I plot a line profile across the bead centre and compare bio-experiment anti-DIG bead profiles to the calibration profiles to obtain d_2. Figure 2.12 shows a reslice plot - orthogonal slices through the image volume - of the bead image. The horizontal axis is the image profile and the vertical axis is the number of slices. This time the style of representation is different from that in figure 2.10 but the calibration method is identical. Now that both $(d_3 - d_2)$ and d_2 are obtained, we can calculate d_3 by adding them.

In a DNA tether experiment, an anti-DIG bead is immobilised on the coverslip surface while the magnetic bead is trapped. The trapped bead will need to be brought to a height so that its centre coincides the centre of the anti-DIG bead. I do not use the degree of convergence of the laser beam to control the magnetic bead height, as the beam is set to be maximally convergent for the most efficient trapping. I instead use the nanostage to bring the anti-DIG bead closer to or away from the trapped bead. Figure 2.11 shows five different nanostage z-positions with both types of beads in the field of view. The trapped bead is approximately the same height above the laser focus across different positions of the nanostage (taken into consideration Brownian force that nudges the bead up and down), which is why the trapped bead has similar appearances in figure 2.11 (b) and (c).

However, it does slightly move up or down depending on the height of the nanostage

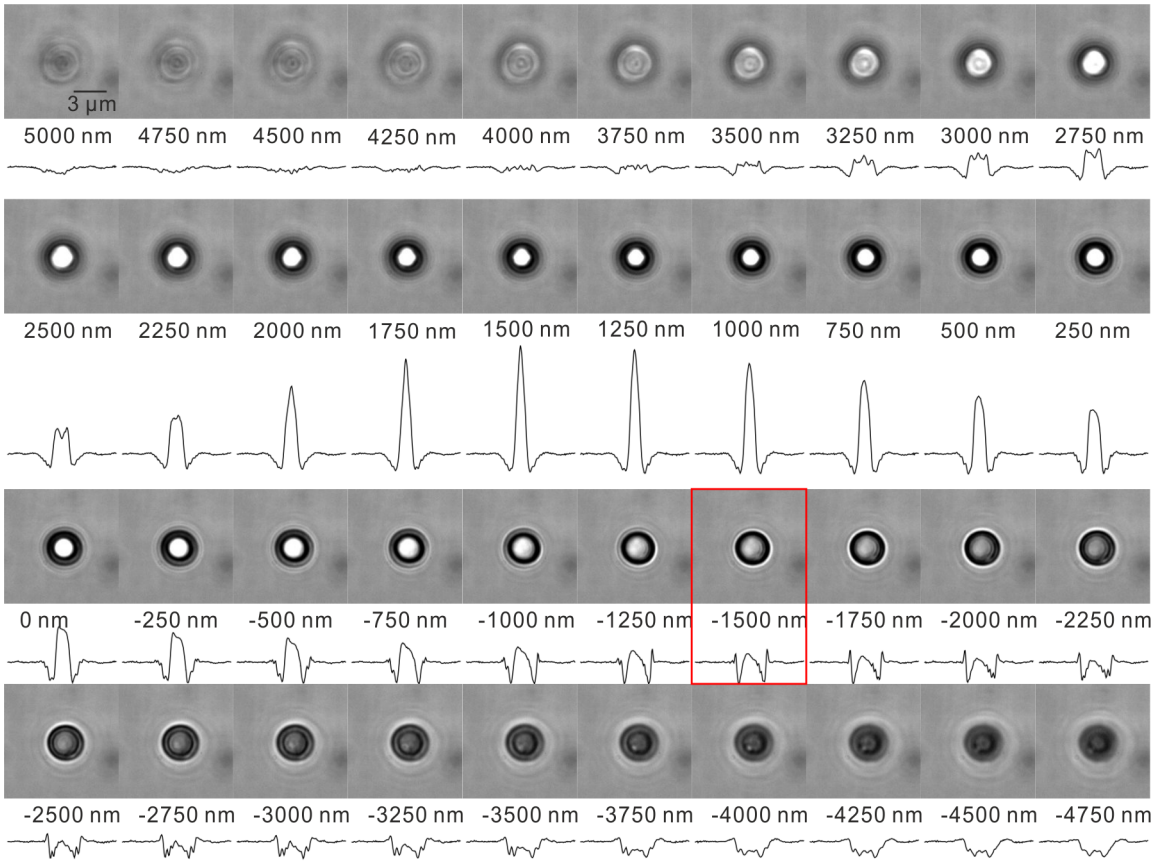

Figure 2.10: Bright field images of magnetic bead taken at various $d_3 - d_2$. The line profile of each image accompanies the image. The bead in focus is highlighted with a red rectangle. The distance labelled for each image is $d_3 - d_2$, which is why the rectangled bead has a value of -1500 nm, namely the radius of the bead.

due to the spherical aberration caused by how thick the layer of sample solution the laser has to penetrate. For example, the appearance of the trapped bead in (a) is noticeably different because the coverslip is so far out.

The five snapshots are selected from a series of 200 images taken at equally-spaced nanostage heights (which are also the images used to compile figure 2.12) so I know the positions of each image relative to a reference image, say figure 2.11 (b). I decide that, in (b), the anti-DIG is in focus by inspection (sharpest edge, or least diffraction). There are multiple approaches to work out which image among the 200 corresponds to the assay configuration, shown in (c): (1) the trapped bead is found to be $d_3 - d_2 = 0.6\,\mu\text{m}$ above the laser focus by comparing its profile to the calibration profiles (figure 2.10). The radii of the two beads and their coinciding height of centres suggest that the bottom of the trapped bead should be $d_3 = 1\,\mu\text{m}$ above the coverslip. Therefore, the focus should be at $d_2 = 1 - 0.6 = 0.4\,\mu\text{m}$ above the coverslip. I select the image that is $2.5 - 0.4 = 2.1\,\mu\text{m}$ below the image in (b) to be the image of the assay configuration. (2) Following the first method, we know $d_2 = 0.4\,\mu\text{m}$. I work out the line profile of the anti-DIG bead when $d_2 = 0.4\,\mu\text{m}$. Then I select the image that matches the profile. (3) I can determine the "touch" moment in figure 2.11 (d) since the magnetic bead noticeably jiggles when moving into that frame. The number of frames between figure 2.11 (b) and the "touch" frame allows the determination of how far the nanostage has travelled and therefore the amount

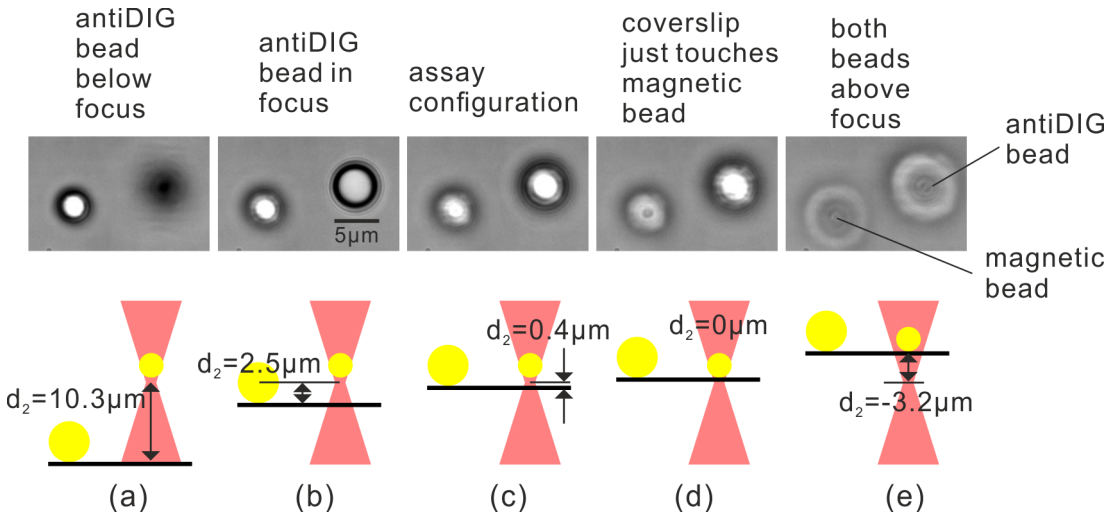

Figure 2.11: An anti-DIG bead is tethered to the coverslip whereas a magnetic bead is trapped with the laser trap. The nanostage is then commanded to rise in position while the objective lens fixed in position. From (a) to (d) the coverslip moves closer and closer to the magnetic bead so the anti-DIG bead changes appearance. The magnetic bead is more or less fixed with respect to the objective focus so appears to be the same. From (d) to (e) the coverslip pushes upward both beads so they change appearance together.

by which the trapped bead is above the anti-DIG bead. Then in another experiment, from the positions in (b), the nanostage can move up a calculable amount to bring the configuration into figure (c). This method does suffer from the fact that once the trapped bead comes into contact with the coverslip, it immobilises so this combination of magnetic and anti-DIG beads is no longer usable. Also the closeness of the coverslip to the trapped bead potentially causes the position of the trapped bead to shift.

On a different note, it is seen in figure 2.11 (c) that the DNA molecule will always be placed above the imaging plane, as the trapped bead is above the laser focus. Assuming the diameter of the anti-DIG bead is $2.5\,\mu\mathrm{m}$ and the DNA tethers to the height of the centroid of both beads, then the DNA is $2.1\,\mu\mathrm{m}$ above the focal plane for the case shown in figure 2.11 (c). The value will change due to variances in bead diameter and magnetic contents, but the value will be in the vicinity of $2.1\,\mu\mathrm{m}$. To image the DNA onto the camera, an extra pair of lenses are placed in the imaging path - see figure 2.13 (a) bottom diagram - which we call the "correction module". The effective focal length of the correction module-objective lens combination is now the distance between the objective and the DNA. One concave lens can theoretically achieve the same effect but having a concave-convex pair mounted on sliding rods (Thorlabs' cage system, CP09/M, ER4) allows easy adjustment of the focus to accommodate different DNA height in experiments.

Assuming the bead is $o = 2.1\,\mu\mathrm{m}$ above the focal plane, where o means object distance, the focal length of the objective lens is f_{obj}, then from the thin lens equation, the image distance is

$$\frac{1}{o} + \frac{1}{i} = \frac{1}{f_{obj}} \Rightarrow i = 1907\,\mathrm{mm} \tag{2.17}$$

Therefore we need a correction module that is about $-1907\,\mathrm{mm}$ to recollimate the image at

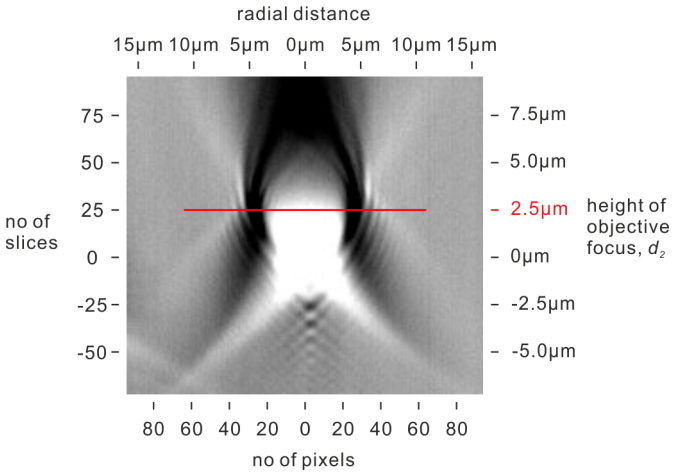

Figure 2.12: Reslice plot of anti-DIG bead images. Bright field images of anti-DIG bead are taken at various d_2. The line of pixels through the centre of the bead is extracted from each image and stacked up to form this reslice plot. The red line indicates when the bead is in focus, corresponding to when $d_2 = -2.5\,\mu\text{m}$.

infinity. The focal length for the dual-lens system, f is given by

$$\frac{1}{f} = \frac{1}{f_1} + \frac{1}{f_2} - \frac{d}{f_1 f_2} \tag{2.18}$$

where f_1 and f_2 are the focal lengths of the two lenses and d is the physical separation between the two lenses, which can be changed easily by sliding the lenses along the cage rods. Many combinations of parameter values can make $f = -1907\,\text{mm}$. We choose $f_1 = -100\,\text{mm}$, $f_2 = 150\,\text{mm}$ and $d = 58\,\text{mm}$ to make the correction module, as these lenses are of "standard" focal lengths and $d = 58\,\text{mm}$ is short enough to fit into the imaging path.

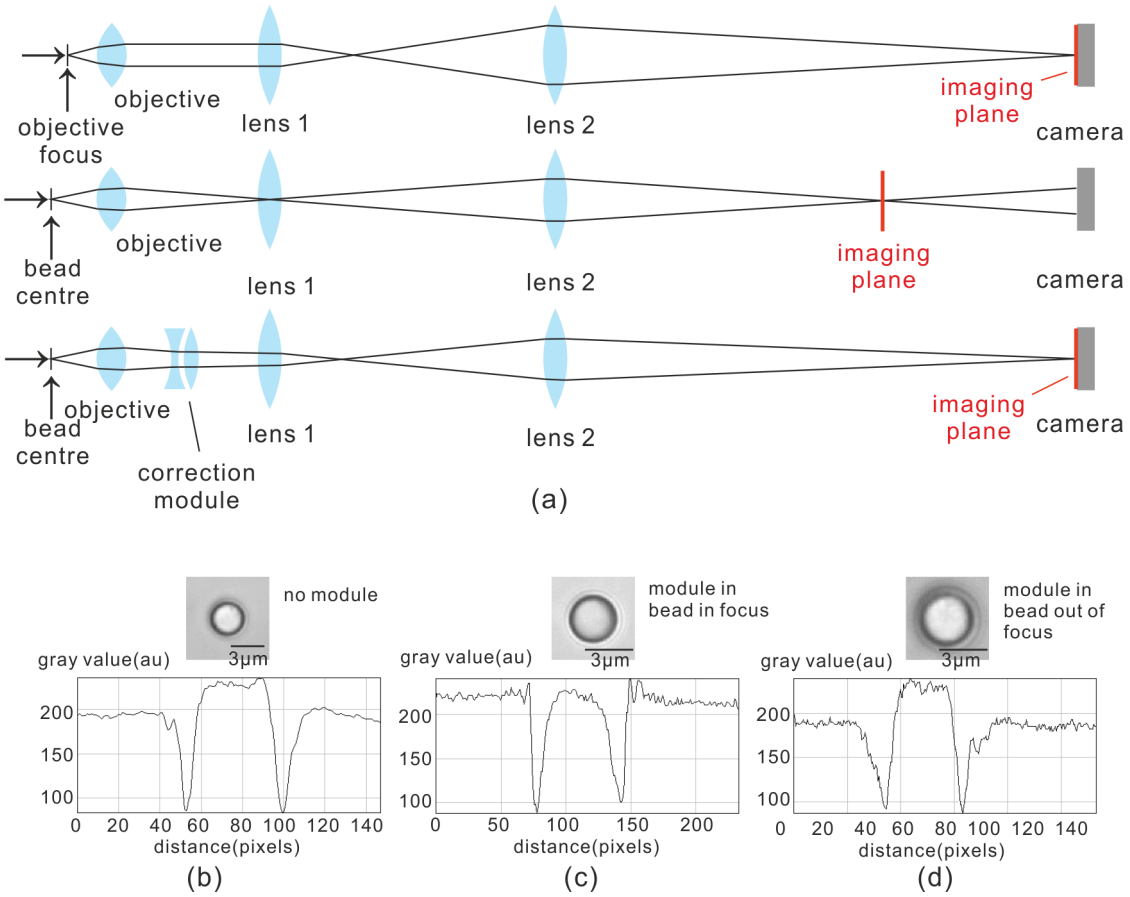

Figure 2.13: A correction module composed of a lens pair brings the DNA and trapped bead into focus. (a) Optical trace diagrams. Top: The image of the object at the objective focus is formed by the objective and a pair of relay lenses onto the camera. Middle: the DNA is above the focus, at the bead centre, which, without the correction module, does not image on the camera. The imaging plane is labelled with a red line. Bottom: the correction module is inserted between the objective and the relay lenses. It re-collimates the light exiting the objective so it is imaged on the camera. (b) Appearance of the trapped bead without the correction module. The bead is in focus - compare the line profile to that in figure 2.10. (c) Appearance of the trapped bead with the correction module. (d) With the correction module, the strength of which is set at a "wrong" value. This is to show that the module has flexible focal lengths to accommodate DNA at various heights.

Chapter 3

Magnetic tweezers

The design, construction and calibration of the magnetic tweezers that is a part of the MOT are described in detail in this chapter. Theories in electromagnetism that are needed to explain the mechanism of the instrument are also introduced for a logical and complete narrative. I also include computer codes that arise from the controlling of the hardware and the analysis of the measurement data.

3.1 Electromagnetism

Relevant theories in electromagnetism are introduced in this section, including how magnetic field is created, the nature of the magnetisation of magnetic beads, how magnetic beads experience a force and torque in a magnetic field, and so on.

3.1.1 Magnetic field of a current loop

Magnetic field is created by electric current. A wire carrying a steady current I generates a $\mathbf{B}$ field at position $\mathbf{r}$ given by the Biot-Savart law:

$$\mathbf{B}(\mathbf{r}) = \frac{\mu_0}{4\pi} \int_C \frac{I d\mathbf{l} \times \mathbf{r}'}{|\mathbf{r}'|^3} \tag{3.1}$$

where $d\mathbf{l}$ denotes differential length of the wire in the conventional direction of the current, $\mathbf{r}'$ denotes the vector pointing from position $\mathbf{l}$ on the wire to $\mathbf{r}$. $\mu_0 = 4\pi \times 10^{-7} \mathrm{N\,A^{-2}}$ is the permeability of free space. It is a good approximation for the permeability of air where the wire is assumed to be in.

Below I calculate the magnetic field due to a circular loop of wire carrying a current, which will be useful later in the evaluation of the field due to the magnetic tweezers. Figure 3.1 shows the wire in red. The point where $\mathbf{B}$ is evaluated is labelled $\mathbf{r}$. The circular symmetry of the geometry results in zero $\mathbf{B_x}$ and $\mathbf{B_y}$, the components of $\mathbf{B}$ along the two radial directions. Denote the radius of the loop as R, Biot-Savart law in the z direction reads:

$$B_z(\mathbf{r}) = \frac{\mu_0 I R}{4\pi |\mathbf{r}'|^3} \int_C dl \tag{3.2}$$

Further denote $z = |\mathbf{r}|$, we have $|\mathbf{r}'| = \sqrt{(R^2 + z^2)}$, and

$$B_z(\mathbf{r}) = \frac{\mu_0 I R}{4\pi (R^2 + z^2)^{3/2}} 2\pi R = \frac{\mu_0 I R^2}{2(R^2 + z^2)^{3/2}} \tag{3.3}$$

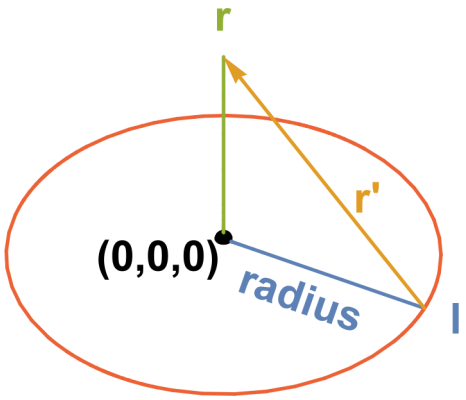

Figure 3.1: Schematics of a current carrying loop centred at the origin.

3.1.2 The superparamagnetic bead

The magnetic beads that I use have a diameter of 3 µm. The core of the beads are made of styrene-maleic acid (SMA) copolymer. The core is covered in a shell of magnetite [CAS: 1317-61-9]. The shell is protected in another thin layer of polymer. Finally the surface is functionalised with streptavidin [CAS: 9013-20-1]. Figure 3.2 (a) shows the structure of the bead. Table 3.1 summarises selected characters of the bead.

product name	micromer®-M
product code	08-19-303
surface	streptavidin
bead diameter	$3\,\mu\mathrm{m}$
coefficient of variation in diameter	$< 5\%$
bead volume	$1.41 \times 10^{-17}\,\mathrm{m}^3$
density	$1100\,\mathrm{kg\,m}^{-3}$
bead mass, m_b	$1.56 \times 10^{-14}\,\mathrm{kg}$
solid content per solution	$25\,\mathrm{mg\,mL}^{-1}$
magnetisation, $\mathbf{M}$	$5.4\,\mathrm{A\,m}^2\,\mathrm{kg}^{-1}$ ($H = 80\,\mathrm{kA\,m}^{-1}$)
magnetisation per bead, $\mathbf{M_b}$	$8.4 \times 10^{-14}\,\mathrm{A\,m}^2$
saturation magnetisation, $\mathbf{M_{sat}}$	$6.6\,\mathrm{A\,m}^2\,\mathrm{kg}^{-1}$ ($H > 800\,\mathrm{kA\,m}^{-1}$)
no. of beads per mL solution	1.6×10^9
streptavidin wt per bead wt	$700\,\mathrm{ng\,mg}^{-1}$
streptavidin wt per one bead	$1.1 \times 10^{-5}\,\mathrm{ng}$
streptavidin no. per one bead	1.2×10^5
material	magnetite, Fe_3O_4
Fe_3O_4 content (wt)	$9 - 14\%$
Fe content (wt)	$6 - 10\%$
substrate	styrene-maleic acid copolymer

Table 3.1: Some properties of the 3 µm superparamagnetic bead.

The superparamagnetic bead has no residual magnetisation after the removal of external magnetic field. With the presence of external field, the bead develops magnetisation that is proportional to the external field at low field and reaches a plateau at high field. The magnetisation per unit mass as a function of external magnetic field, $\mathbf{B}$, is given by the Langevin function:

$$\mathbf{M}(\mathbf{B}) = \mathbf{M_{sat}} \left(\coth(\mathbf{B}/\mathbf{B_0}) - \frac{1}{\mathbf{B}/\mathbf{B_0}} \right) \tag{3.4}$$

where $\mathbf{M_{sat}}$ is the saturated magnetic moment per unit mass at high $\mathbf{B}$ and, for our

purposes, $\mathbf{B_0}$ is a fitting parameter. Table 3.1 gives $\mathbf{M} = 5.4\mathrm{A\,m^2\,kg^{-1}}$ at $\mathbf{H} = 80\,\mathrm{kA\,m^{-1}}$ (ie. $\mathbf{B} = 0.1\,\mathrm{T}$) and $\mathbf{M_{sat}} = 6.6\mathrm{A\,m^2\,kg^{-1}}$ at $\mathbf{H} > 800\,\mathrm{kA\,m^{-1}}$ (ie. $\mathbf{B} > 1.0\,\mathrm{T}$), which allows us to fit the Langevin equation to get $\mathbf{B_0} = 0.018\,\mathrm{T}$. Figure 3.2 (b) shows a plot of the fitted

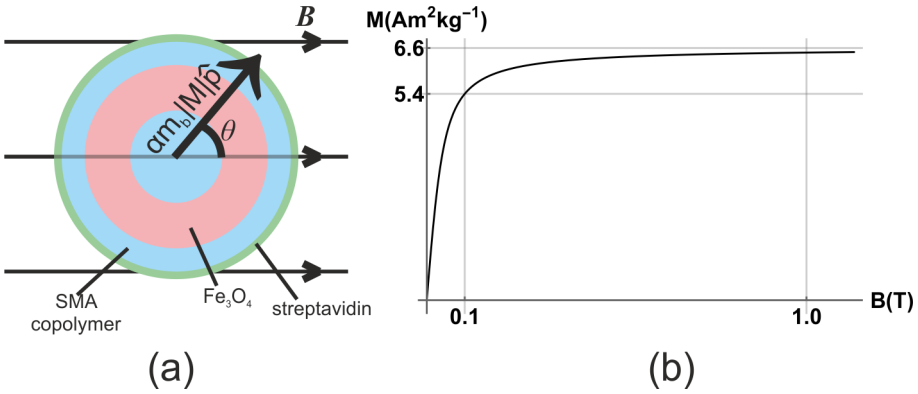

Figure 3.2: Superparamagnetic beads. (a) Structure of the superparamagnetic bead. (b) A plot of its magnetisation with respect to the external field. The gridlines cross at two points on the curve where magnetisations and the respective background fields are supplied by the manufacturer.

curve. Admittedly two data points are not many for fitting the Langevin function and the curve is only as good as the accuracy of the two points. The Langevin function can be approximated below at low field and at high field:

$$\mathbf{M}(\mathbf{B}) = \frac{\chi}{\mu_0}\mathbf{B} \qquad \text{for} \qquad \mathbf{B} \ll \mathbf{B_{sat}} \tag{3.5}$$

$$\mathbf{M}(\mathbf{B}) = \mathbf{M_{sat}} \qquad \text{for} \qquad \mathbf{B} \geq \mathbf{B_{sat}} \tag{3.6}$$

where $\mathbf{B_{sat}}$ is the magnetic field high enough for $\mathbf{M}$ to saturate and χ is the magnetic susceptibility.

The magnetisation of a bead composes of the sum of two components, $\mathbf{M_b} = \mathbf{M_{b1}} + \mathbf{M_{b2}}$. Let m_b denote the mass of a magnetic bead, then $\mathbf{M_{b1}} = m_b\mathbf{M}$. It is the nature of superparamagnetic beads that $\mathbf{M_{b1}}$ is intrinsically aligned with $\mathbf{B}$ regardless of the orientation of the beads themselves. $\mathbf{M_{b2}}$ comes from the fact that the beads have a preferential axis along which a small magnetisation proportional to $m_b|\mathbf{M}|$, in the direction of $\hat{\mathbf{p}}$, is created. Let the constant of proportionality be α, then $\mathbf{M_{b2}} = \alpha m_b|\mathbf{M}|\hat{\mathbf{p}}$. The direction of $\hat{\mathbf{p}}$ is fixed with respect to the bead orientation so can form an angle, θ, with $\mathbf{B}$. See figure 3.2 (a). It is the angular offset of $\mathbf{M_{b2}}$ from the $\mathbf{B}$ field that results in the torque. In summary,

$$\mathbf{M_b} = m_b\mathbf{M} + \alpha m_b|\mathbf{M}|\hat{\mathbf{p}} \tag{3.7}$$

Magnetic force and torque applied on the bead are given in equations 1.6 and 1.7 and reproduced below with slight annotation changes:

$$\mathbf{f} = (\mathbf{M_b} \cdot \nabla)\mathbf{B} \tag{3.8}$$

$$\boldsymbol{\tau} = \alpha m_b|\mathbf{M}]\hat{\mathbf{p}} \times \mathbf{B}\cos\theta \tag{3.9}$$

The $\cos\theta$ in equation 3.9 comes from the fact that only the component of $\mathbf{B}$ that is in the direction of the preferential axis induces $\mathbf{M_{b2}}$. Physically, the force tends to move the bead

towards higher $\mathbf{B}$ and the torque tends to rotate the bead so that θ is reduced to zero. The magnitude of $\mathbf{f}$ scales with the gradient of $\mathbf{B}$ whereas the magnitude of $\boldsymbol{\tau}$ scales with $\mathbf{B}$ itself.

3.1.3 Magnetic torque on the bead

At low field, k_θ scales quadratically with $\mathbf{B}$; at high field, k_θ scales linearly with $\mathbf{B}$. From equation 1.37 and 3.9,

$$k_\theta \propto \tau \propto |\mathbf{M}||\mathbf{B}| \tag{3.10}$$

Substitute equations 3.5 and 3.6 into equation 3.10 to express $\mathbf{M}$ at the small and large field scenarios:

$$k_\theta \propto |\mathbf{B}||\mathbf{B}| = |\mathbf{B}|^2 \qquad \text{for} \qquad \mathbf{B} \ll \mathbf{B_{sat}} \tag{3.11}$$

$$k_\theta \propto |\mathbf{M_{sat}}||\mathbf{B}| \propto |\mathbf{B}| \qquad \text{for} \qquad \mathbf{B} \geq \mathbf{B_{sat}} \tag{3.12}$$

Further from equation 3.3, we have

$$k_\theta \propto I^2 \qquad \text{for} \qquad \mathbf{B} \ll \mathbf{B_{sat}} \tag{3.13}$$

$$k_\theta \propto I \qquad \text{for} \qquad \mathbf{B} \geq \mathbf{B_{sat}} \tag{3.14}$$

Equation 3.13 will be used for the evaluation of k_θ for our setup since the MT is designed for low and measurable torque application.

3.2 Instrument design

This section explains the experimental requirements and the restriction posed by the microscope that led me to the instrument design. Also the design is described in detail including the electromagnets and the driving circuits.

3.2.1 The coils and the spools

The filamentous biomolecule will be laid in a transverse orientation so that its contour can be imaged with fluorescence microscopy. Forces and torques are applied to the molecule to probe its response to the combination of them. The magnetic tweezers are used to apply only torque, which requires the $\mathbf{B}$ field to be rotatable and uniform in space. Two pairs of current-carrying coils arranged at right angle to each other can achieve both. Figure 3.3 depicts the spatial arrangement of the coils in our tweezers. The dimensions are drawn to scale. Although a third pair of coils allows rotation along any angle in three dimensions (as opposed to just the x-axis), that capability is excessive for our purpose. Also the aperture in the nanostage prevents the implementation of a third pair of coils. Ideally, Helmholtz coil pairs - coil pairs which have the property that radius is equal to the separation between coils - should be used because they maximise the uniformity of the $\mathbf{B}$ field. Due to the constrains posed by other modules such as the microscope and nanostage, the separation between coils in our setup is larger than the radius of the coils. However, the field in the geometric centre of the coils where the biological assay is placed is still quite uniform. A plot of spatial distribution of the $\mathbf{B}$ field is shown in figure 3.7.

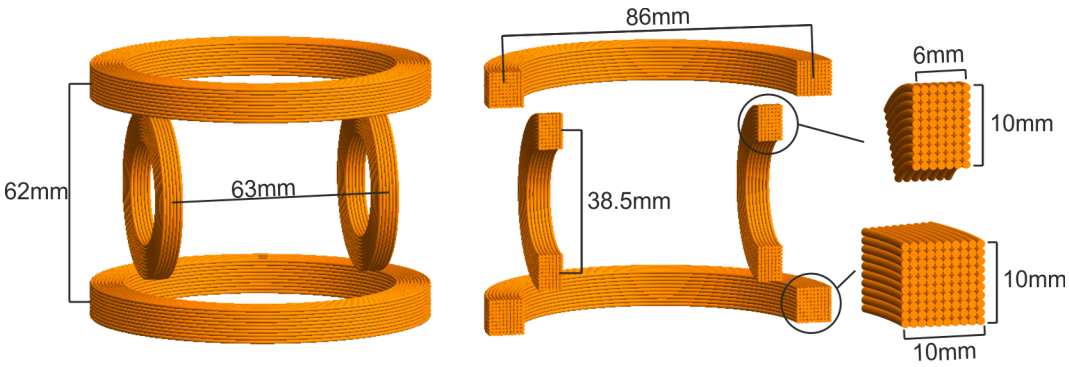

Figure 3.3: A sketch of the coils. The spools that hold the coils and the wires to power supply are not shown in this plot. This bigger coils have 100 turns each and the smaller coils have 60 turns. The drawings are to scale and the measures begin and end at the centres of the coil bundles.

Figure 3.4 shows the spool system that holds the coils. The system can be disassembled into individual spools for each coil so that I can wind copper wires on. Except for the slide holder, all components slot into each other and then are screw-secured for high strength. The slide holder, which will be fixed on the nanostage of the microscope, is detached from

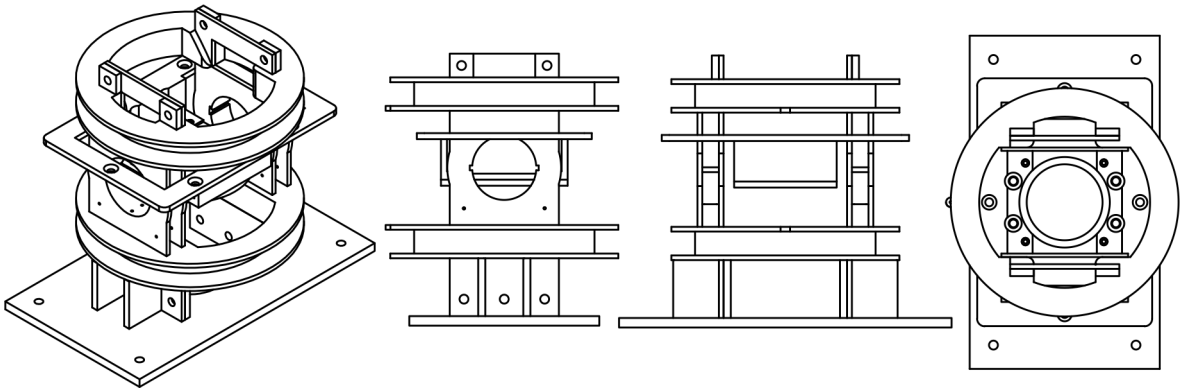

Figure 3.4: A sketch of the spools that hold the coils.

the rest of the spool holder (though it cannot be removed unless the top spool is removed first) to allow movement between the nanostage and the coils. Since the small spools take up space in the square hole in the nanostage, the slide holder has to be shorter than the standard size. Correspondingly, shorter slides (Microslide 27 X 46 X 1.0 mm cut edges, Gerhard Menzel GmbH) are used. The designing was done with Autodesk Inventor 2015 (Autodesk, Inc.); the 3D printing was carried out with Objet500 Connex3 (Stratasys, Ltd.); Rigur RGD450 (Stratasys, Ltd.) is the printing material. Table 3.2 lists some properties of Rigur RGD450. I have made an aluminium platform which mounts on the microscope so that the spool system can mount on it (see figure 3.5). The arrangement fixes the position of the coils relative to the objective. As mentioned before, the slide holder is fixed to the nanostage.Thus movement of the nanostage moves the flow cell relative to the coils - just the way it needs to be.

The coils are hand-wound from enamel wrapped copper wires (20 SWG, 500 g/m, Rapid Electronics, Ltd.) with a diameter of $0.914\,\mathrm{mm}$. It was tricky to wind the wires neatly manually so the wires are not packed tightly neighbouring adjacent wires. Occasionally a wire can 'jump lane' to the wrong side of the previous turn. The effect of the imperfect

Tensile strength	$40 - 45\,\mathrm{MPa}$
Elongation at break	$20 - 35\%$
Modulus of elasticity	$1700 - 2100\,\mathrm{MPa}$
Flexural strength	$52 - 59\,\mathrm{MPa}$
Flexural modulus	$1500 - 1700\,\mathrm{MPa}$
Heat deflection temperature @ 0.45 MPa	$49 - 54°\mathrm{C}$
Heat deflection temperature @ 1.82 MPa	$45 - 50°\mathrm{C}$
Izod notched impact	$30 - 35\,\mathrm{J\,m^{-1}}$
Polymerized density	$1.20 - 1.21\,\mathrm{g\,cm^{-3}}$

Table 3.2: Some properties of the 3D printing material Rigur RGD450, which is a simulated polypropylene.

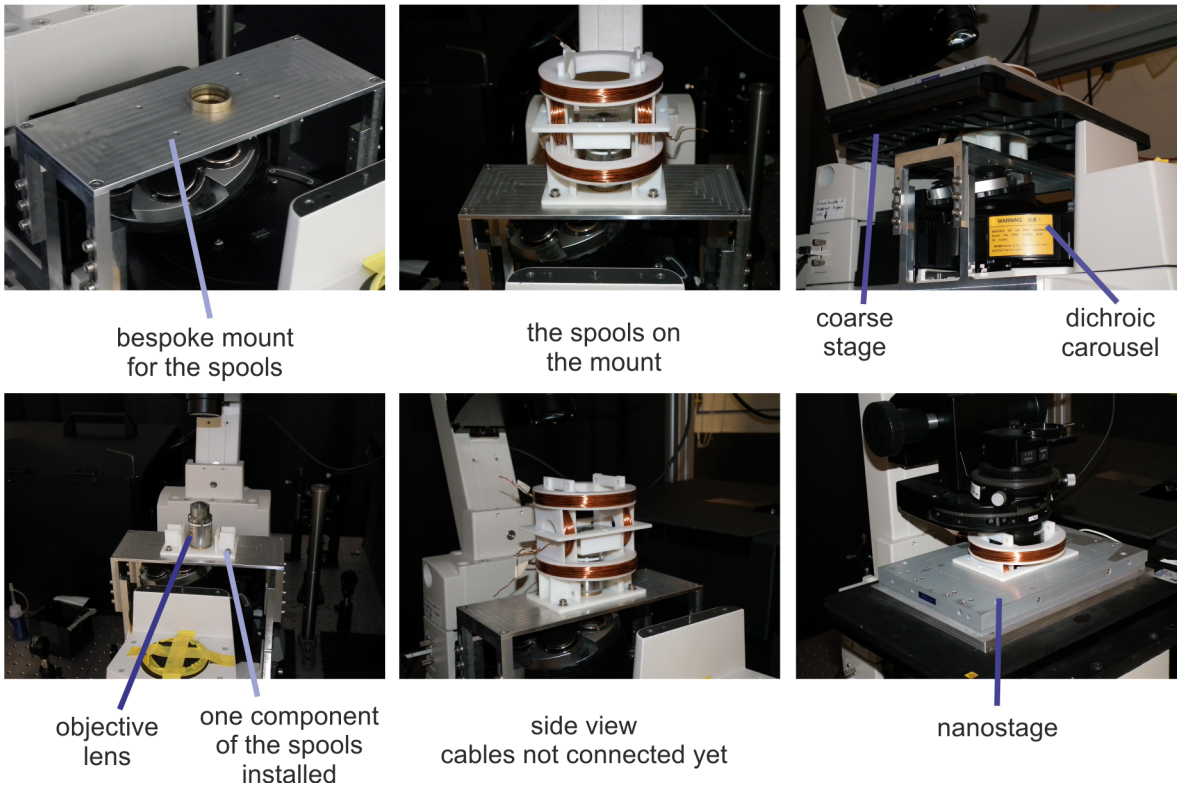

Figure 3.5: Some photos of magnetic tweezers.

winding on the **B** field is nonetheless negligible, which will be shown in section 3.3. After winding, the big coils are connected in series. The polarity is such that when a current is fed into the coil pair, the **B** field from the two coils are in the same direction so the resultant field is double the individual field. Then the coil pair is connected to the output of one of the amplifiers. The same arrangement is done to the small coils (powered by the other amplifier).

3.2.2 The driving circuit

The coils are driven by two PC-controllable bipolar 4-quadrant linear power supplies (BOP 20-5M, Kepco, Inc.). In our application, these power supplies function as high-powered operational amplifiers, which are typically controlled with a voltage signal ranging from -10V to +10V. The output mode can be set to voltage or current mode. Since the **B** field is proportional to the current, the amplifier is set to current mode. The control voltage is directly proportional to the output current, which ranges from -5A to +5A. Table 3.3 lists

selected characteristics of the amplifier provided by the vendor. Since the MT feed on a single low-frequency ($< 30\,\mathrm{hertz}$) sinusoidal wave at any time, the dynamic specifications (the first 4 lines in table 3.3) of the amplifier are more than above the required standard. The static properties of $< 0.01\%$ unwanted fluctuation in current will result in the same percentage of fluctuations in the **B** field, which is small compared to other sources of noise. I also characterised the power supply myself, the data of which are found in section 3.3. The

Rise & fall time ($10\% - 90\%$)	$< 30\,\mu\mathrm{s}$
Large signal frequency response	$> 13\,\mathrm{kHz}$
Slewing rate	$> 0.15\,\mathrm{A}\,\mu\mathrm{s}^{-1}$
Recovery step load	$< 10\,\mu\mathrm{s}$
8-hour drift	$< 0.01\%$
Ripple and noise (rms)	$< 0.01\%$
Ripple and noise (p-p)	$< 0.1\%$

Table 3.3: Selected characteristics of the BOP 20-5M amplifier provided by the vendor. All quoted values are those when the amplifier is in current mode.

voltage signal is generated with a LabVIEW controlled analogue output (NI 9263, National Instruments Corporations). Figure 3.6 (a) shows the schematics of the electronic part of the magnetic tweezers. I have used 13 ampere rated kettle leads for the connection between the amplifiers and the coils. The reason being both the high current they are designed carry (low resistance) and the twisted pair cabling to minimising cross-talk when an AC current is carried. The leads are kept at a minimum practical length (<1.5 m) to reduce any possible magnetic field from the cables.

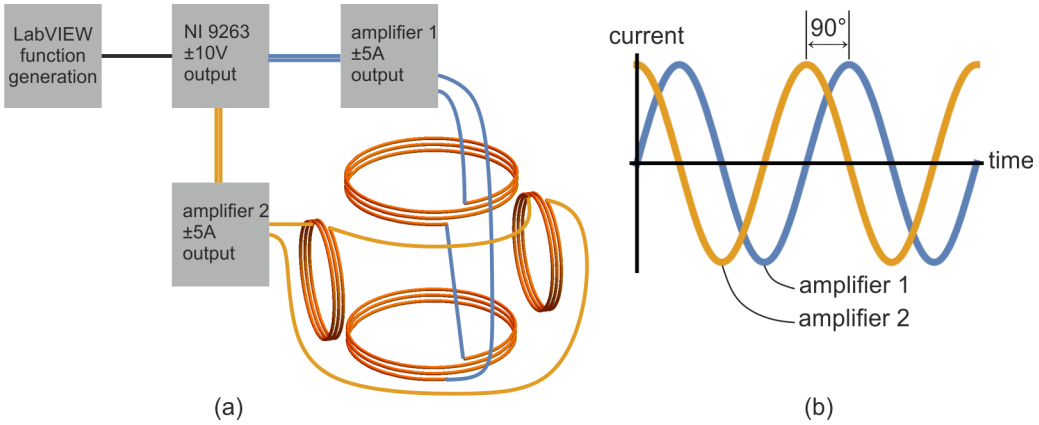

Figure 3.6: Schematics of the control circuit of the magnetic tweezers. (a) The experimenter uses LabVIEW to generate control sinusoidal voltages in two channels. NI 9263 outputs the voltages to two amplifiers that turn the voltages to currents. The amplifiers then drive the two pairs of coils. (b) An example of currents sent to the coils to rotate the **B** field at constant angular speed. Note that for simplicity, the amplitudes for the two waves are taken to be the same. In reality they will be different.

I illustrate the mechanism of the magnetic tweezers by describing the generation of a rotating **B** field. Two sinusoidal currents are sent to the two pairs of coils respectively. Figure 3.6 (b) shows the phase relationship between the two currents. At time = 0, the yellow curve is at its maximum, creating a maximum horizontal field. Since the blue curve is at zero, there is no vertical field component. As time goes on, the horizontal field decreases and a vertical

component starts to appear. The resultant field starts to point up. Following through the rest of the curves, you can see that the **B** field rotates at constant velocity for two circles. If a magnetic bead is in the centre of the coil set, it will also rotate two turns. The code to control the MT can be found in appendix A.2.

3.3 Instrument modelling

In this section I evaluate a few key parameters to the operation of the magnetic tweezers such as the **B** field strength and direction, torsional stiffness of the MT, heat dissipated and temperature rise of the system and so on. Simple geometries are done with evaluation of analytical expressions with reasonable values for variables such as **B** and I. Non-symmetrical geometries are done with numerical integration. These *a priori* values serve as rough guides as to where measured values should lie and the correctness of theoretical and experimental values can be crossed checked.

3.3.1 Magnetic field and torque

Equation 3.3 gives the **B** field of one turn of coil. Figure 3.3 shows the radius and positioning of the coils. So for the pair of bigger coils, assuming $I = 1\,\mathrm{A}$, the **B** field in the centre (where biological samples will be placed) is in the vertical direction and of magnitude:

$$B_{\uparrow} = 2 \times 100 \times \frac{\mu_0 I R^2}{2(R^2 + z^2)^{3/2}} \tag{3.15}$$

$$= 200 \times \frac{\mu_0 (43 \times 10^{-3})^2}{2((43 \times 10^{-3})^2 + (31 \times 10^{-3})^2)^{3/2}} \tag{3.16}$$

$$= 1.56\,\mathrm{mT} \tag{3.17}$$

where the factor of 2 is due to the two coils and 100 due to 100 turns in each coil. Similarly, the small pair of coils create a field pointing horizontally:

$$B_{\rightarrow} = 2 \times 60 \times \frac{\mu_0 (19.25 \times 10^{-3})^2}{2((19.25 \times 10^{-3})^2 + (31.5 \times 10^{-3})^2)^{3/2}} \tag{3.18}$$

$$= 0.56\,\mathrm{mT} \tag{3.19}$$

For each coil, the turns are at different positions and of different radii, but the above treatment gives reasonable approximation. The difference between the approximated and exact values are 0.01% for the big coil pair and 0.85% for the small coil pair, which, at our current rounding of 2 digits after the decimal point, does not affect the rounded values. For a constant velocity rotation of the **B** field, we require that $B_{\rightarrow} = B_{\uparrow}$. So the current in the small coils needs to be $1.56/0.56 = 2.8$ times the current in the big coils. Table 3.4 lists B at a few current values. $I_{\rightarrow}$ is the current in the small coils; $I_{\uparrow}$ is the current in the big coils. The last column is calculated with equation 3.9 with magnetisation calculated from equation 3.4, assuming $\alpha = 5\%$ (α is a constant of proportionality that quantifies the bead magnetic anisotropy - see equation 3.7 for its mathematical definition), which is a "typical" value for superparamagnetic beads [63]. But of course α needs to be obtained experimentally.

Helmholtz coils provide a highly uniform magnetic field in the volume between the two coils. However, the MT in my design are an approximation to Helmholtz coils since the

$I_{\uparrow}$ (A)	$B_{\uparrow}$ (mT)	$I_{\rightarrow}$ (A)	$B_{\rightarrow}$ (mT)	B_{sum} (mT)	k_{θ} (pN nm rad^{-1})
0.1	0.156	0.28	0.156	0.22	4.6
0.5	0.78	1.4	0.78	1.1	115
1.0	1.56	2.8	1.56	2.2	461
1.5	2.34	4.25	2.34	3.3	1035

Table 3.4: Some typical current values fed into big and small coil pairs, the generated field strengths and torsionally stiffness. The stiffness is calculated with an assumed $\alpha = 5\%$. Actual α will be measured experimentally.

separation between the two coils in each pair is larger than the radius of the coils. This is more so for the smaller pair of coils (see figure 3.3). So it is important to know the gradient of the field strength especially in the central horizontal plane as the flow cell will be moved in a 2 mm by 2 mm square in that plane during experiments. The flow cell is fixed in the vertical position from experiment to experiment so the variation along the z-axis can be ignored (the variation in z is quite small anyway). I evaluated the $\mathbf{B}$ field as a function of the 3D positions in the volume of the spools. The off-axis points are numerically integrated with equation 3.1. Figure 3.7 shows the $\mathbf{B}$ field strength for four example planes. Figure 3.7 (a) and (b) show the field strength in the vertical plane that passes through the centre of the spool (see the labelled viewing angle in the figures). Although the field varied almost from 0 to 100% in the planes, most of that variation is outside of the central cube of side length 10 mm. For example, when only the larger pair of coils are switched on, there is only 0.48% variation over the central 10 mm along the x-axis - see the plot in Figure 3.7 (a) on the very top. The variation in the central 2 mm is only 0.019% (not shown in the figure). (b) shows the corresponding plot when the smaller pair of coils are turned on. Variation over 10 mm along the same axis is 7.4% while over 2 mm is 0.30%. The variation along the y-axis are plotted in Figure 3.7 (c) and (d), on the very top of each sub-figure. The variation in Figure 3.7 (c) is identical to that in (a) due to cylindrical symmetry. The variation in Figure 3.7 (d) is much less than that in (b).

3.3.2 Heat generation

Another important element to consider is the heat generated and temperature rise of the tweezers as well as the flow cell. The radius of the copper wire is $0.457 \times 10^{-3}\,\mathrm{m}$, so the cross-sectional area is:

$$A_{coil} = \pi(0.457 \times 10^{-3})^2 = 6.56 \times 10^{-7}\,\mathrm{m}^2 \tag{3.20}$$

I use the radii of individual turns (as opposed to using the average) to calculate the lengths of the coils:

$$l_{big} = 2 \times 10 \times \sum_{radius} 2\pi \times radius = 54.0\,\mathrm{m} \tag{3.21}$$

$$l_{small} = 2 \times 6 \times \sum_{radius} 2\pi \times radius = 14.4\,\mathrm{m} \tag{3.22}$$

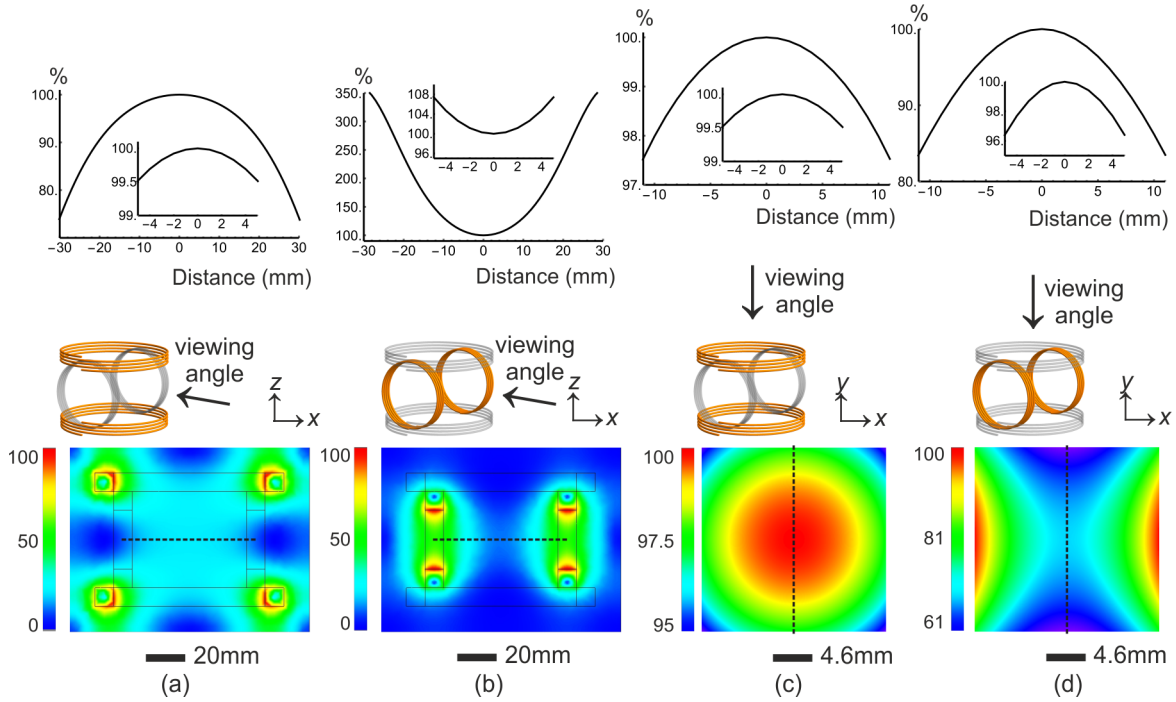

Figure 3.7: The distribution in space of the magnetic field due to the coils. (a) Top: profile plot of the field strength along the dashed line in the false colour strength at the bottom. The inset shows a zoomed-in figure of the central part of the plot. The centre in all x, y and z axes are the origin in the plots. The variation is 0.5% over 10 mm. Bottom: the field intensity over the xz plane. (b) shows the same plots as in (a) but with the smaller pair of coils turned on instead. (c) and (d) show the central horizontal rather than the vertical plane.

The resistivity of copper is $\rho = 1.68 \times 10^{-8}\,\Omega\,\mathrm{m}$, so the total resistance is

$$R_{big} = \rho \frac{l_{big}}{A_{coil}} = 1.38\,\Omega \tag{3.23}$$

$$R_{small} = \rho \frac{l_{small}}{A_{coil}} = 0.37\,\Omega \tag{3.24}$$

The power of heat dissipation, assuming sinusoidal current with an amplitude $I = 1\,\mathrm{A}$ into both the big coil pair and the small coil pair, is:

$$P_{big} = I_{rms}^2 R_{big} = \left(\frac{1}{\sqrt{2}}\right)^2 \times 1.38 = 0.69\,\mathrm{W} \tag{3.25}$$

$$P_{small} = I_{rms}^2 R_{small} = \left(\frac{1}{\sqrt{2}}\right)^2 \times 0.37 = 0.185\,\mathrm{W} \tag{3.26}$$

$$\tag{3.27}$$

The volume of the coils:

$$V_{big} = l_{big} A_{coil} = 54.0 \times 6.56 \times 10^{-7} = 3.54 \times 10^{-5}\,\mathrm{m}^3 \tag{3.28}$$

$$V_{small} = l_{small} A_{coil} = 14.4 \times 6.56 \times 10^{-7} = 0.94 \times 10^{-5}\,\mathrm{m}^3 \tag{3.29}$$

So mass

$$m_{big} = 8.96 \times 10^3 V_{big} = 0.317\,\mathrm{kg} \tag{3.30}$$

$$m_{small} = 8.96 \times 10^3 V_{small} = 0.084\,\mathrm{kg} \tag{3.31}$$

where $8.96 \times 10^3\,\mathrm{kg\,m^{-3}}$ is the mass density of copper. The heat capacity of the coil set is

$$C_{big} = 385 m_{big} = 122\,\mathrm{J\,°C^{-1}} \tag{3.32}$$

$$C_{small} = 385 m_{small} = 32\,\mathrm{J\,°C^{-1}} \tag{3.33}$$

where $385\,\mathrm{J\,kg^{-1}\,°C^{-1}}$ is the specific heat capacity of copper. For the calculation of the

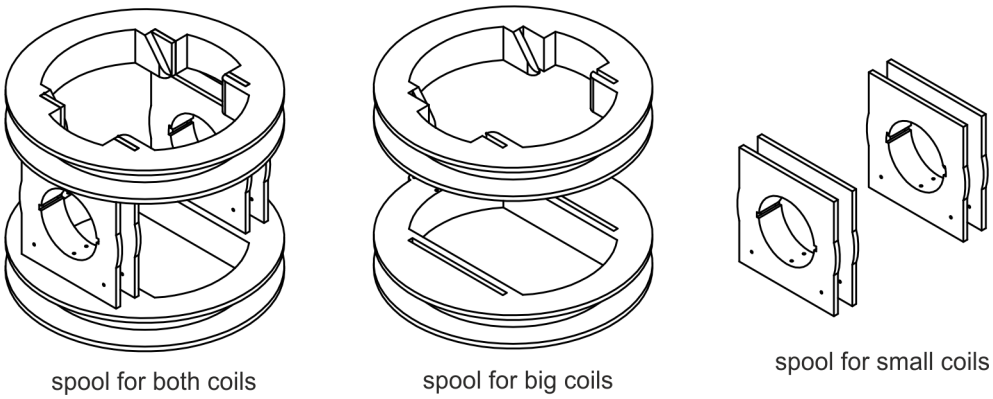

Figure 3.8: The portion of the spool set used in the calculation of the heat capacity. The rest is omitted as the rest is not in direct contact with the coils. See figure 3.4 for the complete spool set.

heat capacity of the spool, only the part in direct contact with the coils is used (see figure 3.8). The volume of the partial spool is $V'_{big} = 4.97 \times 10^{-5}\,\mathrm{m^3}$ and $V'_{small} = 1.42 \times 10^{-5}\,\mathrm{m^3}$. This is automatically evaluated by Autodesk Inventor. The mass is $m'_{big} = 0.060\,\mathrm{kg}$ and $m'_{small} = 0.017\,\mathrm{kg}$. It is not clear what the specific heat capacity of the 3D print material is so I will use that of polystyrene ($1500\,\mathrm{J\,kg^{-1}\,°C^{-1}}$) to calculate the heat capacity of the spool:

$$C'_{big} = 1500 m'_{big} = 89\,\mathrm{J\,°C^{-1}} \tag{3.34}$$

$$C'_{small} = 1500 m'_{small} = 26\,\mathrm{J\,°C^{-1}} \tag{3.35}$$

And the total heat capacity of the spool-coil system is:

$$C''_{big} = 122 + 89 = 211\,\mathrm{J\,°C^{-1}} \tag{3.36}$$

$$C''_{small} = 32 + 26 = 58\,\mathrm{J\,°C^{-1}} \tag{3.37}$$

With peak-to-peak $I_{big} = 1\,\mathrm{A}$ and $I_{small} = 2.8\,\mathrm{A}$, and ignoring the loss of heat into the surrounding for now, the temperature rise of the system as a function of time is:

$$\Delta T_{big} = \frac{P_{big}}{C''_{big}} t = \frac{0.69}{211} t = 3.27 \times 10^{-3} t \tag{3.38}$$

$$\Delta T_{small} = \frac{P_{small}}{C''_{small}} t = \frac{0.185}{58} t = 3.18 \times 10^{-3} t \tag{3.39}$$

Figure 3.9 shows a plot of temperature rise as a function of time:

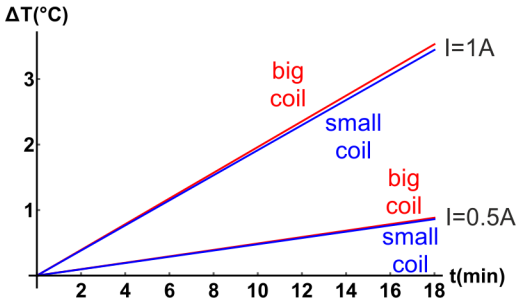

Figure 3.9: Temperature rise in the big and small coil pairs over time. Half-peak-to-peak $I = 1\,\mathrm{A}$ and $I = 0.5\,\mathrm{A}$ are supplied to both coils in this example. Heat loss into the surrounding is neglected for this plot. Note that the blue and red lines are quite close together for either current level.

The above calculation does not take into consideration the dissipation of heat into the environment, which will set a plateau to the temperature of the coils and also slow down the initial temperature rise. This effect will not be modelled here. Measured values can be found in section 3.5.4.

3.4 External magnetic field

Since the magnitude of the operating $\mathbf{B}$ field is "small", we need to consider the effect of background magnetic field on the rotation of the bead in the MT. The external field composes of the earth's magnetic field and the field from magnets in other instruments. I will try to evaluate them and the effect on the MT and devise approaches to reduce the effect of these fields.

3.4.1 Earth's magnetic field

Table 3.5 show the earth's magnetic field. As a comparison, the magnitude of the magnetic field due to the MT is on the order of $1\,\mathrm{mT}$. Figure 3.10 shows the orientation of the microscope. The angling of the lab relative to the geographical north is first found out from Google map to be $24°$. The microscope and the MT are aligned with the lab they are also $24°$ from the north. I project $\mathbf{B}_{earth}$ onto the MT's coordinate system where the x-axis is along $\mathbf{B}_{earth\rightarrow}$ created by the pair of smaller coils and the z-axis is along $\mathbf{B}_{earth\uparrow}$ created by the pair of larger coils to get:

$$\mathbf{B}_{earth\rightarrow} = 6.9\,\mu\mathrm{T} \tag{3.40}$$

$$\mathbf{B}_{earth\uparrow} = -45.9\,\mu\mathrm{T} \tag{3.41}$$

which are 0.69% and 4.6% that of $1\,\mathrm{mT}$ respectively. The resulted angular deflection of the bead for a $1\,\mathrm{mT}$ field are maximally $0.065\,\mathrm{rad}$ ($3.75\,°$). This is when the MT's field is purely horizontal and oriented such that $\mathbf{B}_{earth\rightarrow}$ cancels $6.9\,\mu\mathrm{T}$ of it. Then $\mathbf{B}_{earth\uparrow}$ tilts the combined field up by $\arctan(45.9/(707 - 6.9)) = 0.065\,\mathrm{rad}$. This tilt changes in both magnitude and direction as the MT's field rotates. The resulted k_θ can be maximally increased by 9.5% when the MT's field and the earth's field are aligned and the latter strengthens the former. When they are anti-aligned, k_θ decreases by 9.1%. All these are assuming that MT's field is $1\,\mathrm{mT}$. The earth's field has less effect when the MT's field

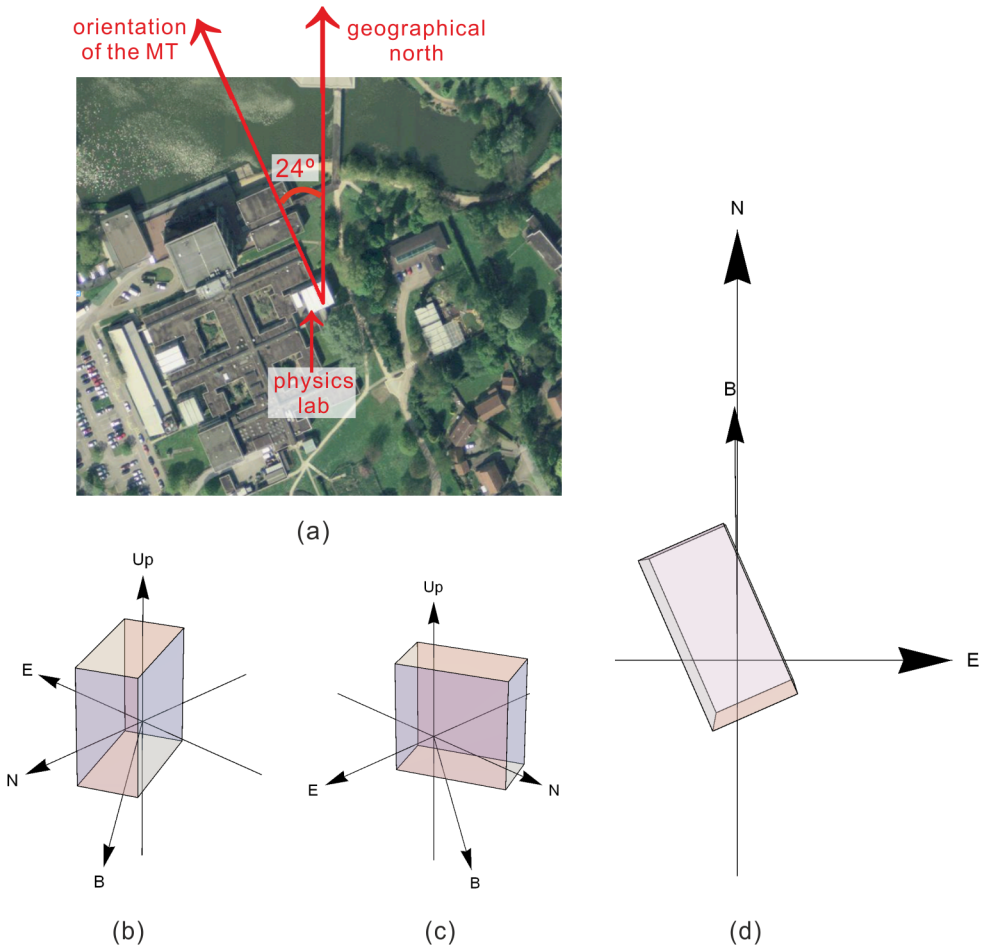

Figure 3.10: Earth's magnetic field. (a) A Google map screenshot showing the physics lab orientation. The MT are in the same direction as the microscope. (b) to (d) show the earth's magnetic field relative to the orientatin of the microscope. The coordinates are geographical rather than magnetic.

increases and vice versa.

Methods of isolating a volume from the earth's field can be divided into passive and active categories. The former involves shielding the region of interest with an enclosure of material of high permeability such as permalloy or mu-metal. It is not obvious how to enclose the sample space because the MT are mounted on the microscope which in turn is placed on the optical table and the whole setup is huge. The latter involves using 3 pairs of Helmholtz coils to generate negative field of the earth's field in each of the three spatial dimensions. The coils that make up the MT are good approximations of Helmholtz coils in the central region of several millimetres. There are only two pairs but the third pair is not necessary as that pair would cancels earth's field along the magnetic bead's rotational axis. The DC currents in the small and large pair of coils to cancel the earth's field are

$$I_{\rightarrow} = 8.8\,\mathrm{mA} \tag{3.42}$$

$$I_{\uparrow} = 21\,\mathrm{mA} \tag{3.43}$$

The above are *a priori* values, the direction and intensity of local earth's field are influenced by the presence of any material of high permeability in the neighbourhood such as reinforcement steel in concrete walls. So the discussion above serves more as an

	North (nT) (+N -S)	East (nT) (+E -W)	Vertical (nT) (+D -U)	Total (nT)
value	18209.0	-533.3	-45899.8	49382.6
change/year	10.7	49.0	21.1	23.4
uncertainty	138	89	165	152

Table 3.5: Values of earth's magnetic field at latitude of 53.945°N and longitude of 1.054°E, the coordinates of the lab and on 22 November 2014. World magnetic model (WMM) [132] is used to obtain the field values.

indication of how much earth's field will likely affect the tweezers' operation rather than providing actual values for correcting the earth's field. The *a posteriori* local earth's field will be discovered with the same method as described below to measure magnetic field due to other instruments.

3.4.2 Magnetic field of other instruments

Many lab equipments have permanent magnets in them such as PCs, cameras and motorised stages - indeed any equipment with motorised moving parts. It is difficult to calculate the resultant field due to all the magnetic field sources. Also, as mentioned in the section above, earth's field may have local variations. So I need to measure the field experimentally.

Hall probes or Gauss meters have low measurement precision. For example, the model 460 multi-axis Hall probe (Lake Shore Cryotronics, Inc.) has 0.25% measurement error and the most precise setting has a range of 0 to 3 mT, ie. the uncertainty is 7.5 $\mu\mathrm{T}$, larger than the earth's field (see equation 3.40).

I have devised a method to obtain the DC current required in each of the two pairs of coils to cancel the total local external field. For the smaller pair (responsible for $\mathbf{B}_{\rightarrow}$), a compass is placed horizontally in the center of the spools. With no current in the coils, the compass will point to the external field. A current is then supplied to the smaller pair of coils. The value is changed until the field along that axis is zero and the needle of the compass is perpendicular to that axis.

For the larger pair (responsible for $\mathbf{B}_{\uparrow}$), the compass is placed vertically in the center of the spools, in the plane formed by $\mathbf{B}_{\rightarrow}$ and $\mathbf{B}_{\uparrow}$. A current of arbitrary value is supplied to the smaller pair of coils so there is a $\mathbf{B}_{\rightarrow}$ component to bring the needle to point approximately in the transverse direction but there will be a vertical component in the orientation of the needle due to the external field. A current is then supplied to the larger pair of coils, the value of which is changed until the field along the vertical axis is zero and the needle of the compass lies completely transversely.

This method does not yield measured values of external field yet it does evaluate the DC currents to supply to the MT for cancellation of external field.

3.5 Calibration of the MT

In this section I discuss the measured values of key parameters that specify the properties of the magnetic tweezers. The signal-to-noise ratio in each of the equipments involved in driving the coils, the electrical properties of the coils, the magnetic field of the coils as a function of the currents and the background magnetic field. The most important calibration

is the stiffness of the field both as a function of the strength of the field and as a function of the angular speed.

3.5.1 Noise of the driving circuit

Any noise in the driving current will manifest as noise in the **B** field that rotates the magnetic bead so it needs to be quantified and considered during the analysis of rotation data. The noises in the driving circuit for the coils compose of contributions from the analogue output (NI 9263, ±10 V output) and the amplifiers (BOP 20-5M, ±5 A output in current mode). These are separately measured with analogue input (NI 9222), which happens to be the input that measures the QPD signals as described in chapter 2. The circuit used for measurement is sketched in figure 3.11 (a), which also contains the driving devices and the corresponding wiring - these have been paled-out so emphasis is led away from them. The results of the noise measurement are displayed in figure 3.11 (b) to (e).

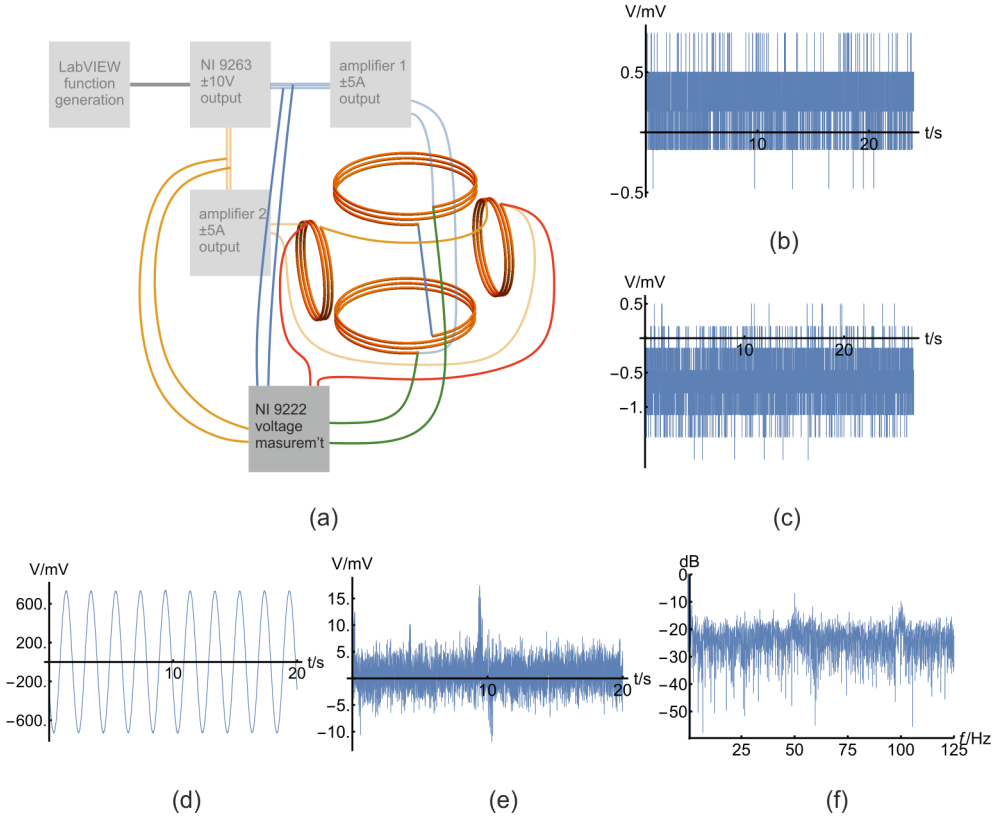

Figure 3.11: A sketch of the circuits to characterise instrument noises and the results of the measurement. (a) The controlling part of the driving circuit from figure 3.6 is included for reference but it is grayed out. The yellow and blue wire pairs measure the noises from the analogue output; the blue and green pairs measure the noises from the amplifier. (b) Noises in the measurement device itself. (c) Ripples in the analogue output. The driving current cannot be measured directly with existing equipments in my lab so the voltage across the coils is measured instead, which is shown in (d). (e) The noises in (d) obtained by subtracting a sine wave fit from the plot in (d). (f) Noise power spectrum of the plot in (e) to show that the noise is white. The absolute noise density is not shown; the decibel is used instead with 0 set at an arbitrary position.

First, the measurement noise of the analogue input (NI 9222) is evaluated by shorting the

terminals and taking readings. Since high-frequency (such as 50 kHz) noises will not be relevant - they simply average out over the rotational time scale of the bead - the sampling rate is set to be 250 Hz. The ripples over about 20 seconds are shown in (b). The standard deviation is 0.21 mV. I will regard this as the measurement error for other noises. Then the ripple in the analogue voltage output (NI 9263) is evaluated by connecting NI 9263 directly to NI 9222 and setting a DC 0 V output. The results are shown in (c). The standard deviation is 0.34 mV so the ripple is 0.34±0.21 mV. In addition, there is a DC offset of 0.62 mV from zero (the polarity of the signal has been ignored).

Next, the amplifier that drives the larger coil pair is turned on. The analogue output sends a 0.5 Hz, 1 V control signal to the amplifier. The amplifier's output current varies linearly with the control voltage $I_{out} = \sigma V_{ctrl}$ where $\sigma = 0.5\,\mathrm{A\,V^{-1}}$. Therefore the 1 V control signal results in the amplifier output of 0.5 A. Equation 3.24 gives the calculated resistance of the coil pair - $1.38\,\Omega$ - so from Ohm's law the amplitude of the voltage across the coil pair should be 0.69 V. Figure 3.11 (d) shows the measured voltage across the coil pair, the wiring of which is shown as the green pair of wires in (a). The data are fit with a sine wave to yield an amplitude of 0.72 V, which agrees quite well with the theoretical value, considering that the wiring for voltage measurement takes up a portion of the voltage drop as well. Data in (d) are then subtracted by the sinusoidal fit to obtain the noise in the data. The noise is plotted in (e), which has a standard deviation of 2.63 mV. The root-mean-square value of the driving signal is $0.69/\sqrt{2} = 0.49\,\mathrm{V}$. So the ripple-to-signal ratio is $2.63/490 = 0.5\%$, which is worse than the specification shown in table 3.3. Also, there is a mean of 0.76 mV, which will show up as a constant $\mathbf{B}$. Equation 3.42 suggests that an approximately 8.8 mA DC current will be needed to cancel the earth's magnetic field. The error is about 10% the current to counter the earth's field, which emphasizes the need to experimentally obtain the current setting to offset the unwanted external field. Figure (f) shows the noise power spectrum. On the AC part of the noise, a Fourier analysis shows that the noise is white therefore the power of the noise in the rotation frequency will likely be small and can be neglected. The noise in other frequencies will average to the mean and therefore will not affect the bead's rotation once this mean is properly zeroed.

3.5.2 Current response to the driving circuit

An example of the measured voltage across the large pair of coils is shown in figure 3.11 (d) but what about other voltage levels? In this section, systematic measurement of the current through both pairs of coils is shown. The method to obtain the current in the coils at any given driving voltage is the same as that used to obtain figure 3.11 (d), ie. using the measurement circuit in 3.11 (a).

NI 9222 in figure 3.11 (a) is a voltage sensor so the voltage across the coils instead of the current through the coils is measured although ideally I should measure the current as it is directly proportional to the generated magnetic field. The problem with measuring voltage is that the wires that connect NI 9222 to the coils has a small voltage drop on them so the calculated current for the coils will be smaller than the actual value. Nevertheless, the wires are kept as short as practically possible (∼1.5 m). The control voltage V_{ctrl} is set to sinusoidal oscillations with discretely increasing amplitudes so that the current in the coils also increases. This is shown in figure 3.12 (a). To obtain the amplitude of the waves, a sinusoidal expression is fit to each amplitude level. Figure 3.12 (b) shows an example of the

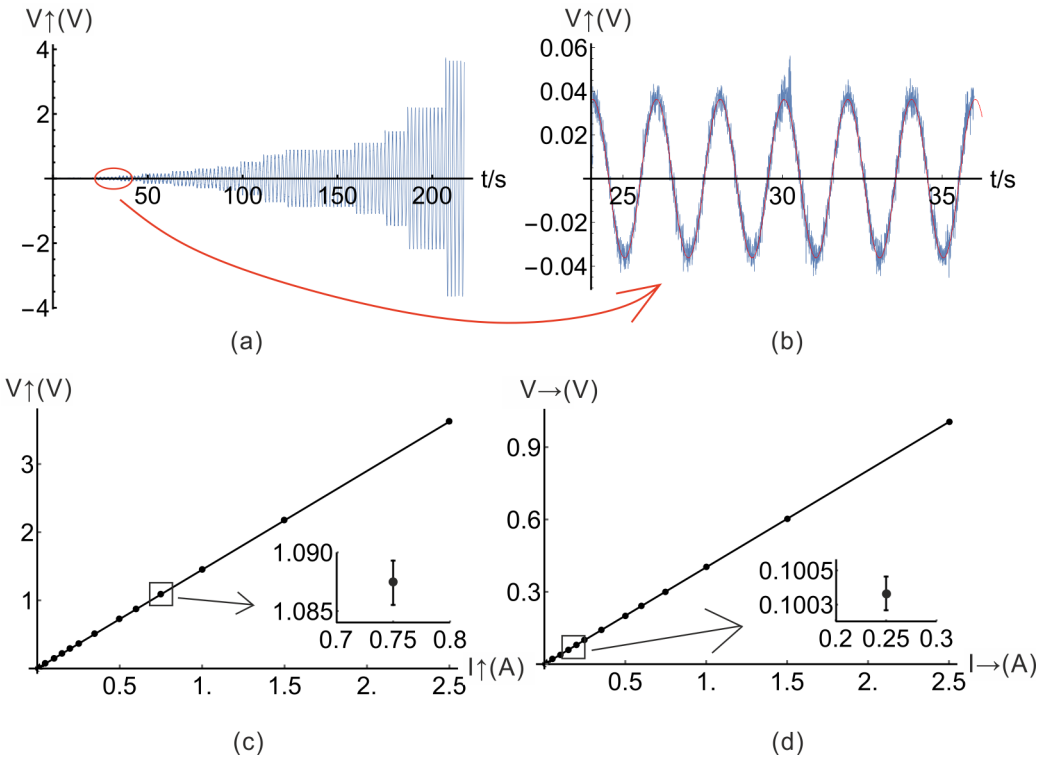

Figure 3.12: Coils' magnetic field. (a) The **B** field strength of the pair of larger coils as a function of current through the coils. The Gauss meter reading fluctuates over a time scale of $\sim 1\,\mathrm{s}$ and three readings are taken for each current level before moving on to taking the next reading. The error bars show the range of field strengths measured for that current. All error bars are too small to be visible so the inset shows a zoom-in on one of the points to show the magnitude of that error bar. (b) The **B** field strength of the pair of smaller coils.

fit as the red overlay on the data extracted from (a). The current from the amplifiers follows $I_{out} = \sigma V_{ctrl}$ where $\sigma = 0.5\,\mathrm{A\,V^{-1}}$. The voltages across the coil pairs are then plotted against the currents through them, shown in (c) and (d) for the larger and smaller pairs respectively. The error bars are obtained by splitting each measurement into two equal parts and fitting the sine wave separately to obtain two fits. Then the standard deviation is used as the error bars. Since they are too small to be visible, a zoomed-in version of a randomly selected point is shown in each plot. From the plots I can calculate the resistance of the coils plus the wires that connect the coils and NI 9222:

$$R_{big} = 1.44 \pm 0.0006\,\Omega \tag{3.44}$$

$$R_{small} = 0.40 \pm 0.00015\,\Omega \tag{3.45}$$

The errors are standard errors of the least square fit according to the following expression

$$\sqrt{\frac{(y - y\prime)^2}{N}} \tag{3.46}$$

where y is the measured voltage, $y\prime$ is the voltage from the fit line and N is the number of data points. The measured resistance is larger than the calculated value, partly due to the extra wiring and possibly also because the actual value is indeed larger. I do not need to know the exact value as it is the **B** that has to be know exactly, which will be discussed

below.

3.5.3 Magnetic field of the coils

The magnetic field of the coils as a function of the currents is measured with a Gauss meter (GM05, Hirst Magnetic Instruments Ltd), which composes of a transverse and an axial probe. But using one probe is enough to measure fields in 3D as it can be physically rotated to measure the field along different directions. The Gauss meter has a calibration shield to create a zero-field volume for the sensor to be zeroed inside. I tested it by holding the probe close to an electromagnet, which resulted in a reading of a few mT. Keeping the probe in place, I then put on the shield and followed the procedures displayed on the screen of the device to zero the probe with the shield. The probe was then mounted with

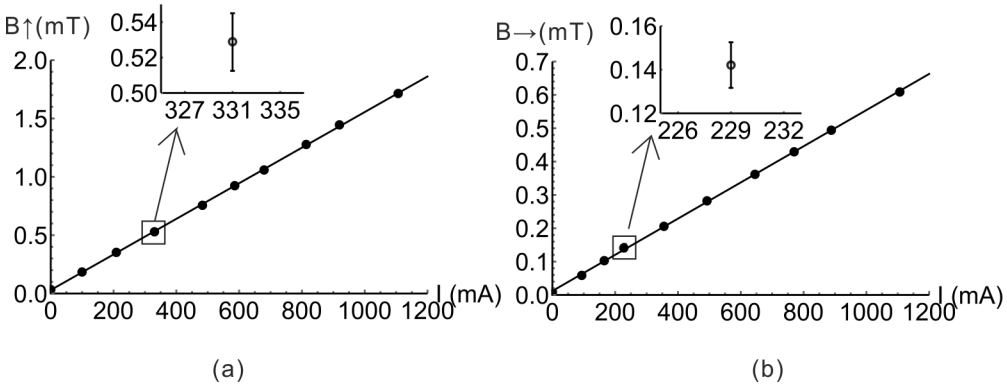

Figure 3.13: Coils' magnetic field. (a) The **B** field strength of the pair of larger coils as a function of current through the coils. The Gauss meter reading fluctuates over a time scale of $\sim 1\,\mathrm{s}$ and three readings are taken for each current level before moving on to taking the next reading. The error bars show the range of field strengths measured for that current. All error bars are too small to be visible so the inset shows a zoom-in on one of the points to show the magnitude of that error bar. (b) The **B** field strength of the pair of smaller coils.

Thorlabs optomechanical components so the probe head was in the centre of the coils. Figure 3.13 shows the result of measurements with linear fit to the data points. The two pairs of coils were turned on one-at-a-time for the measurement. There is quite good agreement between the measured and the calculated values in section 3.3.1. Note that the error bars are small so zoomed-in versions of a randomly selected point in each plot is included as insets. The error bars are approximately 0.03 mT in both insets. Table 3.5 lists earth's field ranging from 0.0005 mT to 0.046 mT in different directions, which is too small for the Gauss meter to measure.

As discussed in section 3.5.2, the exact currents in the coils are not known. The currents in figure 3.13 are calculated from $I_{out} = \sigma V_{ctrl}$ where $\sigma = 0.5\,\mathrm{A\,V^{-1}}$. It is V_{ctrl} that can be set exactly so as long as I know the relationship between **B** and V_{ctrl}, knowing the exact I is not important.

3.5.4 Temperature behaviour

The temperature rise of the coils after turning on the power supplies is measured with a thermocouple thermometer (Tenma 72-7712). The ends of the thermocouple are inserted into

the coil turns for the temperature measurement - see figure 3.14 (a). When a 1 A sinusoidal current is supplied to both coils, the initial temperature rise is approximately linear with time and the rate of increase matches the theoretical prediction in figure 3.9. This is shown in figure 3.14 (b). The temperature after around 15 minutes starts to plateau, as seen in the flattening in the curves in (b). I also measured the temperature rise in the big coil over about an hour, in which the temperature stabilises to about 0.8°C - see figure 3.14 (c).

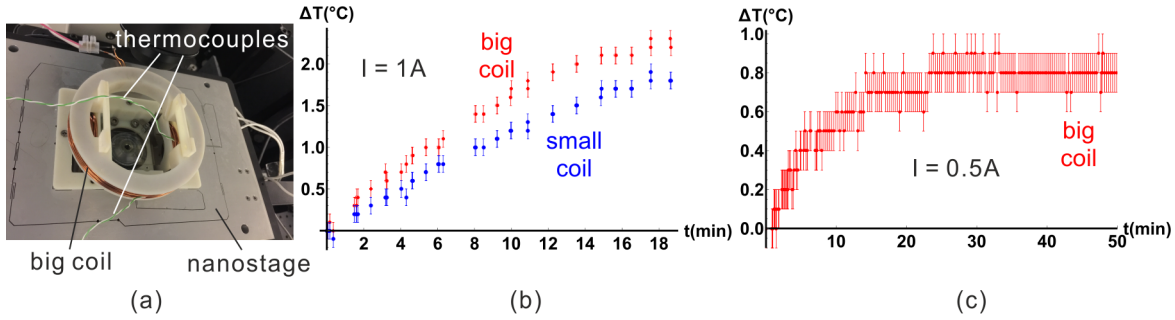

Figure 3.14: Initial temperature rise and subsequent plateauing. (a) A photograph featuring the thermocouple ends being inserted into the coil turns to measure the temperature of the coils. (b) The measured temperature for the big and small coils in the first 20 minutes after turning on the power supplies to send a sinusoidal current of 1 A in both pair of coils. (c) The measured temperature for the big coils in the first 50 minutes after turning on the power supplies to send a sinusoidal current of 0.5 A. The plateauing is seen after 20 minutes. The error bars are the precision of measurement by the thermometer.

3.5.5 Rotation control and measurement

The mechanism to rotate the magnetic bead at constant angular speed has been illustrated in section 3.2.2. The currents sent in the two pairs of coils are sinusoidal waves 90° apart, shown in figure 3.6 (b), and the amplitude of the current in the smaller pair of coils will be 2.8 times that in the larger pair, shown in table 3.4. There will also be a DC current of small values to offset the external fields - see equations 3.42 and 3.43.

If the ratio of the currents in the two pairs of coils deviates from the correct value, the rotation will accelerate and decelerate every half a cycle. The optimal ratio is found experimentally by exploring a range of values in the vicinity of 2.8 and measuring if the rotation speed is constant. First, the coil set is unmounted from the microscope and laid on its back so that the rotating $\mathbf{B}$ field is now in the horizontal plane. A compass is placed in the centre of the coil set to allow the visualisation of the $\mathbf{B}$ field. The response of the compass is video recorded with an iphone 6 plus rear camera at 60 frames per second. The rotation is set to 1 Hz (ie. 1 rev per second). This means every frame is an accummulation of up to 6° of rotation. Figure 3.15 shows the smearing of the compass needle of about 6° in a frame. Nevertheless, the frame images allow the determination of the orientation of the needle by finding the centre of the smear. The ratio of currents is adjusted until the orientation of the needle is equally apart from frame to frame. The ratio turns out to be about 2.8 so it matches the calculated value.

The beads are then rotated and images taken both in bright field and fluorescence. The lack of surface smoothness of the magnetic beads allows the observation of the rotation in

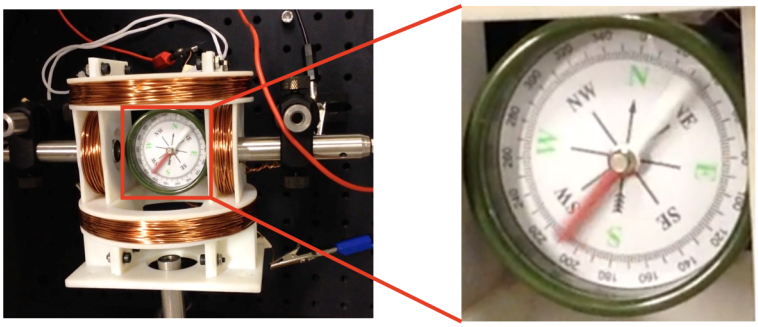

Figure 3.15: The ratio between the current in the large coils and the small coils is tested with a compass, which is laid flat in the centre of the coil set so that it can rotate freely. This dictates that the coils are flipped 90° from the mounted orientation. The frame rate of the camera is 16.67 ms so each frame will show the accumulation of the compass needle position over that time. The blow-up shows the smearing of the needle.

bright field. However, the autofluorescence from the beads are rather circularly symmetric so one cannot see the rotation of the bead in fluorescence. The approach to visualise the rotation in fluorescence is to clad the magnetic beads with biotin surface-functionalised fluorescent beads (FluoSpheres®, 505/515 nm, 0.04 µm, F8766). The two beads are diluted

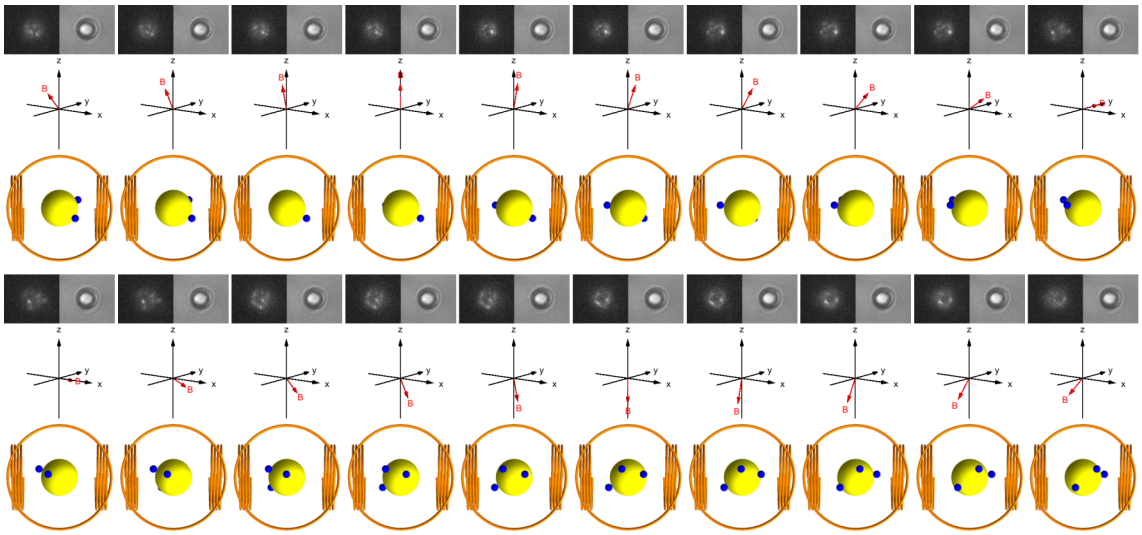

Figure 3.16: Selected frames from a video taken of a trapped and rotated magnetic-fluorescent bead combination in both bright field and fluorescence. Underneath each frame is a sketch of the orientation of the **B** field. Underneath that is a cartoon of the bead combination in which the magnetic bead is labelled yellow and fluorescent beads blue. The cartoon is to illustrate the rotation of the bead combination and the blue beads do not corresponds exactly to the positions of the fluorescent beads.

and mixed in 1 times PBS (phosphate-buffered saline) buffer with concentration of 1 in 100 from stock concentration for the magnetic beads and 1 in 1000 for the fluorescence beads. The beads are incubated for at least 10 minutes before being flown into a simple tunnel slide made by sandwiching a slide, two strips of double-sided tapes and a coverslip. The coverslips are plasma cleaned but not blocked with BSA (bovine serum albumin) although one can block the surface if they want to. A bead combination is first trapped with the optical tweezers so it does not diffuse away. Then currents are sent to the coils to rotate the

beads. Figure 3.16 shows snapshots of the video. Annotations of the bead orientation is added underneath the frame images. Videos of freely diffusing bead combination have also been taken in which the bead also diffuses in and out of focus.

The interference pattern between the bead and the NIR laser beam at the back focal plane of the condenser is concurrently collected by the QPD. It turned out that the ribbon cables usually used for carrying the multi-channel signals out of the QPD are induced an electromotive force (emf) from the varying $\mathbf{B}$ field. Figure 3.17 (a) shows a photo of a ribbon cable. I flew water into the tunnel slide and turned on both the OT and the MT, the latter running at 8 Hz. Figure 3.17 (c) shows a plot of the signal measured on the QPD. Since there are no magnetic beads in the laser trap or anywhere in the flow cell, the oscillation in V_{SUM} must be an induced emf. (d) shows its power spectrum as a function of frequency. When a

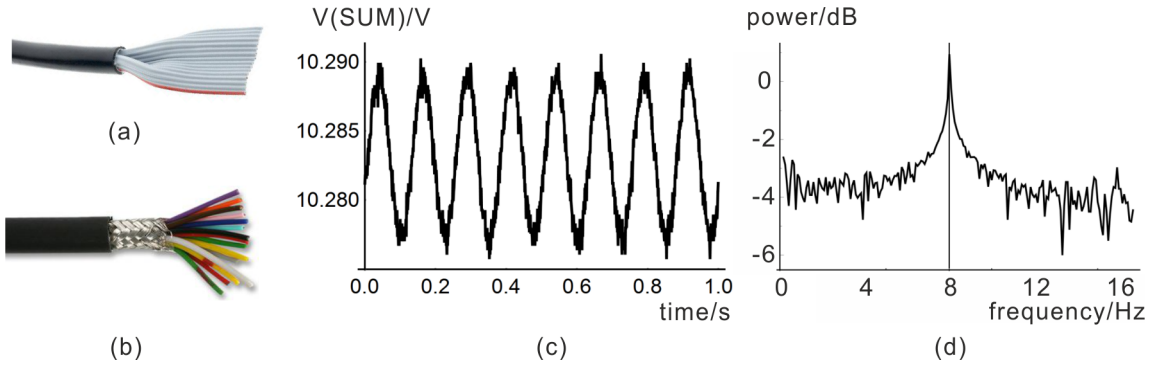

Figure 3.17: QPD cables need to be metallically sheathed to prevent the induction of an emf along the length of the cables. (a) A non-metallic sheathed cable. (b) A metallic sheathed cable. (c) Using a non-metallic sheathed cable, the varying $\mathbf{B}$ field induces an emf in V_{SUM} with an amplitude of about 0.1% the laser-originated signal. (d) The power spectrum of the signal clearly shows a peak at the rotation frequency (8 Hz).

metallic sheathed cable, a photo of which shown in figure 3.17 (b), is used, the induced emf is negligible and the power spectrum shows white noise (not plotted in the figure) so now the QPD and its cables are ready for the magnetic bead rotational measurement.

If there is only one fluorescent bead attached to the magnetic bead, ideally V_{LR}/V_{SUM} will show up as a sinusoidal wave but in reality the signal deviates from that of a sine, possibly because of the intrinsic surface asymmetry of the magnetic beads. If there are multiple fluorescent beads attached to the same magnetic bead, the waveform will presumably be a super-position of the sine wave with the rotation frequency (ie. the fundamental wave) and multiple higher-harmonic sinusoidal waves of various amplitudes and phases. The highest harmonic number is equal to the number of fiducial markers on the bead.

The voltage-time series has been discrete-Fourier transformed and absolute-squared to obtain the power spectrum plots - see figure 3.18 right panel. These plots clearly show the peaks corresponding to the fundamental frequency and the overtones, indicating the presense of multiple fluorescent beads on the magnetic bead surface. For the 1 Hz rotation, the fundamental peak is about ten times as high as the overtones. However, other frequencies see different ratios. For example, the 5 Hz plot sees almost equal fundamental wavelength and overtones.

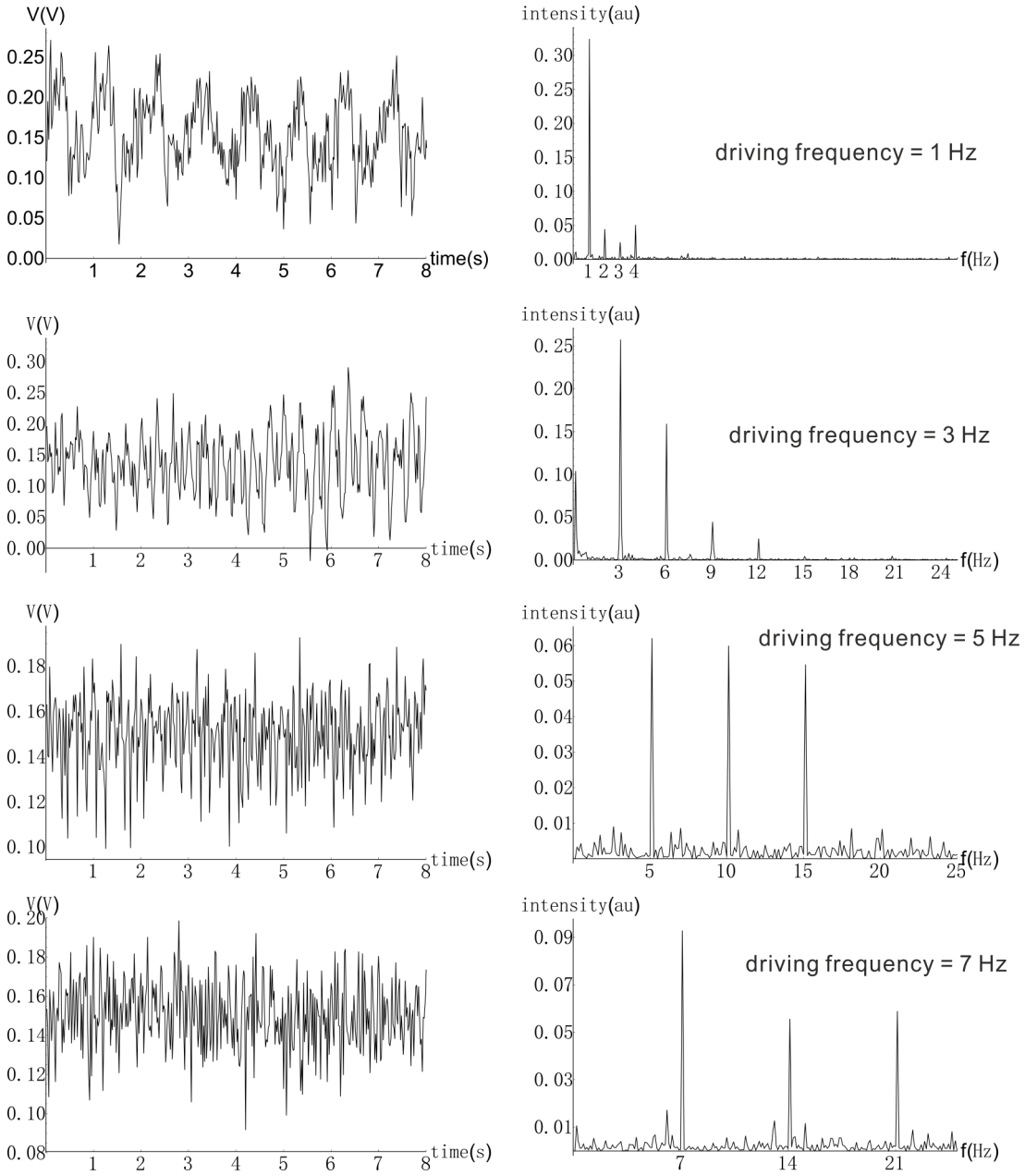

Figure 3.18: Four examples of V_{LR}/V_{SUM}-time plot (left) and their corresponding power-spectrum plot (right). The driving frequencies are 1, 3, 5 and 7 Hz respectively from top to bottom. In each V_{LR}/V_{SUM}-time plot the periodical oscillations in voltage is clearly seen although they do not follow a sinusoidal shape, due to the existence of the overtones as well as noise in the measurement. The vertical axis label should technically be a unitless ratio but here I (misleadingly) labelled it V(V) for simplicity. Also, the DC component has been removed (by subtracting mean) before the generation of the power spectrum plot because the DC peak dwarves the harmonics but it is the harmonics that are of interest. All x-axes of the spectrum plots have a range of 0 to 25 Hz so the four plots can be easily compared.

3.5.6 Angular stiffness

Two methods to calibrate the angular stiffness of the magnetic field have been described in section 1.4: the angular retardation method and the equipartition theorem method. For either of the methods to work, marker beads are needed again to decorate the surface of the

magnetic beads as described in section 3.5.5 although the 0.04 µm fluorescent beads serve different purposes in the two methods: a source of topological asymmetry for the QPD detection in the former and a visual marker for the camera detection in the latter. In this chapter I describe the use of the angular retardation method to obtain k_θ.

A 0.54 A sinusoidal current is sent to the larger pair of coils and 1.5 A to the smaller coils. The angular speed is set to $\omega_i = 2\pi,\ 4\pi,\ ...,\ 2\pi i\,\mathrm{rad\,s^{-1}}$ in succession, ie. the revolution per second is $f_i = 1,\ 2,\ ...,\ i\,\mathrm{Hz}$. For each frequency, the sine wave is set to run multiple cycles (on the order of 10) - see figure 3.19 (a) for a short sample of the control voltage running at 1 Hz. The measured QPD signal is not necessarily sinusoidal due to the presence of multiple marker beads (as opposed to one single bead) on the surface of the magnetic bead - see figures (b) and (c), which is described in detail in the figure caption. Since the QPD signals are rather noisy, it is tricky to find the phase of the signals. To solve this problem, I performed correlation of the signal with the reverse of itself. The resulted curve preserves the phase information while being much smoother - see figure (d). This way the peaks can be used to easily determine the phase of the correlation and thus the phase of the signals.

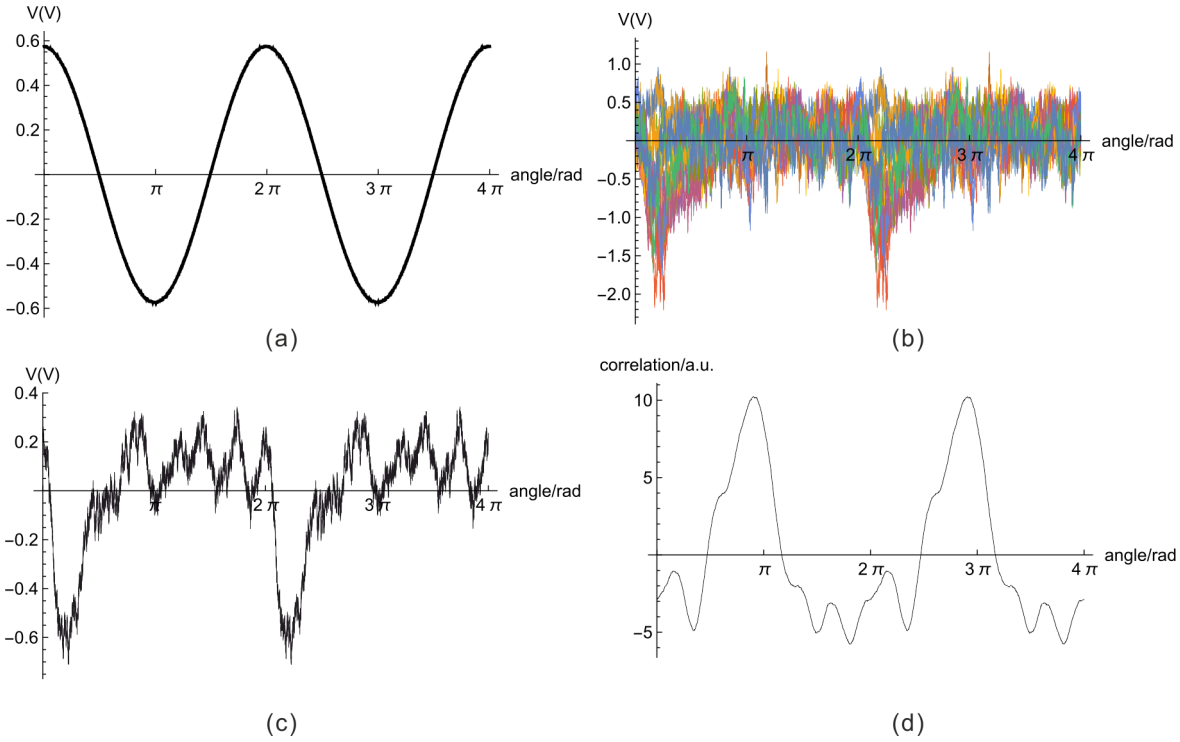

Figure 3.19: Finding the angular position of the marked magnetic beads by QPD measurement. (a) The control voltage applied to the smaller pair of coils for $f = 1\,\mathrm{Hz}$ rotations. Only 2 cycles are shown here for neatness of presentation. (b) The V_{LR}/V_{SUM} channel of the QPD signals. The V_{TB}/V_{SUM} channel also shows a periodic variation but it has lower amplitudes so I ignore that channel for the measurement of bead rotations. This time, however, all recorded signals for $f = 1\,\mathrm{Hz}$ rotations are sketched. They are first divided into 4π-long parts and plotted on top of each other, each of which is in a different colour - again the chopping-up of the signals is for presentation purposes. (c) The mean of all the plots in (b) shows clear periodicity but it is a noisy curve so simple methods such as using the peak to determine the phase do not apply. (d) The correlation of the plot in (c) with the reverse of itself. The peak in each period is quite easy to find and it is used as a marker to compare phases of the plots from different rotational frequencies.

Figure 3.20 plots QPD signals and correlations of all frequencies together and the phase of each correlation plot is circled. Figure 3.20 plots the phase shift as a function of rotation frequencies. Then the data are fit with a linear curve with gradient = $-0.429\,\mathrm{rad\,Hz^{-1}}$. From equation 1.44, the gradient is expressed as

$$\text{gradient} = \frac{8\pi\eta R^3}{k_\theta} \tag{3.47}$$

which rearranges to give

$$k_\theta = \frac{8\pi\eta R^3}{\text{gradient}} \tag{3.48}$$

The negative sign in the gradient indicates the fact that the bead lags behind the $\mathbf{B}$ field so can be ignored in the calculation of the stiffness. The resulting stiffness is $k_\theta = 1.1 \times 10^3\,\mathrm{pN\,nm\,rad^{-1}}$, which is at the lower bound of the $10^3 - 10^4\,\mathrm{pN\,nm\,rad^{-1}}$ of traditional magnetic tweezers. To achieve torque measurement of DNA in which the characteristic torques are on the order of $10\,\mathrm{pN\,nm}$, the stiffness of the trap needs to be on the order of $100\,\mathrm{pN\,nm\,rad^{-1}}$. This can be achieved by lowering the current $\sqrt{10}$ fold to 0.17 A in the larger pair of coils and 0.47 A to the smaller coils - remember that stiffness scales with the square of the currents in the coils.

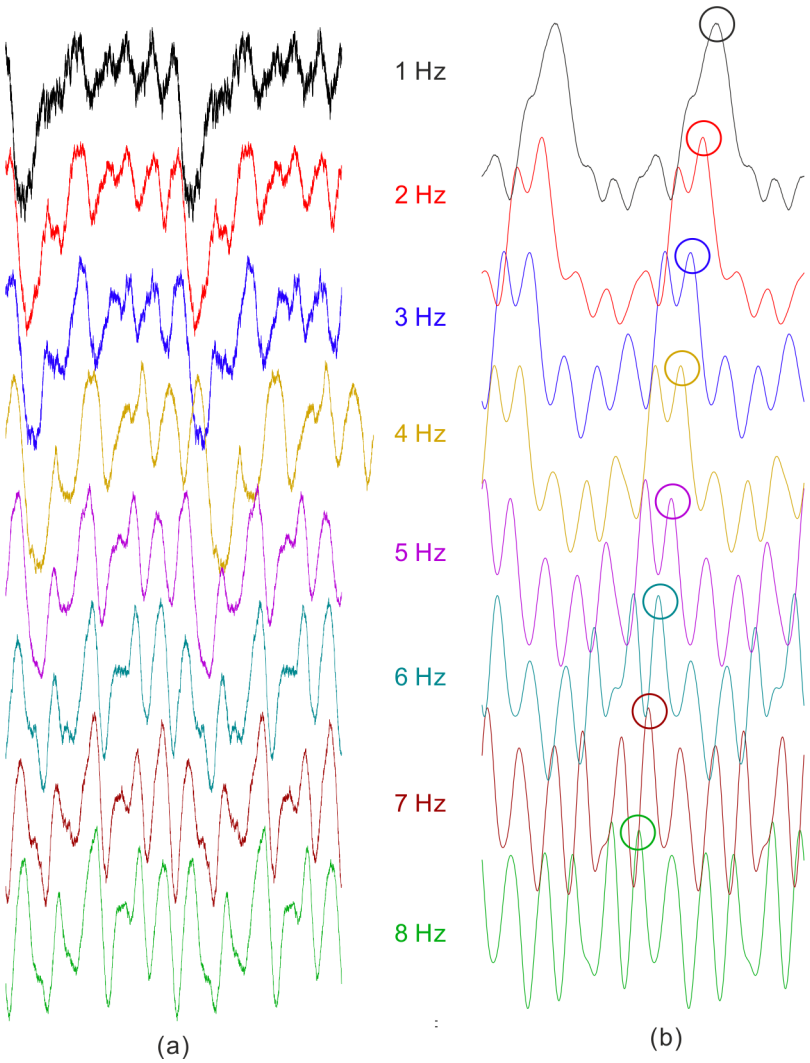

Figure 3.20: Finding the angular stiffness by the retardation method. (a) The averaged V_{LR}/V_{SUM} of the QPD signals for 1 to 8 Hz rotations are juxtaposed for easy observation of the phase shift over increasing rotation speeds. Axes have been removed so the plots are more easily compared. See figure 3.19 (c) for axes and other details. (b) The corresponding correlation plots - see figure 3.19 (d) for axes and other details. I use the circled peaks in each plot to determine the phase of the plots.

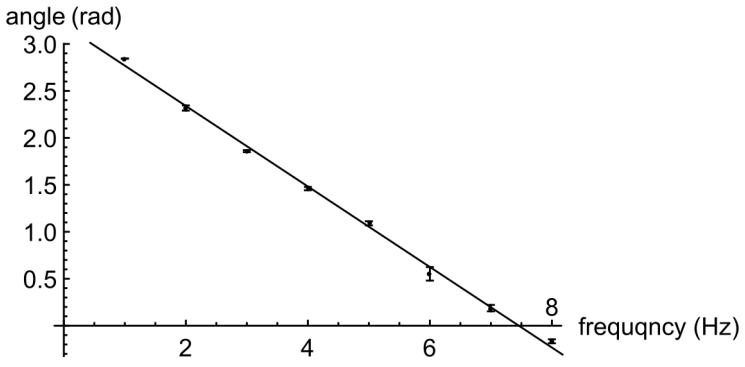

Figure 3.21: The phase shifts as a function of rotation frequencies. The phase shifts are obtained from the positions of the circles in figure 3.20 (b). The gradient of the linear fit is then used to obtain k_θ.

Chapter 4

Imaging Module

The instrumentation for super-resolution fluorescence microscopy includes excitation optics, the microscope and the emission optics. My fellow PhD student Helen Miller and I designed and built the system. We also devised assays for super-resolution fluorescence imaging of end-modified lambda-DNA molecules tagged with the intercalating dye molecule YOYO-1 and minor groove binding dye SYTO-13. Both dyes have photoblinking properties to allow the application of Stochastic Optical Reconstruction Microscopy (STORM) and analysis with software packages such as rainSTORM, QuickPALM and ADEMS code. We were able to observe DNA topological changes in real time, which is necessary when the DNA is manipulated with magneto-optical tweezers and its dynamics are imaged at single-fluorophore resolution.

This chapter describes the design and construction of the imaging module and the findings of the imaging experiments.

4.1 Excitation optics

A broad spectrum laser serves as the excitation light source of which the excitation wavelengths of the fluorophore are selected. Figure 4.1 shows the set-up where the laser passes through a telescope formed with a positive lens and the objective. The emerging beam is collimated and its diameter can be controlled by the focal length of the positive lens. I use both narrowfield [133, 134] and widefield mode epifluoresence to demonstrate in proof-of-principal experiments the trapping and imaging of DNA molecules. Slimfield mode has a small illuminated area of $\sim 30\,\mu\mathrm{m}$ and has 100 to 1000 times the intensity of a widefield illumination. This is both for increased emission rate and thus higher frame rate and also for restricted illumination only to the area of interest. For example, in the imaging of a DNA shorter than $3\,\mu\mathrm{m}$ in contour length, the excitation field will only need to be large enough to cover the length of the DNA. However, the excitation field can potentially be switched to standard diameter (widefield) as well as TIRF mode [135] for imaging other systems.

4.1.1 Excitation path properties

The laser used for excitation source is a white-light supercontinuum laser (Fianium SC-400-4, Fianium Ltd.). The full width at half maximum (FWHM) is measured to be $24\,\mu\mathrm{m}$ in widefield and $3\,\mu\mathrm{m}$ in slimfield. The unattenuated intensity 1800 is $\mathrm{W\,cm^{-2}}$.

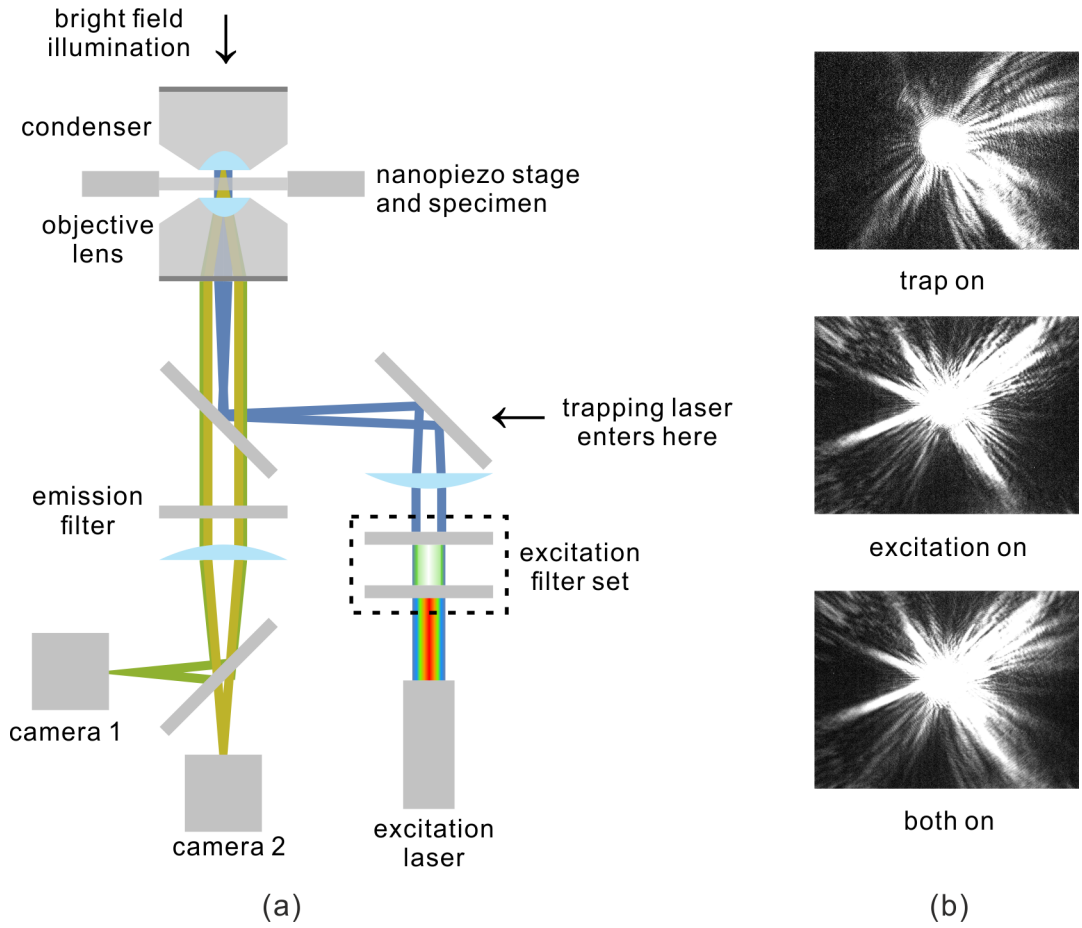

Figure 4.1: Excitation optics. (a) Optical diagram to illustrate the arrangement of excitation and imaging optics. (b) The excitation beam profile is concentric with the NIR trapping laser for early bead trapping experiments. The two beams appear at the same place on the camera.

4.1.2 Co-alignment of lasers

Fluorescence of dyes that non-specifically bind to the bead surfaces and autofluorescence of the beads themselves are sources of noise so need to be minimised. In slim-mode illumination, the extent of the excitation profile in the imaging plane needs to roughly coincide the extent of the transverse DNA molecule while the two beads at either end of the DNA lie at the tails of the Gaussian intensity of the excitation beam. However, at the stage of the calibration of the MOT, one of the characterisation of the tweezers involves the trapped magnetic bead being rotated and imaged in fluorescence. This requires the trapping and excitation laser beams to coincide. In theory, when the two are separately aligned, each should shoot through the centre of the objective lens. In practice, the beams are not so precisely centred and a mere $\sim 0.5\,\mu\mathrm{m}$ offset will be obvious on the camera. Thus, minor adjustments are needed in one of the beams so it is brought to coincide the other. Since any movement in the aligned trapping beam will decrease the trapping stiffness, which is the most crucial property of the optical tweezers, the trapping beam is kept untouched. The excitation beam is moved by walking it with a pair of mirrors so the bead ends up superposing the extent of the trapping profile and still passes vertically through the sample plane.

4.2 Emission optics

The imaging is done on two EMCCD cameras (iXon Ultra 897, Andor Technology Ltd.) of different wavelengths separated by a spectral colour splitter (TuCam, Andor Technology Ltd.). This is represented by the yellow and green rays in figure 4.1. The magnification on both cameras is 160 nm/pixel as measured with a graticule. For the imaging experiment described below, the EM gain is set to an absolute value of 300, the video sampling rate is 40 ms per frame (continuous) and typically 1000 frames are obtained per acquisition.

4.3 A DNA imaging experiment

Helen Miller and I have done preliminary super resolution dsDNA imaging experiments and obtained single molecular resolution imaging data. This is an integral part of the ultimate MOT with super-resolution fluorescence microscopy setup so this work here will prove useful for integration with the tweezers.

4.3.1 DNA preparation

We used λ-DNA (N3011S, NEB) as the tagged molecule as it has a contour length of $\sim 16.3\,\mu\mathrm{m}$ [136], which is long enough to allow easy observation. Oligonucleotides that have a part complementary to the 12 base pair overhangs are added to both ends of the DNA to allow a functionalisation group to be added to one end for tethering to a magnetic bead and a fluorophore (distinguishable from the fluorophores along the body of the DNA) to the other end for the identification of that end of the λ-DNA. The fluorophore end also has a functionalisation group for tethering to the coverslip surface. The magnetic bead end is functionalised with a single biotin molecule; the coverslip end with a Tex615 (a red fluorophore) and a digoxigenin. Figure 4.2 (a) shows a schematic of the end-modified λ-DNA design. The λ-DNA is in black and the end-modification oligomers in green and red. Table 4.1 contains the sequences of the oligomers (Integrated DNA Technologies). Figure 4.2 (b) to (d) show simulated DNA annealing at 37°C. There is low probability of unwanted self-annealing (c). The simulation is done with NuPack [137].

The protocol to modify the λ-DNA is as follows:

- 10 μM oligomers are phosphorylated using 1 unit of T4 polynucleotide kinase (Promega) in 1$\times$ T4 DNA ligase buffer (NEB) and incubated for 75 minutes at 37 °C.
- The DIG end was annealed in 1$\times$ T4 DNA ligase buffer with 1.5 nM λ-DNA and 20 nM oligomers 1 and 2 (see table 4.1) at 65°C for 5 minutes.
- The mixture is cooled to room temperature.
- 1 unit of T4 DNA ligase (NEB) is added to the mixture and the product incubated for 2 hours.
- A QIAEX II Gel Extraction Kit (Qiagen) is used to remove enzymes and excess oligomers.

The biotinylated end was attached using the same protocol. The DNA product is kept at 4°C for short and medium term storage and -20°C for long term storage.

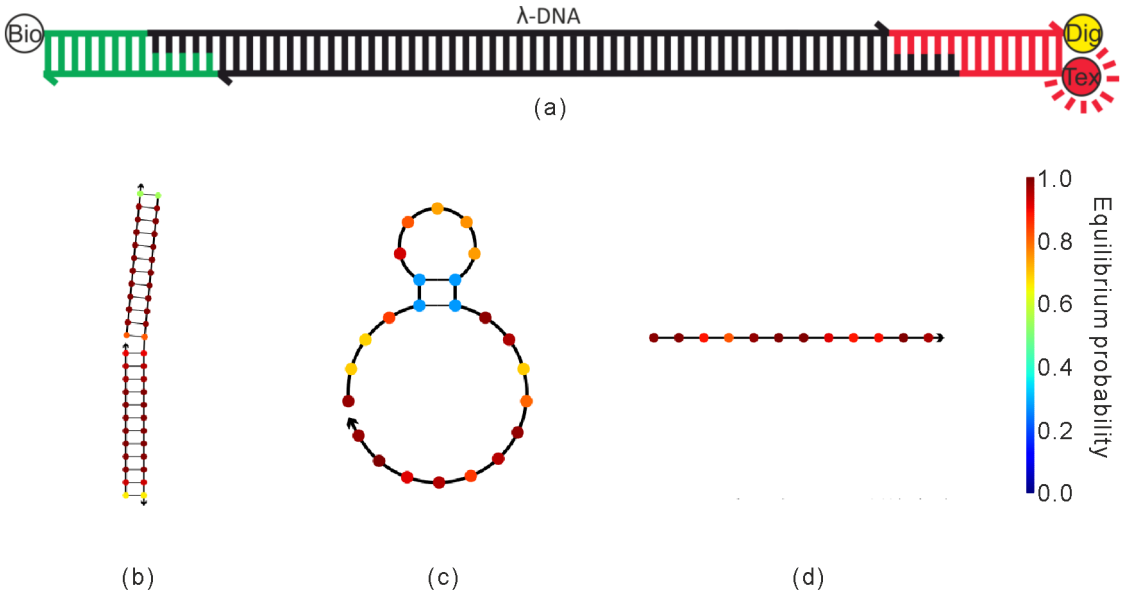

Figure 4.2: (a) A schematic of the end-modified λ-DNA design, with the biotinylated oligomer (green) and digoxigenin-Tex615-tagged oligomer (red) indicated. (b) Simulation of the configuration when the λ-DNA overhang, the dig oligomer and the fluorophore oligomers are mixed, at 37°C, with 1:1:1 concentration ratio. This is how we'd like the strands to behave. (c) When the dig oligomer is on its own in the solution, there is a small chance ($\sim$0.4) that bonds form between two pairs of nucleotides. When the other two strands are present, this dig oligomer binds to them much more readily. (d) When the fluorophore oligomer is on its own in the solution, no annealing happens.

oligomer	sequence
1	5′-AGGTCGCCCCCGTTCGTTGAGTCA-digoxigenin- 3′
2	5′-Tex615-GACTCAACGAAC-3′
3	5′-GGGCGGCGACCTGGACAGCAAGTTGGACAA-3′
4	5 ′ - biotin-TTGTCCAACTTGCTGTCC-3′

Table 4.1: Sequences of oligomers used to modify λ-DNA.

4.3.2 Imaging

The imaging is done on two different sample configurations. One with the solution sandwiched between a coverslip and a slide with no tape in-between and the solution volume kept to a minimum - see figure 4.3 - we call this the immobilization assay. The second assay is in a tunnel slide - see figure 4.7. In the former configuration the two glasses press on the DNA so the entropic coiling is overcome and the DNA molecules are extended. This way it is easier to identify the DNA. In the latter configuration the DNA will coil up and appear more or less as a blob in the image but the tunnel slide will be the eventual setup arrangement - see figure 5.1.

Reagents are diluted in 1$\times$ phosphate buffered saline (PBS; 10 mM phosphate buffer, 2.7 mM potassium chloride, 0.137 mM sodium chloride, pH 7.4, Sigma Aldrich). Two example DNA dyes are used to label the DNA: SYTO-13 (a minor groove binder, Life Technologies Ltd.) diluted to 50 µM and YOYO-1 Iodide (a intercalating dye, Life Technologies Ltd.) diluted to 10 µM. During sample preparation, care is taken to use large diameter pipette tips and to pipette slowly so the long λ-DNA is not or is minimally sheared.

For the immobilization assay, the following protocol is used. Where no waiting is specified, the step is taken out immediately.

- Plasma clean (in Harrick PDC-32G plasma cleaner) the coverslips for 1 minute at maximum power to remove impurities and to reduce autofluorescence.
- Mix 5 µL of 50 µM YOYO-1 Iodide with 5 µL of the 0.1 nM DNA product.
- Place 5 µL of the sample in the centre of a microscope slide. Place a coverslip onto the liquid droplet and make sure that no bubbles form and that the solution spans the whole coverslip surface area.
- Seal the edges of the sample with nail varnish to prevent evaporation.

For the tunnel slide assay, the following protocol is used. Again, where no waiting is specified, the step is taken out immediately.

- Plasma clean the coverslips for 1 minute at maximum power to remove impurities and to reduce autofluorescence.
- Mix 5 µL of 50 µM YOYO-1 i Iodide with 5 µL of the 0.1 nM DNA product.
- Lay two lines of double sided tape 3 mm apart on a microscope slide (VWR international, cat no. 631-0114) to produce a tunnel. Then lay the coverslip on the tape. Press the coverslip to seal.
- Introduce 5 µL of anti-digoxigenin ($1\,\mu\mathrm{g\,mL^{-1}}$, Roche Diagnostics) into the tunnel to functionalise the tunnel surface.
- Incubate in a humidity chamber with the coverslip side down for 5 minutes.
- Block the remaining free surface by flushing with 100 µL Bovine Serum Albumin (BSA, 0.1%, 1 mg/ml, Sigma Aldrich).
- Introduce 5 µL end-modified DNA into the tunnel.
- Flush the tunnel with 100 µL PBS solution.
- Seal the ends of the tunnel with nail varnish to prevent evaporation.

Figure 4.3 shows an example fluorescence image. When the excitation laser is let through to the sample space, initially continuous linear DNA structures are visible due to the high density labelling all or mostly in the emitting state. We see a combination of combed-out sections of single molecules of DNA and DNA with a more globular appearance. Averaging over the combed out DNA molecules seen in four separate acquisitions, stretched strands of DNA with mean lengths $17.6 \pm 2.5\,\mu\mathrm{m}$ are seen, consistent with the expected length of double-stranded λ-DNA of $\sim 16\,\mu\mathrm{m}$. The globular shaped DNA that are not flowed out following washing steps in the sample incubation protocols have measured diameters of $1.70 \pm 0.32\,\mu\mathrm{m}$. The worm-like-chain model [122, 138] predicts an end-to-end length of $\sim 2(L_c L_p)^{1/2}$, where L_c is the total contour length and L_p is the persistence length, which is about 50 nm. The model suggests 1.3–$1.4\,\mu\mathrm{m}$ for our observed globular DNA. When the DNA molecule is immobilized by spatial confinement, small sections of the DNA molecule

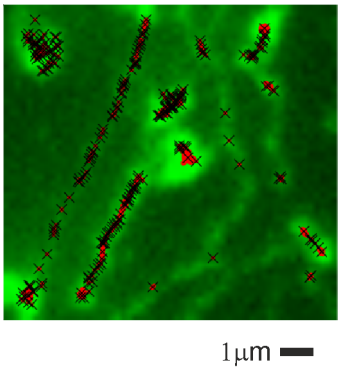

Figure 4.3: Fluorescence imaging of DNA in the immobilization assay. Fluorescence micrograph of YOYO-1 labelled λ-DNA (green) being squeezed between the slide and the cover slip to extend linearly. The green signals are the average of successive frames. In each frame, only a small fraction of the fluorophores are lit at random, allowing the location of individual fluorophores. This is possible because adjacent lit fluorophores are sufficiently apart so their point spread functions do not overlay and the centres of the PSFs can be determined. The coordinates of the fluorophores from many frames are all shown in the figure as black crosses (ie. ADEMS code reconstruction in red and clusters as black crosses). The pH is set to 7.4. The imaging buffer is $1\times$ phosphate buffered saline.

are stretched between surface attachments, giving a measured value slightly higher than the non-tethered prediction.

After a few frames' time under laser illumination, the DNA images move from continuous linear structures to sparse blinking along the same DNA molecules due to the bleaching of some but not all of the fluorophores. The latter regime allows superresolution imaging, and to determine the position and intensity of individual molecules by fitting the point spread function to the observed image. Photoblinking can be achieved with both SYTO-13 and YOYO-1. Figure 4.6 (a) shows consecutive frames each contains a random subset of fluorophores being in the emission state. An example intensity *vs* time plot of a fluorophore is found in (b). The fact that the fluorophore is on after staying in dark state for sometime shows that the dye can recover from bleaching.

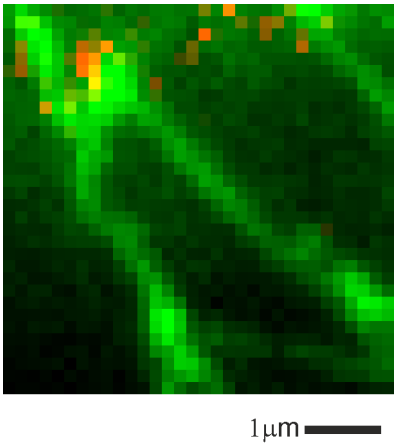

Figure 4.4: Overlaid green channel (DNA contour) and red channel (DIG end of DNA). The red fluorophore Tex615 marks the end of the DNA that is tethered to the coverslip surface. This serves as evidence that the DIG-antiDIG linkage has formed at the coverslip surface.

Figure 4.4 shows the reconstruction (red) from ADEMS code overlaid and cluster positions (black crosses). Many more spots are found in regions in the image with brighter laser illumination. In rainSTORM, localization precision is estimated using the formulation in [124]. The localization precisions from each of these methods for the YOYO-1 and SYTO-13 dyes are shown in Table 3. SYTO-13 is generally more poorly localized as it is much dimmer but the different methods largely agree.

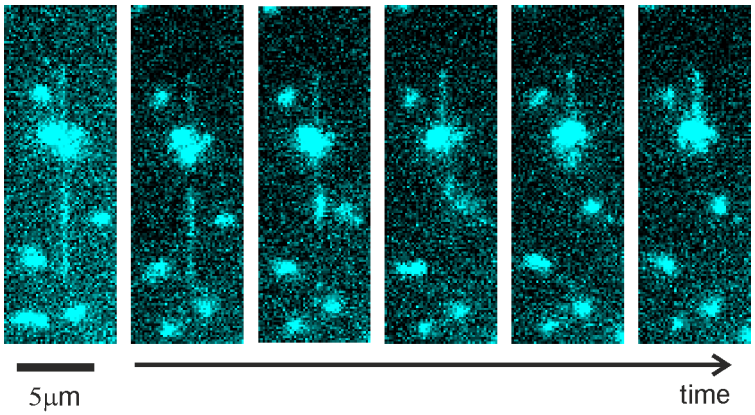

Figure 4.5: Sequential image frames of SYTO-13 labelled λ-DNA initially laid straight and then snapped and coiled due to laser induced oxygen-species free radical damages. In DNA-manipulation experiments, oxygen scavenging chemicals will be added to the imaging buffer to prevent such snapping. DNA ligase will also be used to repair any nicks in single strands should they arise - see section 5.5 for the contents of the imaging buffer.

Extended DNA strands can be seen to break at random time points under laser illumination, due to free-radical formation in the solution, illustrating that the imaging system is capable of monitoring real-time changes to DNA topology - see figure 4.5. The immobilized DNA assay undergoes Brownian motion and diffusion to a less extent so allows us to perform super-resolution reconstructions. The addition of the red organic dye Tex615 at one end of the λ-DNA enables the use of dual colour channels to identify the point of attachment to the surface - see figure 4.4 - demonstrating the imaging setup capable of performing dual colour co-localization imaging at a single molecule level.

We tested three software packagess with similar functionality to generate superresolution reconstruction images of the DNA molecules, the open source Quick-PALM [139], rainSTORM [140] and the in-house ADEMS software [141, 142]. They all identify bright spots in each frame, quantify their intensity and size and assess the quality of each detected spot. QuickPALM identifies bright spots in images using the Högbom 'CLEAN' method [143] and determines the spot centroid from its centre of mass. RainSTORM segments images to find bright spots using a top-hat algorithm to even out the background and thresholds the resultant image. The intensity centroid of these candidate spots is found using iterative Gaussian masking [124]. Spots are rejected if they have insufficient localization precision ($>$50 nm). ADEMS code also uses a top-hat transformation but with the addition of a dilation/expansion step followed by an erosion to reduce spurious candidate spots. 2D Gaussian masking is used to generate an estimate for the centroid, followed by a second stage involving a 2D Gaussian fit in which the Gaussian amplitude, local background offset and separate Gaussian sd values in x and y

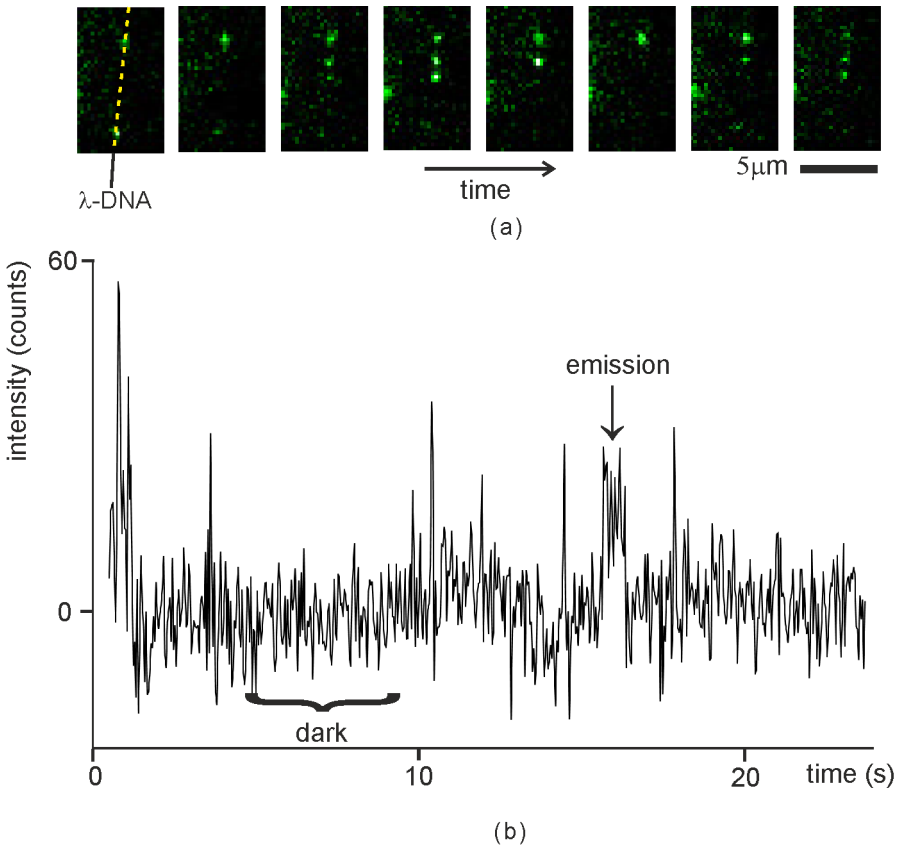

Figure 4.6: Stochastic DNA-binding dye photoblinking. (a) An example of stochastic YOYO-1 photoblinking (green) from consecutive image frames. The dashed line in frame 1 marks a λ-DNA. (b) An example intensity *vs* time trace of a single YOYO-1 fluorophore bound to λ-DNA, showing the integrated pixel intensity over each dye's PSF minus the local background intensity. We observed dark states lasting up to 10 seconds and bright 'on' states in the range of 10 – 1000 ms.

are free to vary but with the centroid coordinates from the first masking stage fixed. This two-stage approach resulted in greater robustness for fitting, converging at the very low values of SNR equivalent to dim single dye molecule signals, compared to using a fully unconstrained one-stage 2D Gaussian fit. Different criteria are used for accepting a spot – the SNR must be above a threshold which can be correlated to robust statistical probabilistic confidence criteria. Localization precision is calculated from the sd of the intensity centroid positions from different frames and independently by cluster analysis, which links proximal fluorescent spots into a cluster and provides a measure of the localization precision from the mean intra-cluster distances. The localization precisions of the three methods for are shown in table 4.2. SYTO-13 has lower precision due to its dimness.

	rainSTORM	ADEMS code centroid distribution	ADEMS code mean cluster distance
YOYO-1	35 nm	40 nm	41 nm
SYTO-13	67 nm	62 nm	90 nm

Table 4.2: Summary of localization precision for the three algorithms. Units are all nm.

In separate imaging attempts, super-paramagnetic beads (Dynabeads MyOne^{TM} Streptavidin C1, Life Technologies Ltd. - see table 6.1) were incubated with the DNA construct. Briefly, the protocol is as the following:

- Plasma clean the coverslips for 1 minute at maximum power to remove impurities and to reduce autofluorescence.
- Mix 10 µL of 50 µM YOYO-1 Iodide, 5 µL of the 0.1 nM DNA product and 5 µL of the paramagnetic beads nM at $100\,\mu\mathrm{g\,mL^{-1}}$ in an eppendorf tube.
- Mix by manual flicking every 2.5 minutes for 30 minutes to avoid sedimentation.
- Assemble the tunnel slide with BSA blocking and - see the tunnel slide protocol above.
- Introduce 5 µL bead-DNA solution into the tunnel.
- Flush the tunnel with 100 µL PBS solution.
- Seal the ends of the tunnel with nail varnish to prevent evaporation.

We tested whether the beads were tethered to the DNA molecules at the biotin-functionalised end by first observing whether any bead was positioned at an end of a DNA molecule. They could be found but they were rare. Among the ones that did appear to have tethered - an example is shown in figure 4.7, we held a magnet close to the sample and pulled the bead away. But the DNA were not pulled taut and the bead diffused away without taking the DNA with it. We concluded that no convincing evidence of tethering was found in this instance of tether creation. I improved the functionalised DNA later by labelling the DNA with multiple biotin molecules (also multiple digoxigenin molecules at the other DNA end) - see chapter 5.

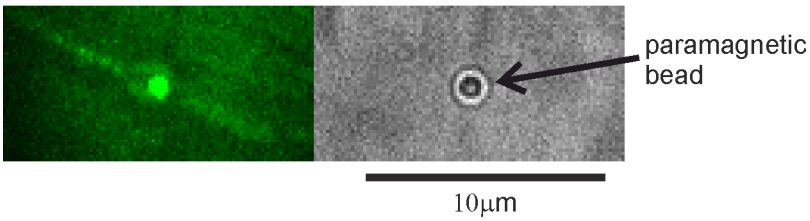

Figure 4.7: Fluorescent and bright field images of a super-paramagnetic bead with two DNA molecules at two sides of the bead. The fluorescent image was taken in the green camera channel. Unfortunately, this by itself is not enough evidence that tethering was formed between the end of the DNA molecules and the bead.

Both photoblinking and transient binding can contribute to stochastic single fluorescence emission events. I modelled the photoblinking due to transient binding to reach the conclusion that the emission events are actually mostly due to photoblinking rather than transient binding. YOYO-1 is a fluorogenic dye in the sense that its brightness increases by typically two orders of magnitude when bound to DNA compared to unbound. I calculated the on-rate at which free dye molecules bind to DNA in equilibrium, and the average binding lifetime that a dye stays bound to DNA; a low on-rate indicates that fluorescence emission events are rarely due to new binding of free dye from solution, whereas a long binding lifetime in principle allows a typical dye molecule more time to

stay on the DNA to undergo cycles of photoblinking. The kinetics of binding and unbinding between DNA binding sites and dyes are given by equation 4.1, which describes how the occupation of a DNA binding site changes in equilibrium:

$$\frac{d[\text{site} \cdot \text{dye}]}{dt} = k_{on}[\text{site}][\text{dye}] - k_{off}[\text{site} \cdot \text{dye}] \tag{4.1}$$

where $[\text{site} \cdot \text{dye}]$ is the concentration of dye-bound DNA sites, $[\text{site}]$ is the concentration of empty sites, $[\text{dye}]$ is the concentration of free dye in solution and k_{on} and k_{off} are the on-rate and off-rate constants respectively. At equilibrium, equation 4.1 is equal to 0 so

$$\frac{[\text{site} \cdot \text{dye}]_{eq}}{[\text{site}]_{eq}[\text{dye}]_{eq}} = \frac{k_{on}}{k_{off}} = K_a \tag{4.2}$$

where K_a is the association constant.

Solving equation 4.1 gives pre-equilibrium reactions and solving equation 4.2 gives the concentrations of the components and allows the calculation of the on-rate and lifetime. To find out how long it takes to reach 50% of equilibrium occupancy of dye binding sites when DNA is mixed with dye, equation 4.1 is re-written as:

$$\frac{dx}{dt} = k_{on}([\text{site}]_0 - x)([\text{dye}]_0 - x) - k_{off}x \tag{4.3}$$

where $x \equiv [\text{site} \cdot \text{dye}]$, $[\text{site}]_0$ is $[\text{site}]$ at $t = 0$ and $[\text{dye}]_0$ is $[\text{dye}]$ at $t = 0$. The solution is summarised in figure 4.8, with values for k_{on} obtained from literature. The 50% binding equilibrium point is reached after about 30 ms.

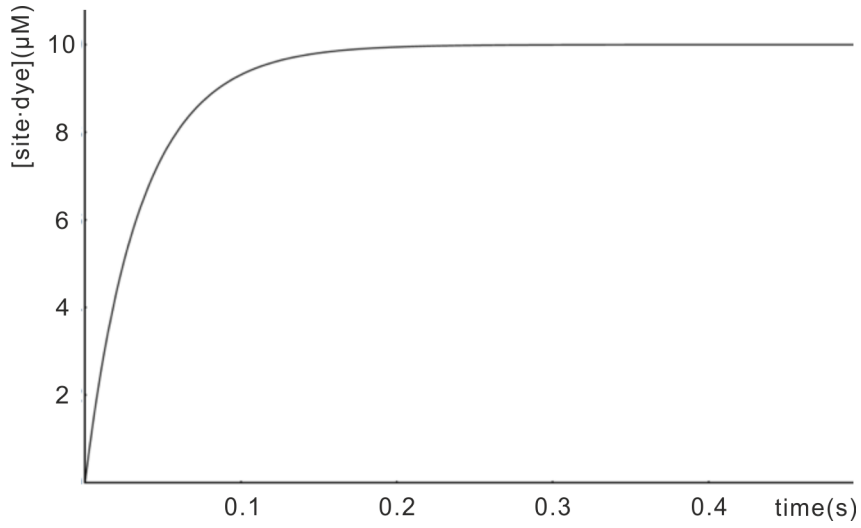

Figure 4.8: Kinetics of dye binding to DNA.

At equilibrium, equation 4.2 can be expressed as

$$\frac{[\text{site} \cdot \text{dye}]_{eq}}{([\text{dye}]_0 - [\text{site} \cdot \text{dye}]_{eq})([\text{site}]_0 - [\text{site} \cdot \text{dye}]_{eq})} = K_a \tag{4.4}$$

whose solution is

$$[\text{site} \cdot \text{dye}]_{eq} = \frac{1}{2}\left([\text{site}]_0 + [\text{dye}]_0 + \frac{1}{K_a} - \sqrt{([\text{site}]_0 + [\text{dye}]_0 + \frac{1}{K_a})^2 - 4[\text{site}]_0[\text{dye}]_0}\right) \tag{4.5}$$

Plug in $[\text{site}]_0 = 1.59 \times 10^{-9} \times 48502 = 7.71 \times 10^{-5}\,\text{M}$ where $1.59 \times 10^{-9}\,\text{M}$ is the concentration of DNA and 48502 is the number of base pairs in λ-DNA, and $[\text{dye}]_0 = 10^{-5}$ M, and assuming $K_a = 10^{10}\,\text{M}^{-1}$ (obtained from literature), we get

$$[\text{site} \cdot \text{dye}]_{eq} = 9.9999851 \times 10^{-6}\,\text{M}^{-1} \tag{4.6}$$

and

$$\frac{[\text{site} \cdot \text{dye}]_{eq}}{[\text{site}]_{eq}[\text{dye}]_{eq}} = 7 \times 10^5 \tag{4.7}$$

which shows the vast majority of the dyes are in bound statues in equilibrium.

The blinking behaviour we observe is consistent with our expectation from the modelling, the code of which is shown in appendix A.4. This is evidence that we observe photoblinking rather than binding and unbinding behaviour of the fluorescent dye.

Chapter 5

DNA assay

In this chapter I describe the wet-lab processes to create torsionally constrainable double stranded DNA, the construction of single molecular DNA dumbbell assay and force/torque transduction experiments.

5.1 Functionalised DNA

For twisting-DNA type experiments, the double stranded DNA molecule needs to be rotationally constrained at both ends. One way to achieve this is through the dumbbell configuration: one bead tethered to one end of the DNA and another bead to the other end. As figure 5.1 shows, the beads are functionalised (ie. having tethering molecules attached to them) over the whole surface and the ends of the DNA are functionalised over a length along the DNA (as opposed to just a point at the end of the DNA) so the bead-DNA tethers are at multiple points. This is the key to the rotational locking of the bead-DNA tether. To produce such DNA, a double stranded DNA (dsDNA) is used as the central part and two functionalised dsDNA (referred to as 'functionalised handles' below) are added to the ends of the central part. The central part needs to be at least $\sim 1\,\mu\mathrm{m}$ long, or about ~ 3000 base pairs (bp), in length so there is enough space to image the dynamics of the molecule. There is no upper limit on the length but vibrational noise scales linearly with the length and the efficiency/quality of producing the DNA also increases with length. I have chosen to use a

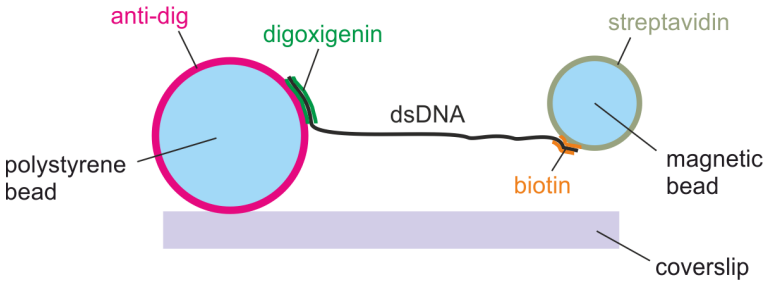

Figure 5.1: Arrangement in the DNA assay. The 5 µm anti-DIG bead is immobilised to the coverslip surface. One end of the DNA is tethered to the bead. The other end of the DNA is tethered to a magnetic bead, which is tapped with the optical tweezers (not shown). The beads and DNA are approximately drawn to scale, assuming a $\sim 10\,\mu\mathrm{m}$ contour length DNA.

$\sim$ 3 kbp dsDNA as the central part. The functionalised handles will need a sufficient number of tethering molecules to form a strong tether. The minimum length can be

determined experimentally. I chose $\sim$ 500 bp for both handles. The procedures for creating such DNA are based on Y. Seol's protocol [144] with modifications to suit our purpose. First, I create the central part. Figure 5.2 is a graphical representation of this process. As I ignore the effect GC content has on the stiffness/dynamics of the DNA for now, any commercially available linear DNA or plasmids longer than about 3 kbp will be fine. Y. Seol used the pET-28a (+) plasmid so I will also use this. Then a 3 kbp part from the plasmid is selected for polymerase chain reaction (PCR) to multiply into a large number of 3 kbp linear dsDNA. Primers that match the ends of the 3 kbp region are ordered from a commercial supplier for PCR. The primer sequences are found in figure 5.2. The final step is restriction reactions with BfuAI at one end and BsaI at the other to turn the blunt ends into overhangs for the later annealing with the handles. Then, I create the handles at both

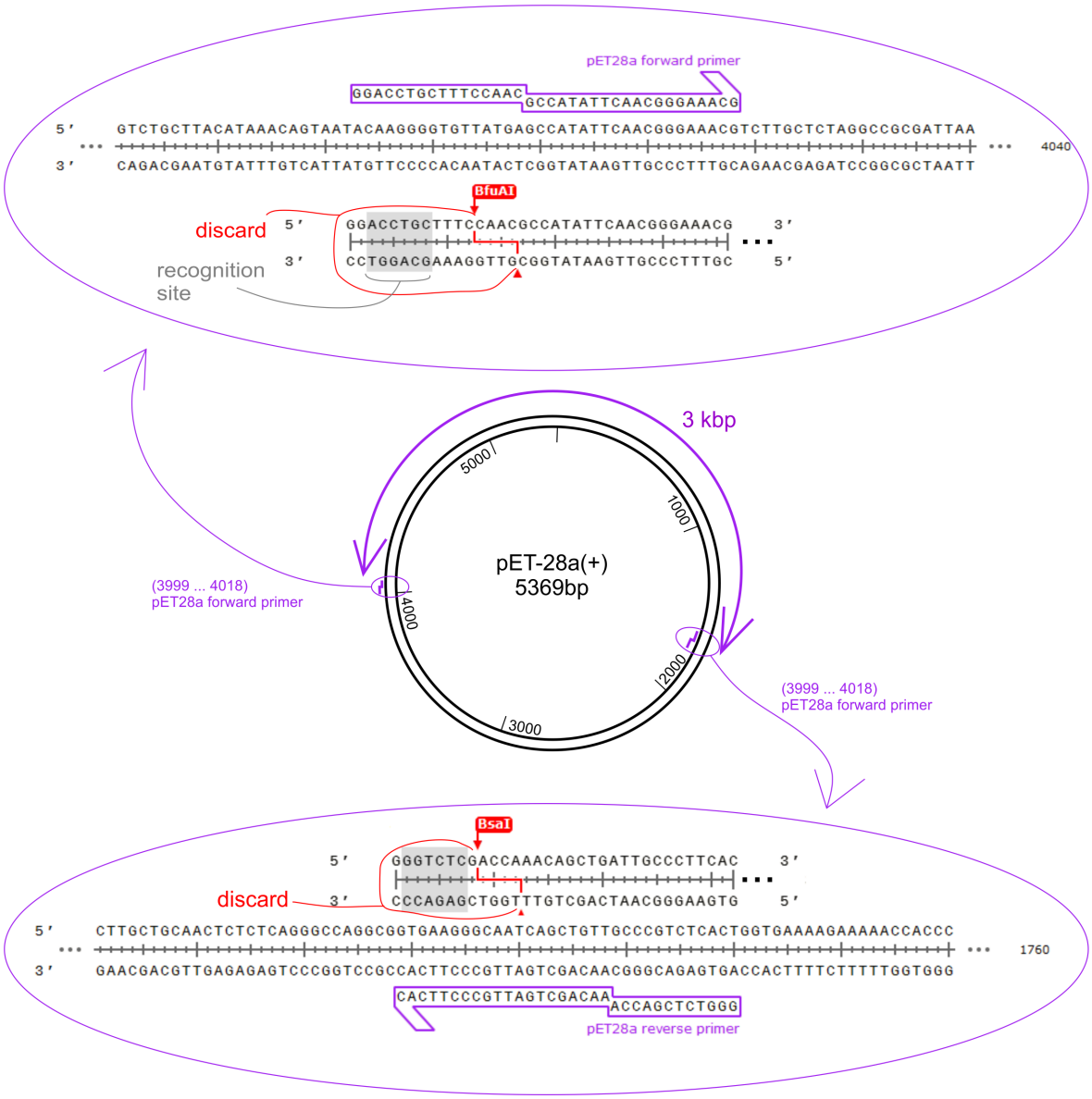

Figure 5.2: Schematics to show the process to create the $\sim$3 kbp central part of the torsionally constrainable dsDNA. A pET-28a (+) plasmid first undergoes PCR with two primers designed such that the PCR products are 3 kbp blunt-end dsDNA, which then has both its ends cut with (different) restriction enzymes as shown in the purple bubbles.

ends of the central part. Figure 5.3 depicts this. The process to obtain $\sim$500 bp linear

dsDNA is similar to that used to obtain the central part, except that the dNTPs in the PCR have biotin-dUTP and digoxigenin-dUTP mixed in so that the end products will have biotin and digoxigenin present. See the table below for details of the biotin and dig used.

	Biotin-16-dUTP	DIG DNA Labeling Mix
provider	Jena Bioscience	Roche
molecule name	biotin-16-5-aminoallyl-dUTP	digoxigenin-11-dUTP
main ingredients	1 mM biotin-dUTP	1 mM dATP, 1 mM dCTP, 1 mM dGTP, 0 65 mM dTTP, 0 35 mM DIG-dUTP
molecular weight	948 g/mol	1091 g/mol
molecules : dTTPs	1:2	7:53
molecules per handle	85	30

The plasmid to use this time is pBluescript II (+). In the biotin-tagged handle, biotin-dUTP to dTTP ratio is 1:2. For a 509 bp dsDNA with 4 nt overhang, there are $509 \times 2 + 4 = 1022$ nucleotides (nt). I approximate that a quarter of the nucleotides are dTTP or dUTP so there are approximately $1022 \times 25\% \times 1/3 = 85$ biotin molecules per handle. In a digoxigenin-tagged handle, there are 30 digoxigenin molecules. After the PCR, the biotin handle is cut with BfuAI only and the dig handle with BsaI only. This way, each type of handle will attach to a specific end of the central part. The actual attachment is done by mixing the the three parts together and adding DNA ligase. Figure 5.4 depicts the final product.

For convenience, I calculate the molecular weight of pBluescript, pET28a, the central part, the handles and the construct (ie. the central part + the handles). The MW of dsDNA is equal to $(\text{no. of nt} \times 607.4) + 157.9\,\text{Da}$. The addition of $157.9\,\text{Da}$ to the MW is due to the MW of a $5'$ triphosphate. For example, pBluescript has 2961 bp, so $2 \times 2961 \times 607.4 + 157.9 = 3597\,\text{kDa}$. $1\,\text{nM}$ pBluescript in $\text{g}\,\text{L}^{-1}$ is $1\,\text{nM} \times 3597\,\text{kDa} = 3.597\,\text{ng}\,\mu\text{L}^{-1}$. For another example, biotin handle has 509 bp and 4 nt overhang, so $(2 \times 509 + 4) \times 607.4 + 157.9 = 621\,\text{kDa}$. There are 85 biotins per handle, so $85 \times 948 = 81\,\text{kDa}$. So the total handle weight is $621 + 81 = 702\,\text{kDa}$. The values for various DNA are listed in table 5.1. The blue lines in the table are dsDNA before restriction reactions.

	bp	overhang	nt	biotin/dig	MW (kDa)	1 nM in ng µL^{-1}
pBluescript	2961	0	5922	0	3597	3.60
pET28a	5369	0	10738	0	6522	6.52
biotin handle	525	0	1050	88	721	0.72
dig handle	525	0	1050	31	671	0.67
central part	3127	0	6254	0	3799	3.80
biotin handle	509	4	1022	85	702	0.70
dig handle	513	4	1030	30	659	0.66
central part	3099	4+4	6206	0	3770	3.77
construct	4129	0	8258	85+30	5129	5.13

Table 5.1: The molecular weights of various DNA involved in the creation of torsionally constrainable DNA are calculated. Conversion factors from molar concentration to mass concentration is also listed in the last column for convenience as they are used later.

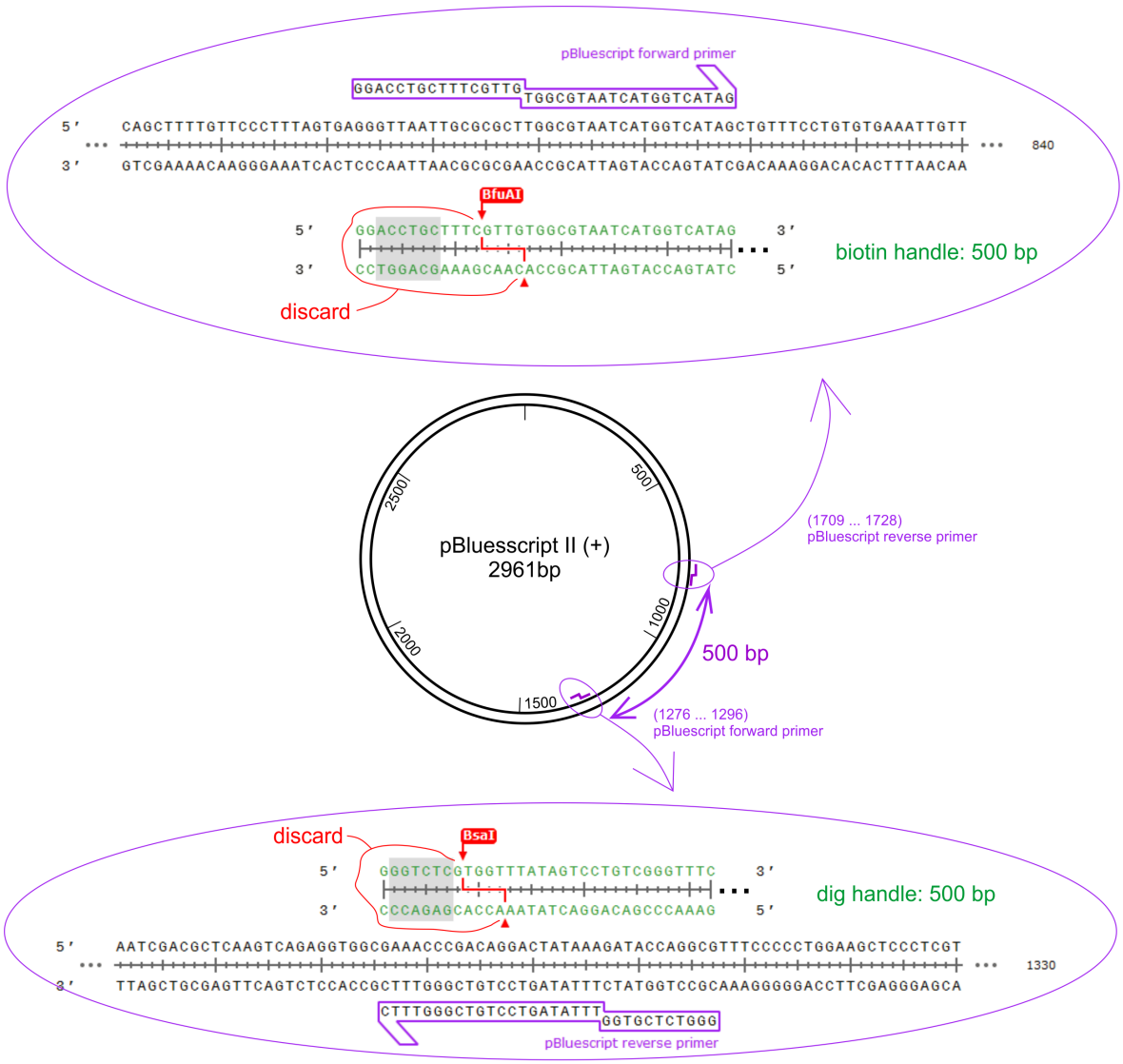

Figure 5.3: Schematics to show the process to create the ∼500 bp functionalised handles. A pBluescript II (+) plasmid undergoes PCR with two primers designed such that the PCR products are ∼500 bp blunt-end dsDNA, which is then split into two eppendorf tubes one of which has a DNA end cut with the restriction enzyme BsaI and the other of which cut with BfuAI.

5.2 The protocol

The protocol that I used to create such DNA is detailed below. The instructions are sufficiently complete so one can reproduce the torsionally constrainable DNA following this protocol.

Step 1. Procure the following primers from a commercial supplier:

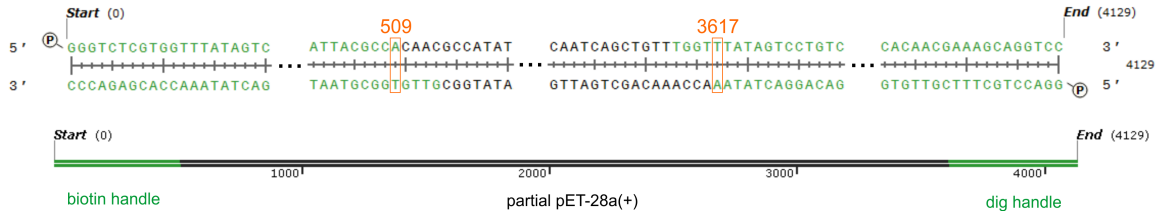

Figure 5.4: Schematics to show the torsionally constrainable DNA. The handles are in green where the central part in black. The position of the junctions are labelled with nucleotide numbers (orange).

primer name	mass (mg)	amount (nmol)	sequence
pET28a forward	8.14	739.3	5′-GGACCTGCTTTCCAACGCC ATATTCAACGGGAAACG- 3′
pET28a reverse	6.90	707.6	5′-GGGTCTCGACCAAACAGCT GATTGCCCTTCAC-3′
pBluescript forward	7.65	688.5	5′-GGACCTGCTTTCGTTGTGGC GTAATCATGGTCATAG-3′
pBluescript reverse	6.96	704.7	5 ′ - GGGTCTCGTGGTTTATAG TCCTGTCGGGTTTC-3′

and add 1000 µL double distilled water to each tube to obtain:

primer name	amount (nmol)	add water (µL)	conc (µM)
pET28a forward	739.3	1000	739
pET28a reverse	707.6	1000	708
pBluescript forward	688.5	1000	689
pBluescript reverse	704.7	1000	705

Step 2. Further dilute the primers by taking 1 µL primer solution from each tube and adding 9 µL water to each solution:

primer name	vol (µL)	add water (µL)	final conc (µM)
pET28a forward	1	9	73.9
pET28a reverse	1	9	70.8
pBluescript forward	1	9	68.9
pBluescript reverse	1	9	70.5

Step 3. Mix the following chemicals in a PCR tube for PCR reaction to generate the central part. Note that GoTaq Green (2x) is composed of 400 µM dATP, 400 µM dGTP, 400 µM dCTP and 400 µM dTTP so the amount of dNTP is $400\,\mu M \times 12.5\,\mu L \times 4 = 20000\,pmol$. Central part is 6254 nt so 20000 pmol dNTP has the potential to make $20000/6254 = 3.2\,pmol$ central parts. pET28a is measured with a NanoDrop 2000/2000c Spectrophotometer to have initial concentration of 92.6 ng/ul = 14.2 nM. It is known that the spectrophotometer may have significant error so the measurement is only a reference. Initial concentration means concentration of reagents before mixing; final concentration means that after mixing.

chemical	vol (µL)	initial conc (µM)	final conc (µM)	amount (pmol)
GoTaq Green 2x	12.5	2×	1×	-
pET28a forward	0.5	73.9	1.48	37
pET28a reverse	0.5	70.8	1.42	35.5
pET28a	3	14.2×10^{-3}	1.7×10^{-3}	42.6×10^{-3}
water	8.5	-	-	-

Step 4. Mix the following in a PCR tube for PCR reaction to generate the digoxigenin functionalised handles. The grey texts are components of the reagent in the line above them. It is necessary to write out each dNTP both for GoTaq Green and for the labelling reagent to calculate the number of dig on each handle. The pBluescript above is measured with a NanoDrop 2000/2000c Spectrophotometer to have initial concentration of 486 ng/ul = 135 nM. So the final concentration is 0.5/25 x initial conc = 9.72 ng/ul = 2.7 nM. The total dNTP is 30000, the handles are 1050 nt long, so the reaction can make $30000/1050 = 28.6\,\mathrm{pmol}$ handles.

chemical	vol (µL)	initial conc (µM)	final conc (µM)	amount (pmol)
GoTaq Green 2x	12.5	2×	1×	-
dATP	-	400	200	5000
dGTP	-	400	200	5000
dCTP	-	400	200	5000
dTTP	-	400	200	5000
DIG labeling mix 10x	2.5	10×	1×	-
dATP	-	1000	100	2500
dGTP	-	1000	100	2500
dCTP	-	1000	100	2500
dTTP	-	650	65	1625
dig-dUTP	-	350	35	875
pBluescript forward	0.5	68.9	1.38	34
pBluescript reverse	0.5	70.5	1.41	35
pBluescript	0.5	135×10^{-3}	2.7×10^{-3}	68×10^{-3}
water	8.5	-	-	-

Step 5. Mix the following in a PCR tube for PCR reaction to generate the biotin functionalised handle. The effective amount of dNTP for each species is $5000\,\mathrm{pmol}$, so can make $5000 \times 4/1050 = 19.0\,\mathrm{pmol}$ products.

chemical	vol (µL)	initial conc (µM)	final conc (µM)	amount (pmol)
GoTaq Green 2x	12.5	2×	1×	-
dATP	-	400	200	5000
dGTP	-	400	200	5000
dCTP	-	400	200	5000
dTTP	-	400	200	5000
DIG labeling mix 10x	2.5	10×	1×	-
biotin-dUTP	-	1000	100	2500
pBluescript forward	0.5	68.9	1.38	34
pBluescript reverse	0.5	70.5	1.41	35
pBluescript	0.5	135×10^{-3}	2.7×10^{-3}	68×10^{-3}
water	8.5	-	-	-

Step 6. Perform PCR reaction to create and amplify the wanted linear parts of the plasmids. Yellow highlight means the 3 steps as a whole are repeated 30 times.

step	temperature	time	no. of repeats
initial melting	98°C	2 min	1
melting	98°C	15 sec	
annealing	60°C	30 sec	30
elongation	72°C	5 min	
final elongation	72°C	15 min	1

Step 7. Clean up the three PCR reactions using QIAquick PCR purification kit (QIAGEN, Cat No./ID: 28104). This step removes the primers but not pET28a or pBluescript as they are too big for the purification kit to remove. The reagents created so far are summarised below. The amount of all parts have been discounted by 5% to take into account the loss during purification. The volume is set by the last step of the purification.

DNA	amount (pmol)	vol (µL)	conc (nM)
central part	3.04	50	61
dig-handle	27.2	50	543
biotin-handle	18.1	50	361

Step 8. Restriction digestion to cut out the overhang for each part. Mix the following in three Eppendorf tubes. Incubate at 50°C overnight. The restriction enzymes are BfuAI (R0701S), BsaI (R0535S) and the buffer is NEBuffer 3.1 (R7203S), all of which are procured from NEB.

	vol (µL)
central part	40
BfuAI	1
BsaI	1
10x NEBuffer	5
water	8

	vol (µL)
dig-handle	40
BfuAI	0
BsaI	1
10x NEBuffer	5
water	9

	vol (µL)
biotin-handle	40
BfuAI	1
BsaI	0
10x NEBuffer	5
water	9

Step 9. Purification of the three reagents following the same procedures as in step 7. Below is calculated and measured concentration. 5% discount is applied to the calculation again to account for purification loss. The table also compares the two concentrations and

finds that calculated concentrations are about 10 time higher than measured concentrations. I theorize that this is due to the inaccurate NanoDrop 2000/2000c Spectrophotometer concentration measurement (measured twice) as well as loss of reagents down the pipeline.

	measured conc ($\mathrm{ng\,\mu L^{-1}}$)	calculated conc ($\mathrm{ng\,\mu L^{-1}}$)	difference
central part	18.0	174	$9.7\times$
dig-handle	17.7	273	$15\times$
biotin-handle	13.8	192	$14\times$

Step 10. Ligation. Mix the following. Incubate at room temperature overnight. This is the final product. The product is not purified because the presence of ligase helps repairing nicks formed in the DNA strands, which will be useful for the DNA to stay torsionally constrainable. For the amount and concentration of parts, measured values from step 9 are used rather than calculated values. As the construct concentration will be limited by the central part, which is $0.72\,\mathrm{nM}$.

	vol (µL)	amount (pmol)	conc (nM)
central part	3	14.3×10^{-3}	0.72
dig-handle	3	80.5×10^{-3}	4.02
biotin-handle	3	59.1×10^{-3}	2.96
T4 DNA ligase	1	-	-
10x T4 DNA ligase buffer	2	-	$1\times$
water	8	-	-

5.3 Gel testing

Agarose gel electrophoresis is a method to separate a mixture of DNA by their sizes and to determine the sizes. The agarose gel I use is made by dissolving $0.5\,\mathrm{g}$ solid agarose powder (A0169, Sigma-Aldrich Co. LLC.) in $50\,\mathrm{mL}$ $1\times$ Tris-Acetate-EDTA (TAE) buffer (T9650-1L, Sigma-Aldrich Co. LLC.) to make 1% w/v agarose solution. The solution is microwaved at low power ($200\,\mathrm{W}$) until the solution boils and the powder fully dissolves. To make the DNA visible in the gel, $5\,\mu\mathrm{L}$ SYBR Safe DNA Gel Stain (S33103, Thermo Fisher Scientific Inc.) is added to the gel solution. The gel solution then is poured into a mould which is fitted with a well-forming comb. Cooling down to room temperature over half an hour results in the formation of a solid gel. Agarose gels are submerged in Tris-borate-EDTA (TBE) buffer (BP24301, Thermo Fisher Scientific Inc.) in a horizontal electrophoresis apparatus. TBE buffer conducts electric current during electrophoresis. $5\,\mu\mathrm{L}$ DNA samples are added with $1\,\mu\mathrm{L}$ purple gel loading dye (B7024S, New England Biolabs, or NEB), which migrates at approximately the speed of a 300 bp DNA. The dye serves the purposes of making the DNA samples denser so sink to the bottom of the well, and allowing the experimenter to assess how fast the band migration is. The power is set at about $100\,\mathrm{V}$ for half an hour. After electrophoresis, the gel is placed in an imaging enclosure (ChemiDoc$^{\mathrm{TM}}$MP Imaging System), which contains a charge-coupled device (CCD) camera to capture images. The imager has built-in blue epi LED and UV light sources, both of which can be used to image the fluorescent SYBR Safe-stained DNA separation pattern.

Agarose gel electrophoresis are performed at several points to check if the protocol in section 5.2 creates the expected DNA products. At the end of step 6, I have the central part, and dig and biotin tagged handles. Their molecular weights are listed in table 5.1. The gel to test the correctness of the sizes of the DNA are shown in figure 5.5. I add avidin to the biotin-handles from step 9 in the protocol above. Since each avidin binds up to 4 biotin molecules, multiple handles can join together to form a mesh of DNA, hugely increasing the collective molecular mass and resulting in the mesh staying in the well of the gel. In contrast, biotin-handles without avidin added have MW of 702 kDa so will migrate along the track. Below is a table of reagent mixing and predicted results in a gel run. Note since each anti-digoxigenin (anti-DIG) binds to 2 dig molecules, DNA mesh will again form in the presence of anti-DIG.

sample	MW (kDa)	predicted behaviour
biotin handle	702	move
dig handle	659	move
central part	3770	move
biotin handle + avidin	large	stay in well
dig handle + anti-DIG	large	stay in well
construct + avidin	large	stay in well
construct + anti-DIG	large	stay in well

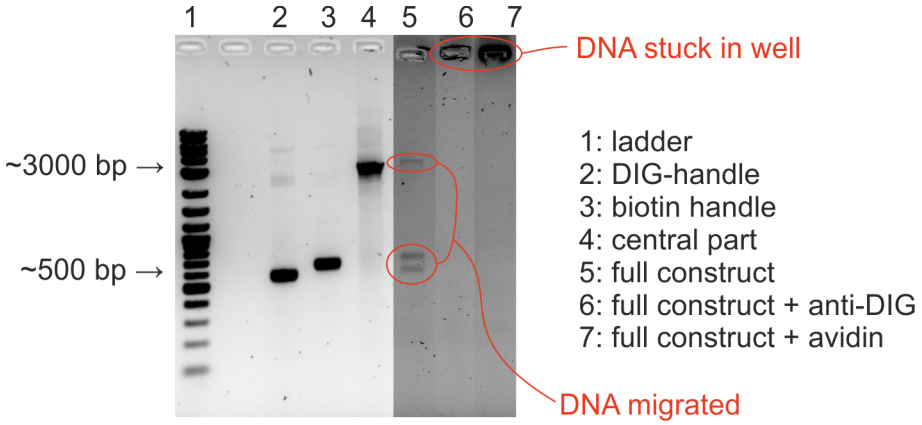

Figure 5.5: A photograph of agarose gel electrophoresis to show the production of torsionally constrainable DNA. Lane 1 is the 1 kbp DNA ladder (N3232L, NEB) serving as a reference to which other lanes can be compared to in order to evaluate the migration distance of other lanes. Lane 2 and 3 are the DIG and biotin handles respectively. Lane 4 is the central part. Products in all three lanes are more or less of the correct molecular weight. There are faint bands of heavy DNAs in lane 2 and 3, which are the plasmids from which the handles are made. Lane 5 is the full construct, which shows up as a band in the upper red circle. The lower red circle contain bands corresponding to unbound handles. When either anti-DIG or avidin is added (land 6 and 7), the bands corresponding to those in lane 5 disappear and the wells show stuck DNA (see the red circle on the top of lane 6 and 7) - this proves that the DNA end functionalisation has worked. Note that lane 5 to 7 have had their brightness decreased in software to enhance the appearance of the bands.

5.4 Buffer

A buffer is a solution with an acid and its conjugate base in it so that the solution experiences a small change in pH value with added acid or base. Single molecular experiments such as DNA twisting experiments are done with biological molecules dissolved in such buffers since a certain pH range protects the DNA from degradation. Also salt is added to protect the double stranded structure. DNA are negatively charged so the two strands repel each other. Positive ions from the salt bind to both strands and reduce the repelling force. pH of 7.4 [105, 107], 7.8 [145–147] and 8.0 [148, 149] have been used in the literature. One widely used buffer, Phosphate-buffered saline (PBS), has an osmolarity and ion concentrations that match those of the human body but PBS makes the magnetic bead adsorb nonspecifically to coverslip surfaces readily thus leaves a small time window for the experimenter to find a bead to trap. I use the buffer in [150] with the following ingredients. The pH value of Tris-HCl applies at $32°\mathrm{C}$.

reagent	concentration
Tris-HCl (pH 7.5)	$40\,\mathrm{mM}$
KCl	$30\,\mathrm{mM}$
NaCl	$25\,\mathrm{mM}$
MgCl2	$1\,\mathrm{mM}$
DTT	$1\,\mathrm{mM}$
BSA	$1\,\mathrm{mg\,mL^{-1}}$

The pH value of Tris-HCl applies at $32°\mathrm{C}$. Tris-HCl with a pH specified actually means a mixture of Tris-HCl and Tris base. Since Tris-HCl is acidic and Tris base is basic, mixture of the two at different ratios can create buffers with pH in the range 7 and 9. I make Tris-HCl (pH 7.5) by dissolving $5.64\,\mathrm{g}$ Tris-HCl and $1.72\,\mathrm{g}$ Tris base in $1\,\mathrm{L}$ double distilled water ($\mathrm{ddH_O}$). Calculation of amount of Tris and Tris-HCl to get the blend with the wanted pH at specified temperature:

when nTrisBase mol of TrisBase and nTrisHCl mol of TrisHCl are mixed, it's equivalent to when (nTrisBase+nTrisHCl) mol of TrisBase and nTrisHCl mol of HCl are mixed. Because HCl is a strong acid, all H^+ is separated from Cl^-. So nTrisHCl mol of H^+ bind with nTrisHCl mol of TrisBase to form nTrisHCl mol of $TrisH^+$, leaving behind nTrisBase mol of TrisBase.

5.5 Stretching DNA

I have stretched and rotated single dsDNA molecules. The mechanical responses of these DNA have been reported in literature so the ones I obtain can serve as proof-of-principle data to show the viability of my magneto-optical tweezers. In this section I describe the findings of stretching a dsDNA. The assay arrangement is as illustrated in figure 5.1. The dsDNA is 30-kbp long. The protocol for making the DNA is not described in this thesis but it is similar to making the 4-kbp DNA as shown in section 5.2, with the difference being the central 3-kbp part being replaced by a 30-kbp stretch from lambda DNA.

The following steps are carried out to assemble the assay

- Plasma clean (in Harrick PDC-32G plasma cleaner) the coverslips for 1 minute at maximum power to remove impurities and to reduce autofluorescence.

- Dilute nitrocellulose (Collodion solution, 09817-100ML, Sigma-Aldrich Co. LLC.) in amyl acetate to make 0.1% nitrocellulose in amyl acetate. This is done in a fume hood.
- Submerse the coverslips for a few seconds in nitrocellulose; then allow to air dry propped up at an angle on lint-free paper.
- Assemble a tunnel slide by sandwiching a slide, two strips of double-sided tapes and a coverslip.
- Flow in anti-dig beads, which is diluted 1 in 10 from stock concentration in $1\times$ phosphate buffered saline + 400 mM KCl. Turn tunnel slide upside down and wait 5 minutes.
- Wash with 200 µl phosphate buffered saline + 400 mM KCl.
- Flow in $1\,\mathrm{mg\,ml^{-1}}$ bovine serum albumin.
- Turn tunnel slide upside down and wait 5 minutes.
- Stain DNA by mixing 119 µl $1\times$ phosphate buffered saline + 400 mM KCl + 10 µl $1\,\mathrm{mg\,ml^{-1}}$ bovine serum albumin + 1 µl 1 mM YOYO-1 Iodide (Catalog number: Y3601, Life Technologies Ltd.) + 30 µl 0.1 nM DNA.
- Flow in the DNA mixture.
- Wash with 200 µl phosphate buffered saline + 400 mM KCl.
- Prepare imaging buffer by mixing 10 µl 40 $\%$ glucose, 10 µl YOYO-1, 10 µl 10 $\times$ ligase buffer, 1 µl T4 DNA ligase, 10 µl $1\,\mathrm{mg\,ml^{-1}}$ bovine serum albumin, 5 µl fluorescent beads (FluoSpheres, 505/515 nm, 0.04 µm, F8766) diluted 1 in 1000 from stock concentration, 5 µl magnetic beads (micromer-M, streptavidin, 08-19-303, micromod Partikeltechnologie GmbH) diluted 1 in 100 from stock concentration, 1 µl catalase, 1 µl gloxy, 1 µl Trolox.
- Flow in the imaging buffer.
- Wash with 200 µl phosphate buffered saline + 400 mM KCl.

The slide is then mounted onto the slide holder with immersion oil applied both between the coverslip and the objective lens and the slide and the condenser lens. The magnetic bead

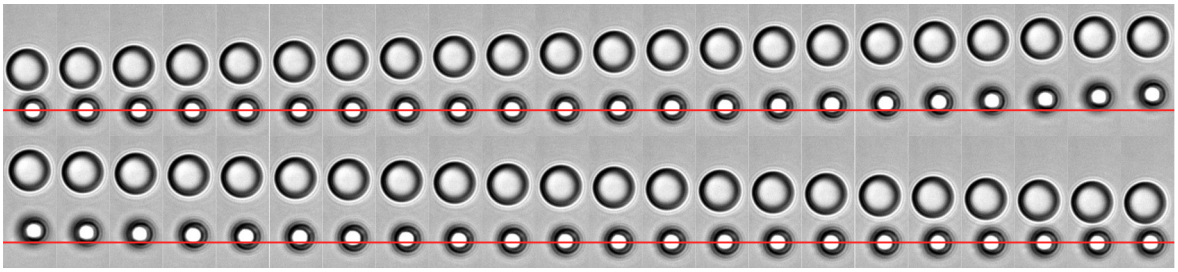

Figure 5.6: The anti-dig bead oscillates about the magnetic bead, resulting in the latter being pulled away from of the trap centre and then back towards the centre again. The red line is drawn to serve as a ruler.

is first trapped in the optical tweezers. An anti-dig bead is then manually brought to the

vicinity of the magnetic bead using the coarse stage. The two beads are allowed to stay close together for a few seconds to allow a DNA tether (or multiple tethers) to form. The nanostage is then oscillated with an amplitude approximately equal to that of the contour length of the DNA. When the two beads are maximally apart, the magnetic bead is just about to be pulled out of the trap. Figure 5.6 shows consecutive bright field frames of the action. A red line is added to assist visual determination of the position of the magnetic bead. Initially the two beads are close and the magnetic bead is in the centre of the optical tweezers trap. As the anti-dig bead moves away, the magnetic bead deviates from the trap centre but stays trapped. Just when the magnetic bead is almost pulled out of the trap, the anti-dig bead moves towards the trap again.

This is repeated for repeated measurements. The bright field images allow the determination of the separation of the two beads and thus the physical stretching of the DNA molecule. QPD signals are taken concurrently to allow the determination of the force applied to the bead. Figure 5.7 shows V_{TB} for three consecutive cycles. The peaks correspond to the magnetic bead away from the centre of the trap. The noisy curves between adjacent peaks are due to the anti-dig bead, which is close enough to the trap to cause perturbations in the QPD signals.

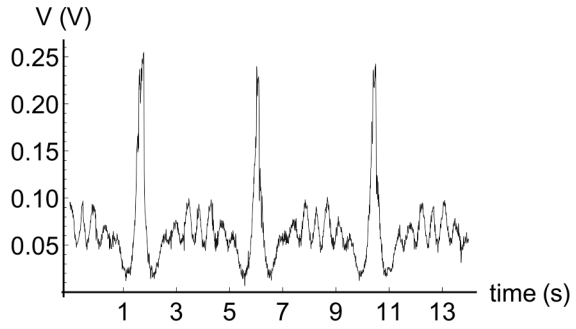

Figure 5.7: The QPD signal for stretching DNA, which corresponds to the motions in figure 5.6.

After a few cycles of tapping, fluorescent images are taken on the same bead-DNA-bead combinations by switching on the excitation laser. For this purpose, the excitation laser is no longer concentric with the trapping laser. Rather, the two are offset by a few μm so that the DNA is now centred on the excitation field. Figure 5.8 shows the first 5 frames of the fluorescence video. It can be seen that the DNA bleaches over time. It is hoped that by optimising the experimental settings, single molecular resolution can be achieved so that any plectonemes formed due to twisting can be seen. The data I have now show early promising developments towards the goal.

5.6 Twisting DNA

The above assay is also twisted for plectoneme formation. For twisting, the two beads are placed at a separation so that the magnetic bead is about to fall out of the trap. The nanostage is not turned on. Instead, the magnetic tweezers start to rotate the magnetic bead. Figure 5.9 shows V_{LR} QPD signals taken. As more and more rotations are introduced into the DNA, the end-to-end length shortens and the average QPD voltage level moves away from the equilibrium position. At about 175th turn, the magnetic bead abruptly falls out of the

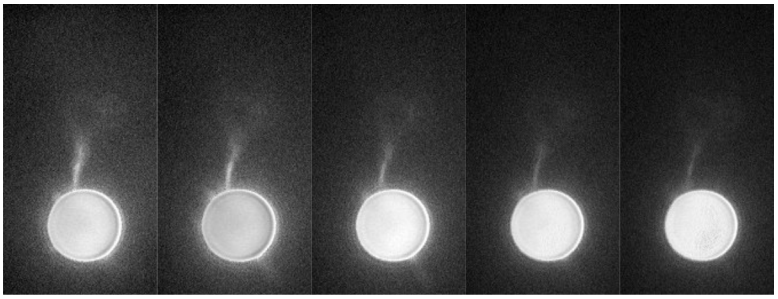

Figure 5.8: The first 5 frames of a fluorescent movie to show a DNA tethered between two beads.

optical trap, resulting in the QPD signal suddenly returning to the equilibrium position.

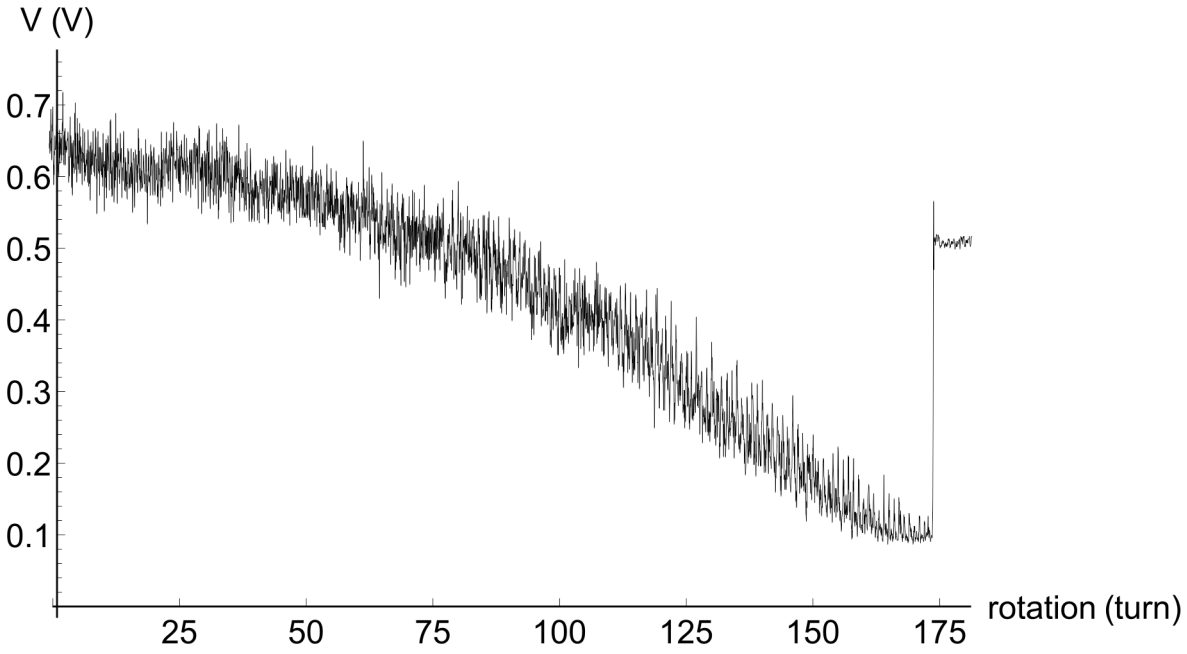

Figure 5.9: The QPD signal for twisting a DNA tethered between the two beads.

A close look at the plot reveals the oscillation about the mean position due to the rotation of the magnetic bead.

Chapter 6

Discussion

Some details of the designing, building and characterising of the magneto-optical tweezers do not really fit into the flow of the narrative in the main text but need to be considered or are interesting to know will be discussed in this chapter. Also I will critically evaluate my own work and, on paper only, explore possibly better alternatives.

This chapter will also point out directions for future work as the MOT as of now are a work in progress. There are many aspects of calibration and testing, and possibly extra design features, that I hope can be carried out in the future. In a bigger picture, this work is about creating the instrumentation, which brings about the tools for conducting single molecule biological experiments. It is those experiments where scientific discoveries are made. A few experimental ideas are briefly described for potential biological experiments.

6.1 About the design

Some points regarding the designs are brought up retrospectively in this section. I also include negative aspects of the design ideas.

6.1.1 Coil diameter

In hindsight, I could have made the number of turns for the big coils fewer since, with the same current supplied to the big coils and the small coils, the big coils generate 2.8 times larger $\mathbf{B}$ field at the biological sample. So in operation, the current supplied to the small coils are always 2.8 times greater (see equations 3.17 and 3.19). Had I designed the big coils with fewer turns, similar levels of currents could be supplied to both pairs of coils. However, there is no adverse effect with my current design, other than spending about £3 more on the 3D printing material!

I made the interesting observation that the thickness of wires used to wind coils does not affect the temperature rise of the coils. To prove this, I assume that wires of various thickness are used to generate the same $\mathbf{B}$ field, and show that the rate of heat generation is independent of wires used. From equation 3.3, we know that B scales linearly with I. Since B also scales linearly with the number of turns, n, in the coil,

$$B \propto In \Rightarrow I \propto \frac{B}{n} \tag{6.1}$$

Let l be the length of coils and A be the cross-sectional area of the copper wire, the resistance

of coils is

$$R \propto \frac{l}{A} \tag{6.2}$$

Since the space in the spool is finite so the higher A is, the fewer turns can fit in, so

$$A \propto \frac{1}{n} \tag{6.3}$$

Substitute $l \propto n$ and equation 6.3 into equation 6.2:

$$R \propto \frac{n}{1/n} = n^2 \tag{6.4}$$

Substitute equation 6.1 and 6.4 into equation for power dissipation:

$$P = I^2 R \propto \left(\frac{B}{n}\right)^2 n^2 = B^2 = \text{constant} \tag{6.5}$$

6.1.2 Criticism

One drawback with this design is the magnetic bead, which absorbs light so heats up. This dictates that only weak trapping laser powers can be used with the current choice of magnetic beads. However, the heating problem and thus the low power problem can be overcome with magnetic beads with lower content of magnets, which will be discussed in more detail below.

Another issue is the limitation posed on the range of movement of the nanostage. This is due to the change in the $\mathbf{B}$ field with respect to position away from the centre of the trap. But more crucially the existence of the small pair of coils prevent the slide from moving to certain positions. This problem does not really prevent experiment from performed - we simply has fewer useful fields of view per slide.

6.2 Future work

In this section I will comment on further steps in building the instruments as well as a range of potential experiments to be carried out.

6.2.1 Instrument characterisation

The properties of both the optical trap and the magnetic field will depend on the magnetic content of the bead. In the former, the Fe_3O_4 shell in the bead absorbs and scatters light much more than polystyrene that is typically used to make beads for optical tweezers without magnetic manipulation. First, this will greatly increase the height of the bead above the trap focus. The second effect is heating of the bead. Lastly, the lateral stiffness is reduced due to the reduced proportion of light being refracted (more light is absorbed). In the magnetic tweezers, the angular stiffness k_θ is proportional to the magnetisation of the bead - see equation 3.10. The manufacturer specified a 5% coefficient of variance in the diameter. If we take the cubic of 1.05, we get 1.16 - a 16% deviation from the mean value in volume and thus in k_θ. And this is assuming the magnetisation per unit volume is constant, which may not be the case (the manufacturer did not specify the coefficient of variance in magnetisation per unit volume). These large variations in k_θ calls for a proper

characterisation of the bead's magnet content. Measurements on hundreds rather than two or three beads are needed to better approximate the statistical distribution. This can be done for example with a DC magnetic property measurement system (MPMS-SQUID sensor) [151]. A similar point can be made of the volume and the opacity of the magnetic beads. These directly influence the displacement-*vs*-voltage calibration of the QPD - see figure 2.5 - so a statistical distribution will need to be obtained for error estimation of the measurement of any experimental bead. Alternatively a displacement-*vs*-voltage calibration can be obtained for every bead used in the experiments.

The second point is about magnetic bead heating. Combining optical and magnetic tweezers have long been recognised as a straightforward approach to utilise the strength of both techniques (force application from the former and torque from the latter) but the challenge of heating due to the iron oxide absorption of light places such hurdles that only a small number of attempts have been made [116, 152, 153]. Indeed when I trapped the magnetic bead at higher laser powers, there was so much heating that the magnetic bead exploded and sometimes the solution in the vicinity of the bead started to boil. The laser power thus has to be kept low and thus the trapping stiffness is kept under $100\,\mathrm{pN\,\mu m^{-1}}$. A "large" force on the dsDNA is $\sim\ 65\,\mathrm{pN}$ at which the dsDNA melts so a $\sim\ 0.65\mu\mathrm{m}$ displacement from the trap centre will be needed to reach this force level, which can be encountered in experiments. This is quite large compared to the FWHM radius of $\sim 0.5\,\mu\mathrm{m}$ laser trap. The best solution to this problem is to lower the magnetic content of the bead. The micromer®-M bead used in this project is not the first bead I tried. Table 6.1 shows the various beads I have tried to trap with the optical tweezers. Spherotech magnetic bead was

product make	micromer®-M	Dynabeads®	Spherotech
product code	08-19-303	65001	SVFM-20-5
surface	streptavidin	streptavidin	streptavidin
bead diameter $(\mu\mathrm{m})$	3	1	2.45
coefficient of variation in diameter	$< 5\%$	$< 5\%$	na
bead volume (m^3)	1.41×10^{-17}	5.24×10^{-19}	7.7×10^{-17}
density $(\mathrm{kg\,m^{-3}})$	1100	1100	1100
bead mass, m_b (kg)	1.56×10^{-14}	5.76×10^{-16}	8.5×10^{-14}
saturation magnetisation $(\mathrm{A\,m^2\,kg^{-1}})$	6.6	na	189
streptavidin wt per bead wt $(\mathrm{ng\,mg^{-1}})$	700	15000	2240
material	ferrite	ferrite	chromium dioxide
formula	Fe_3O_4	Fe_2O_3	CrO_2
Fe_mO_n content by wt	$9 - 14\%$	37%	-
Fe content by wt	$6 - 10\%$	26%	-
substrate	polystyrene	polystyrene	polystyrene
structure	shell	uniform	shell
magnetism	superparamagnetic	superparamagnetic	ferromagnetic
appearance	brown	brown	black

Table 6.1: Comparison of all the magnetic beads that I have used in this project. Only the micromer®-M one seemed to have worked.

the first considered bead as the magnetic field in the MT is quite small. A the beginning I

thought that superparamagnetic beads need a sizeable magnetic field to magnetise them before they can respond to the rotating background field. By contrast, the Spherotech bead being ferromagnetic will not require any background field to keep the magnetisation. However, The chromium(IV) oxide renders the beads very weakly trapped by the laser beam. Later on, I accidentally used some Dynabeads® for tweezing and surprisingly they respond strongly to the rotating magnetic field. However, I was soon disappointed because the Dynabeads® almost never traps due to the 37% Fe_3O_4 content that absorbs and scatters NIR light. The fact that the ferrite particles are uniformly distributed in the volume of the beads may play a role in the opacity of the beads as well but this will need some modelling to confirm. The micromer®-M bead has about a third to a half the ferrite content compared to that of the Dynabeads® and it can be trapped easily and consistently. Since my MT design provides more than enough torque for many biological experiments, there is room for further reduction of magnet content. I am not aware of mass-produced commercial beads that have lower ferrite level but bespoke ones can certainly be made. This will be the most efficient approach to solving potential bead explosion and solution boiling problem at high laser power and also allow higher optical trapping stiffness to be applied. There also exists anti-reflection coated, high-refractive-index titanium dioxide microspheres, which (without embedded magnetic particles), achieved nanonewton optical forces [154]. It may be the case that such beads will have better trapping properties even when Fe_3O_4 is embedded. Another point about the heating is the need to quantify the rise in temperature as it may affect biomolecular properties such as the elasticity of DNA and the processivity of proteins.

A third point to consider is the evaluation of k_z so that I will have obtained $\mathbf{k}$ in all three dimensions. The trapping force mainly lies in the transverse plane but if there is a vertical component, it will need to be added into the resultant force for a more accurate evaluation. Another reason for knowing k_z is the use of magnetic beads, which decreases k_z more than lateral stiffness. Also, the depth of the trapped bead away from the optimum position reduces k_z most. Caution needs to be taken to prevent k_z from falling too low. However, the method developed to measure k_x and k_y does not apply to detecting axial stiffness because of the incompatibility to detecting axial motion. The most straightforward method for determining axial motion is by overfilling the photodiode with the laser beam and measuring the intensity of scattered laser light. This works because the bead changes the divergence of the exiting light depending on its z-position [155]. Other methods include two-photon fluorescence generated by the trapping laser and evanescent-wave fluorescence at the surface of a coverslip [156]. To implement the first method, a second QPD can be added to the microscope. The light emerging from the condenser is split into two perpendicular branches with a beam splitter. One branch is used for lateral stiffness and the other, having a different divergence, for axial stiffness measurement. A simpler method, just as the lateral stiffness measurement, utilises the interference between the scattered and the unscattered beam at the back focal plane of the condenser [157, 158]. The difference between the interference-based method to measure the lateral and the axial stiffness is that the former measures the pairwise difference as a function of lateral bead positions while the latter measures the sum as a function of axial bead positions. The axial counterpart to equation 1.11 can be expressed as [157]:

$$V_{SUM} \approx \frac{8k'\alpha}{\pi\omega_0^2}\left(1+\left(\frac{z}{z_0}\right)^2\right)^{-1/2}\sin\left(\arctan\frac{z}{z_0}\right) \tag{6.6}$$

where all the symbols have the same meaning as in equation 1.11 and z_0 is the Rayleigh length.

6.2.2 Alternative assay

The MOT have the flexibility of accommodating other assay configurations and thus are open to a wider type of experiments. If the laser trap is multiplexed, and the anti-DIG bead trapped rather than immobilised to the coverslip, a dumbbell assay will be formed. This provides a less noisy trap so more precise localisation of fluorophores. Such a configuration has been shown to measure sub-nanometre RNA polymerases advancements on DNA [10]. Maybe this is the key to resolving the supercoils mentioned in section 6.2.1.

A related alteration is in the throughput increase so as to gather statistics in single molecule properties. The MT are intrinsically high throughput while the OT can be multiplexed into a large number of arrays with holography - a spatial light modulator creates individually controllable local maxima and minima in a single trapping beam so multiple beads can be trapped in it [86]. This cab also be combined with multi-well microfluidic systems

A clear path for improving throughput requires the development of ways for parallel tracking of many individual molecules (as in TIRF), either by exploiting the capabilities of newer computers and CPUs to achieve simultaneous real-time tracking of multiple particles or by carrying out parallel reactions in multi-well microfluidic systems, such as those for high-throughput single molecule sequencing [33,62]. It is likely that the increase in throughput will appeal to the pharmaceutical industry, which so far has not shown strong interest in adapting these approaches for drug discovery and characterization and ultra-sensitive diagnostics.

6.2.3 Biological experiments

The immediate experiment will be DNA stretching and rotating with concurrent fluorescence microscopy to image individual fluorophores. This will serve as a proof-of-principal experiment to show that the instrument has the claimed capabilities. At the moment this work is already in progress and some preliminary results have been obtained - see sections 5.5 and 5.6. The complete set of experimentation and analysis will also include (1) plotting the force-extension curve of the supposed DNA to confirm that the magnetic bead is pulled out of the trap by a DNA tether rather than other types of interaction, (2) fluorescence imaging of the whole contour of the DNA as opposed to the partial DNA as shown in figure 5.8, preferably achieving a resolution of ~ 20 nm as that in an sandwiched assay, ie. the coverslip presses on the slide so that the DNA molecule is stretched out and largely immobile, (3) the end-to-end length dependence on the number of rotations introduced into the DNA molecule at both above- and below-threshold tension levels. The breakthrough will be in the fluorescence video recordings of the DNA topological changes as the turns are applied. Loenhout et al. were able to show dynamics of DNA supercoils by real-time fluorescence imaging of torsionally manipulated DNA.

They found the existence of a fast hopping process that facilitates rapid plectoneme displacement [46]. The plectonemes show up as single PSFs due to the lack of spatial resolution. It would be interesting to see if we can visualise the loops of the supercoils. Many other DNA elastic and dynamic studies such as the sequence dependence of DNA bending energy can be reproduced but with fluorescence to provide auxiliary information.

DNA-protein complexes are another direction of research. Due to the large number of the DNA processing proteins, and the complicated interaction between molecules, opportunities exist for many interesting catalytic pathways to be revealed. The MOT's innovative design to interface the high versatility of trapping/rotating with the high resolution of fluorescence microscopy allows the unravelling of molecular biology in its full complexity. For example, DNA stretching has been shown to be useful in probing natural and perturbed DNA compaction, the most stunning case perhaps being DNA packaging motors that push DNA into pre-assembled virus capsid [98].

In processes that involve the coordinated action of many proteins such as DNA repair, the different species of proteins can be tagged with distinguishable coloured fluorophores so the functions of each can be interrogated. A related topic is the compacting of DNA by supercoiling in prokaryotes or by wrapping around histones in eukaryotes. Also, the single-base-pair resolution has the potential to reveal detailed mechanisms in DNA replication, its rate, processivity, pausing and fidelity.

6.3 Other comments

Here I try to explain why counter propagating tweezers or video based force measurements are not possible alternatives to my approach.

Counter propagating tweezers use the gradient force and scattering forces from opposing beams to provide the axial and longitudinal confinement of the trapped object. One advantage of such tweezers is the cancellation of the scattering forces due to the largely opaque magnetic beads, since the scattering forces from the two beams are opposite each other. The main difficulties are the alignment of the two beams, which has to be quite precise for the cancellation to be achieved. Also due to the implementation of the QPD above the condenser, there is no convenient way to introduce the second beam.

Video based force measurements suffer from low frame rate of CCD cameras. If I were to use the power spectrum method to calibrate the stiffness of the optical trap, the frame rate will need to be at least higher than the corner frequency, which potentially reach 1000 Hz. This is beyond the frame rate of most CCD cameras.

Appendix A

Appendices: Codes and algorithms

Here I include the codes I wrote for this PhD project. LabVIEW codes control the instruments and Mathematica codes analyse data and render graphical display of results. The latest versions of these codes are printed in Appendix A. Brief explanations of the functions of each snippet of codes accompany the codes in the same font as that of the main text. The font of the codes is Consolas.

A.1 Stiffness calculation for the optical tweezers

The voltage-time data from the measurement of bead positions are exported from LabVIEW into .lvm files. and put in the same folder as the Mathematica file. First, the working directory of Mathematica is set to this folder and all .lvm file names collected. A few variables are defined to be a set containing a fixed number of dummy entries for later use.

```
SetDirectory[NotebookDirectory[]];
dataFiles = FileNames[__ ~~ ".lvm"];
placeholder = Range[Length[dataFiles]];
plotDisp = plotPower =
   fitLR = fitTB = fitSUM =
      dataLR = dataTB = dataSUM = maLR = maTB = maSUM =
            PowerSpectrumLR = PowerSpectrumTB = PowerSpectrumSUM =
               kxEquipartition = kyEquipartition = placeholder;
```

I then define the scaling of some ticks which will be used when graphs are plotted. Also defined are the model to fit the Lorentzian curve, the values for Boltzmann constant and the absolute temperature. A few more variables are defined but this time values will be set by the user every time the code runs. ”number” indexes the files as there are multiple measurement files in the same folder; ”conversionFactorx” and ”conversionFactory” are the constants that convert voltage from the QPD to real displacement values; ”start” and ”end” allow the user to discard values at the very beginning and the very end, which may be unstable.

```
ticks1 := {Table[{50000 i, i}, {i, 0, 100, 5}],
  Table[{10^-9 i, i}, {i, -500, 500, 100}]}
ticks2 := {Table[{50000 i, i}, {i, 0, 100, 5}], Automatic}
```

```
model = a/(b^2 + f^2);
kB = 1.38 10^-23;
T = 300;
{number, conversionFactorx, conversionFactory, start, end} =
  DialogInput[{number = 1, conversionFactorx = 1.15,
    conversionFactory = 1.4, start = 1, end = -1},
   Column[{
     "type in file number:",
     InputField[Dynamic[number], Number],
     "Specify \!\(\*SubscriptBox[\(\[Sigma]\), \(x\)]\): 1V = ?\[Mu]m",
     InputField[Dynamic[conversionFactorx], Number],
     "Specify \!\(\*SubscriptBox[\(\[Sigma]\), \(y\)]\): 1V = ?\[Mu]m",
     InputField[Dynamic[conversionFactory], Number],
     "Data start at line:",
     InputField[Dynamic[start], Number],
     "Data end at line:",
     InputField[Dynamic[end], Number],
     Button["OK",
      DialogReturn[{number, 10^-6 conversionFactorx,
        10^-6 conversionFactory, start, end}],
      ImageSize -> Automatic]}]];
```

The data in in each .lvm file are a 2D array. Each row is the data for a time point. The columns are time, V_{LR}, V_{TB}, V_{SUM}, etc. Each column is loaded into a variable below:

```
For[n = 1, n <= Length[dataFiles], n++,
  data = Import[dataFiles[[n]]][[start ;; end]];
  length = Length[data];
  time = length/50000.;
  dataLR[[n]] = data[[All, 2]];
  dataTB[[n]] = data[[All, 3]];
  dataSUM[[n]] = data[[All, 4]];
```

V_{LR} and V_{TB} are then converted from voltage to displacement as well as normalised. Also, the DC component is removed as it is not relevant to the power spectrum method and it needs to be gone to reflect the Brownian fluctuation about the mean position.

```
  meanSUM = Mean[dataSUM[[n]]];
  dataLR[[n]] = conversionFactorx dataLR[[n]]/meanSUM;
  dataTB[[n]] = conversionFactory dataTB[[n]]/meanSUM;
  dataLR[[n]] = dataLR[[n]] - Mean[dataLR[[n]]];
  dataTB[[n]] = dataTB[[n]] - Mean[dataTB[[n]]];
```

For the equipartition theorem method to find the trapping stiffness, the displacement data are plugged into equation 1.10 for both x- and y-directions. The "print" command is used so the code can spit out a sentence, whose content is not of interest, to tell the user that the code has run one iteration. This is done as the data samples are large and it can take a while

to run the code. Periodical printing shows that the calculation is not stuck. Afterwards, displacement-time scatter plots are produced.

```
kxEquipartition[[n]] = (kB T)/RootMeanSquare[dataLR[[n]]]^2;
kyEquipartition[[n]] = (kB T)/RootMeanSquare[dataTB[[n]]]^2;
Print[{dataFiles[[n]], "\tData length =", length}];
plotDisp[[
  n]] = {ListLinePlot[dataLR[[n]], PlotStyle -> Black,
   ImageSize -> Medium, PlotLabel -> "L-R ",
   AxesLabel -> {"t/s", "x/nm"}, Ticks -> ticks1],
  ListLinePlot[dataTB[[n]], PlotStyle -> Black, ImageSize -> Medium,
    PlotLabel -> "T-B ", AxesLabel -> {"t/s", "y/nm"},
   Ticks -> ticks1],
  ListLinePlot[dataSUM[[n]], PlotStyle -> Black,
   ImageSize -> Medium, PlotLabel -> "SUM ",
   AxesLabel -> {"t/s", "V/V"}, Ticks -> ticks2]};
```

The code then calculates the power spectrum density by taking the Fourier transform of the discrete time series and absolute squared. This is done for V_{LR}, V_{TB} all V_{SUM} though V_{SUM} will not be used later. Then the power spectrum density series are added a time stamp for later plotting.

```
PowerSpectrumLR[[n]] = ((Abs[Fourier[dataLR[[n]]]]^2)/50000)[[
  1 ;; length/2]];
PowerSpectrumTB[[n]] = ((Abs[Fourier[dataTB[[n]]]]^2)/50000)[[
  1 ;; length/2]];
PowerSpectrumSUM[[n]] = ((Abs[Fourier[dataSUM[[n]]]]^2)/50000)[[
  1 ;; length/2]];
PowerSpectrumLR[[n]] =
 Table[{i/time, PowerSpectrumLR[[n, i]]}, {i, 1,
   Length[PowerSpectrumLR[[n]]]}];
PowerSpectrumTB[[n]] =
 Table[{i/time, PowerSpectrumTB[[n, i]]}, {i, 1,
   Length[PowerSpectrumTB[[n]]]}];
PowerSpectrumSUM[[n]] =
 Table[{i/time, PowerSpectrumSUM[[n, i]]}, {i, 1,
   Length[PowerSpectrumSUM[[n]]]}];
```

The code for fitting uses Mathematica's built-in FindFit function. No settings are modified and by default Mathematica uses Levenberg–Marquardt method for least-squares fit. After fitting, the PSD as well as the fit curve are plotted. Finally the plots are exported to .png images in the same folder.

```
fitLR[[n]] =
 FindFit[PowerSpectrumLR[[n, 10 ;; -1]], model, {a, b}, f];
fitTB[[n]] =
 FindFit[PowerSpectrumTB[[n, 10 ;; -1]], model, {a, b}, f];
fitSUM[[n]] =
```

```
   FindFit[PowerSpectrumSUM[[n, 10 ;; -1]], model, {a, b}, f];
  plotPower[[
    n]] = {Show[
     ListLogLogPlot[PowerSpectrumLR[[n]], PlotStyle -> Black,
      ImageSize -> Medium,
      PlotLabel ->
       Row[{Rasterize["L-R   A="], Rasterize[a /. fitLR[[n]]],
         Rasterize["   f0=" <> ToString[b /. fitLR[[n]]] <> " Hz"]}],
      PlotRange -> All, AxesLabel -> {"f/Hz", "\[Mu]m/Hz"}],
     LogLogPlot[model /. fitLR[[n]], {f, 0.01, length/10},
      PlotRange -> All]],
    Show[ListLogLogPlot[PowerSpectrumTB[[n]], PlotStyle -> Black,
      ImageSize -> Medium,
      PlotLabel ->
       Row[{Rasterize["L-R   A="], Rasterize[a /. fitTB[[n]]],
         Rasterize["   f0=" <> ToString[b /. fitTB[[n]]] <> " Hz"]}],
      PlotRange -> All, AxesLabel -> {"f/Hz", "\[Mu]m/Hz"}],
     LogLogPlot[model /. fitTB[[n]], {f, 0.01, length/5},
      PlotRange -> All]],
    Show[ListLogLogPlot[PowerSpectrumSUM[[n]], PlotStyle -> Black,
      ImageSize -> Medium,
      PlotLabel ->
       Row[{Rasterize["L-R   A="], Rasterize[a /. fitSUM[[n]]],
         Rasterize[
          "   f0=" <> ToString[b /. fitSUM[[n]]] <> " Hz" <>
           dataFiles[[n]]]}], PlotRange -> All,
      AxesLabel -> {"f/Hz", "\[Mu]m/Hz"}],
     LogLogPlot[model /. fitSUM[[n]], {f, 0.01, length/2},
      PlotRange -> All]]}];
Export[ToString[number] <> " plot.png",
  Column[Table[{plotDisp[[m]], plotPower[[m]]} // Grid, {m, 1,
     Length[dataFiles]}], Dividers -> All]];
```

Then the power spectrum density is plotted and the .png images exported.

```
powerOverlayLR =
  ListLogLogPlot[
   Table[PowerSpectrumLR[[i]], {i, 1, Length[dataFiles]}],
   ImageSize -> 1000,
   PlotLegends ->
    SwatchLegend@
     Table["f0=" <> ToString[b /. fitLR[[i]]] <> " Hz", {i, 1,
       Length[dataFiles]}], PlotRange -> All,
   AxesLabel -> {"f/Hz", "a.u."}];
powerOverlayTB =
  ListLogLogPlot[
```

```
   Table[PowerSpectrumTB[[i]], {i, 1, Length[dataFiles]}],
   ImageSize -> 1000,
   PlotLegends ->
    SwatchLegend@
     Table["f0=" <> ToString[b /. fitLR[[i]]] <> " Hz", {i, 1,
       Length[dataFiles]}], PlotRange -> All,
   AxesLabel -> {"f/Hz", "a.u."}];
Export[ToString[number] <> " Power Overlay.png",
  Column[{powerOverlayLR, powerOverlayTB}]];
```

Below is a plot of stiffness *vs* laser power with both the power spectrum method and the equipartition method.

```
power = {118.47, 117.65, 109.19, 97.189, 78.158, 57.14, 36.205,
   18.362, 7.701};
(*Below: power spectrum method in horizontal axis*)
points = Transpose[{power, 10^-7 10^6 fitLR[[All, 2, 2]]}];
points = Abs /@ points;
fitx = FindFit[points, a x + b, {a, b}, x];
points = Transpose[{points, ErrorBar /@ powerH[[1 ;; -2]]}];
f0PowerHorizontal =
  Show[ErrorListPlot[points,
    AxesLabel -> {"Power (mW)",
      "\!\(\*SubscriptBox[\(k\), \
\(x\)]\)(pN\[CenterDot]\!\(\*SuperscriptBox[\(\[Micro]m\), \
\(-1\)]\))"}, AxesStyle -> {Thick, Black},
    LabelStyle -> Directive[40, Black],
    PlotStyle -> Directive[PointSize[0.02], Black],
    PlotRange -> {{0, 120}, Automatic}, ImageSize -> 1000],
   Plot[(a x + b) /. fitx, {x, 5, 120}, PlotStyle -> Black]];
(*Below: power spectrum method in vertical axis*)
points = Transpose[{power, 1.58 10^-7 10^6 fitTB[[All, 2, 2]]}];
points = Abs /@ points;
fity = FindFit[points, a y + b, {a, b}, y];
points = Transpose[{points, ErrorBar /@ powerV[[1 ;; -2]]}];
f0PowerVertical =
  Show[ErrorListPlot[points,
    AxesLabel -> {"Power (mW)",
      "\!\(\*SubscriptBox[\(k\), \
\(y\)]\)(pN\[CenterDot]\!\(\*SuperscriptBox[\(\[Micro]m\), \
\(-1\)]\))"}, AxesStyle -> {Thick, Black},
    LabelStyle -> Directive[40, Black],
    PlotStyle -> Directive[PointSize[0.02], Black],
    PlotRange -> {{0, 120}, Automatic}, ImageSize -> 1000],
   Plot[(a y + b) /. fity, {y, 5, 120}, PlotStyle -> Black]];
fitx = FindFit[Transpose[{power, 10^6 kxEquipartition}],
```

```
   a x + b, {a, b}, x];
fity = FindFit[Transpose[{power, 10^6 kyEquipartition}],
   a y + b, {a, b}, y];
(*Below: equipartition plot in horizontal axis*)
points = Transpose[{power, 10^6 kxEquipartition}];
points = Transpose[{points, ErrorBar /@ equiH[[1 ;; -2]]}];
f0EquiHorizontal =
  Show[ErrorListPlot[points,
    AxesLabel -> {"Power (mW)",
      "\!\(\*SubscriptBox[\(k\), \
\(x\)]\)(pN\[CenterDot]\!\(\*SuperscriptBox[\(\[Micro]m\), \
\(-1\)]\))"}, AxesStyle -> {Thick, Black},
    LabelStyle -> Directive[40, Black],
    PlotRange -> {{0, 120}, Automatic},
    PlotStyle -> Directive[PointSize[0.02], Black], ImageSize -> 1000],
   Plot[(a x + b) /. fitx, {x, 5, 120}, PlotStyle -> Black]];
(*Below: equipartition plot in vertical axis*)
points = Transpose[{power, 10^6 kyEquipartition}];
points = Transpose[{points, ErrorBar /@ equiV[[1 ;; -2]]}];
f0EquiVertical =
  Show[ErrorListPlot[points,
    AxesLabel -> {"Power (mW)",
      "\!\(\*SubscriptBox[\(k\), \
\(y\)]\)(pN\[CenterDot]\!\(\*SuperscriptBox[\(\[Micro]m\), \
\(-1\)]\))"}, AxesStyle -> {Thick, Black},
    LabelStyle -> Directive[40, Black],
    PlotRange -> {{0, 120}, Automatic},
    PlotStyle -> Directive[PointSize[0.02], Black], ImageSize -> 1000],
   Plot[(a y + b) /. fity, {y, 5, 120}, PlotStyle -> Black]];
Export[ToString[number] <> " corner frequency vs power.png",
  Row[{f0EquiHorizontal, f0EquiVertical, f0PowerHorizontal,
    f0PowerVertical}, ImageSize -> 4001]];
```

A.2 LabVIEW control for the magnetic tweezers

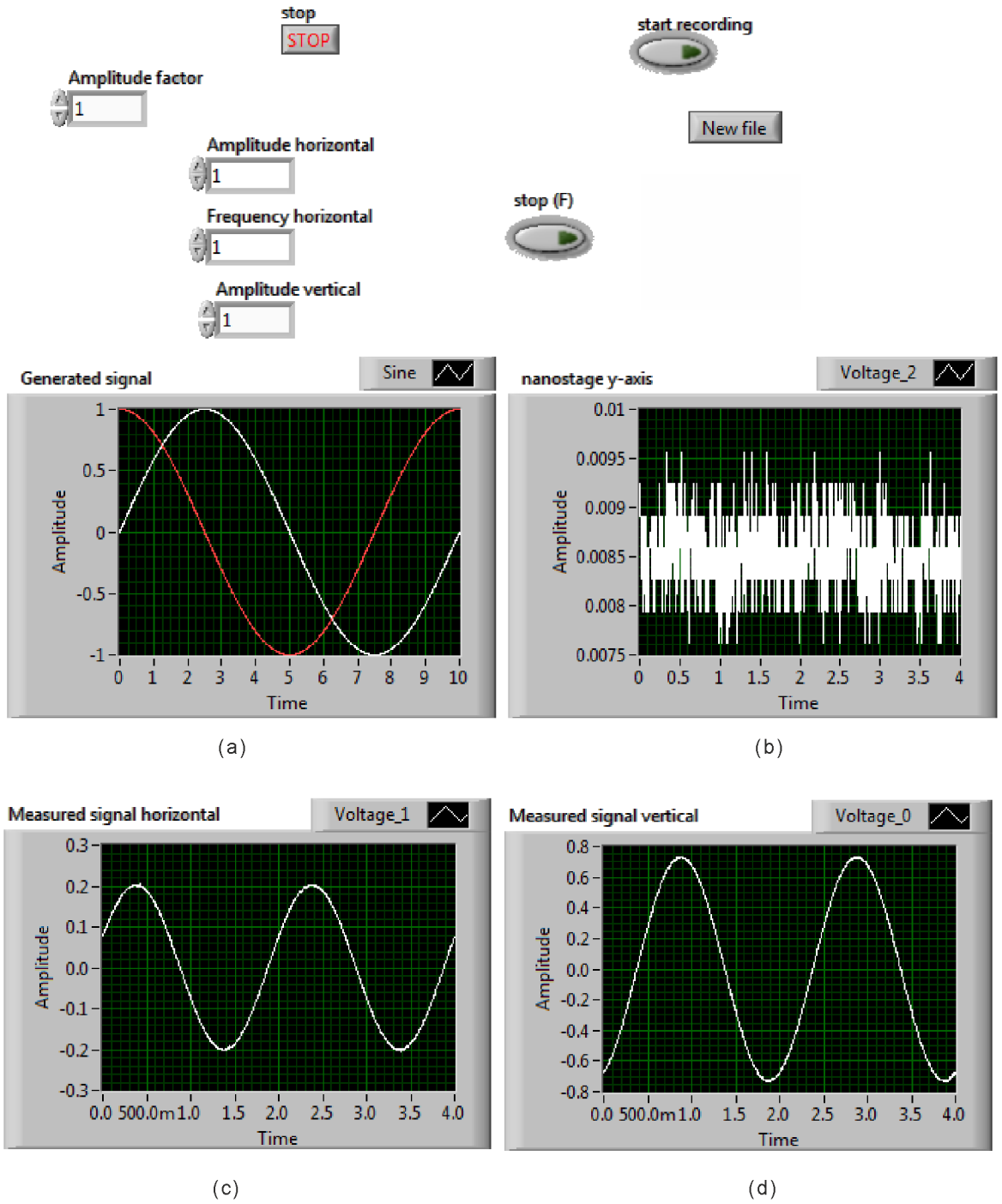

Figure A.1: Magnetic tweezers code - the front panel. The user-specifiable values are the amplitudes and frequency but this can be greatly generalised to include a much more flexibility. (a) The generated signal in x- and y-axis. (b) The nanostage signal is shown here to save screen space but really is irrelevant to the magnetic tweezers control. (c) Measured voltage in the smaller pair of coils. (d) Measured voltage in the larger pair of coils.

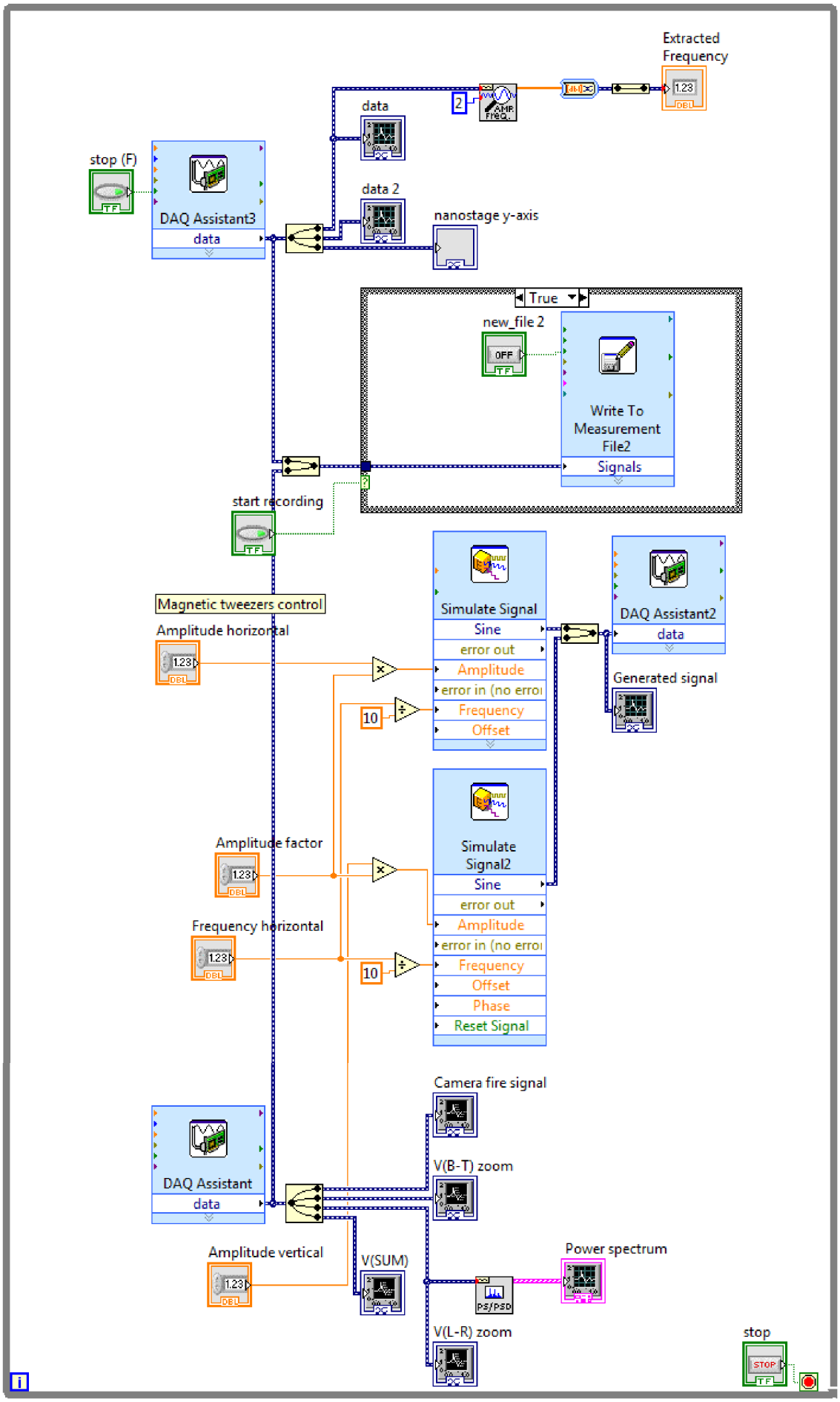

Figure A.2: Magnetic tweezers code - the block diagram.

A.3 LabVIEW control for the nanostage

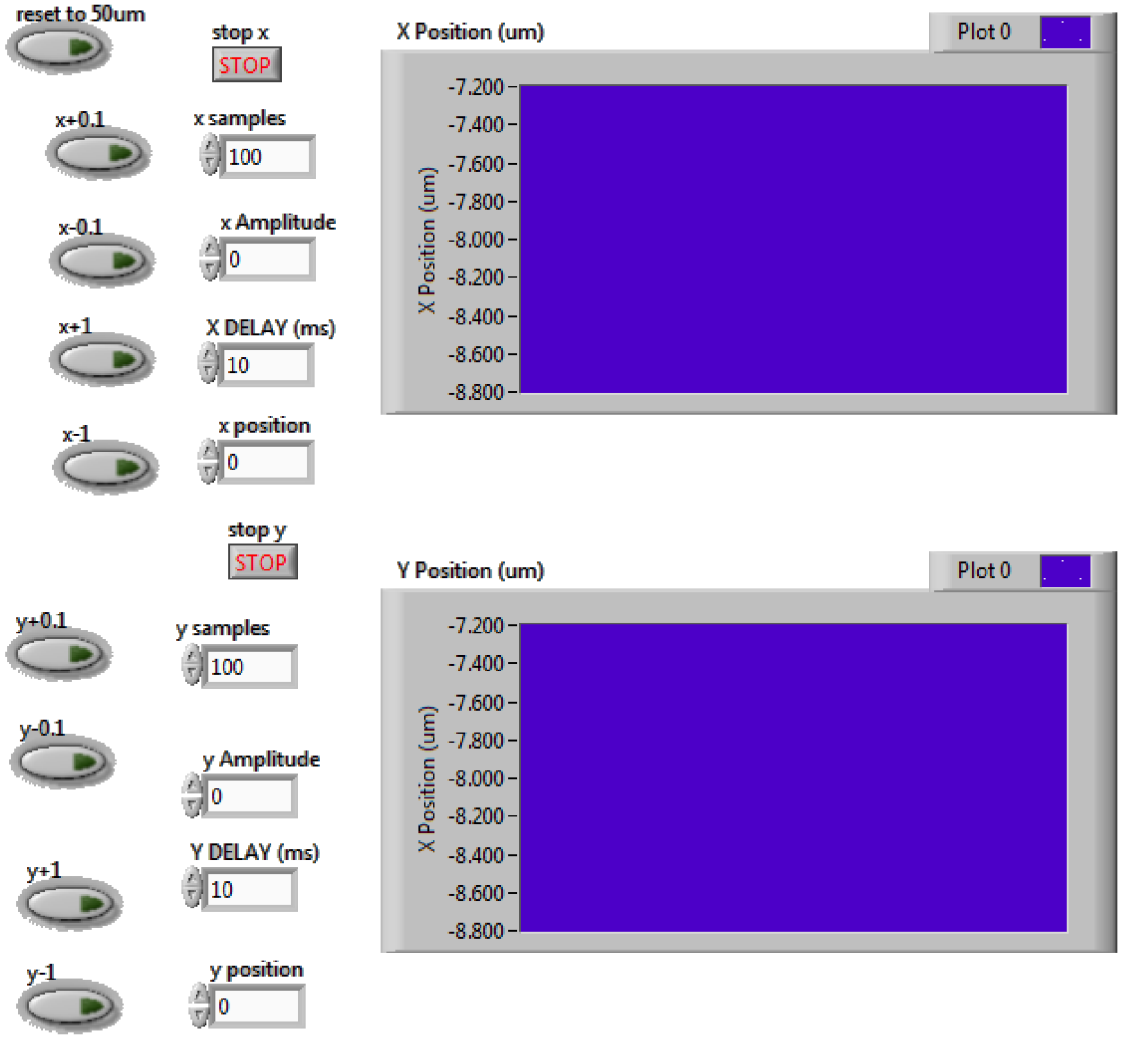

Figure A.3: Nanostage code - the front panel. In this instance the user can press any of the $x + \Delta x$ buttons to move the stage in $\Delta x\,\mu\mathrm{m}$ - this is the same for the y-axis. Again, this can be greatly generalised to include a much more flexibility.

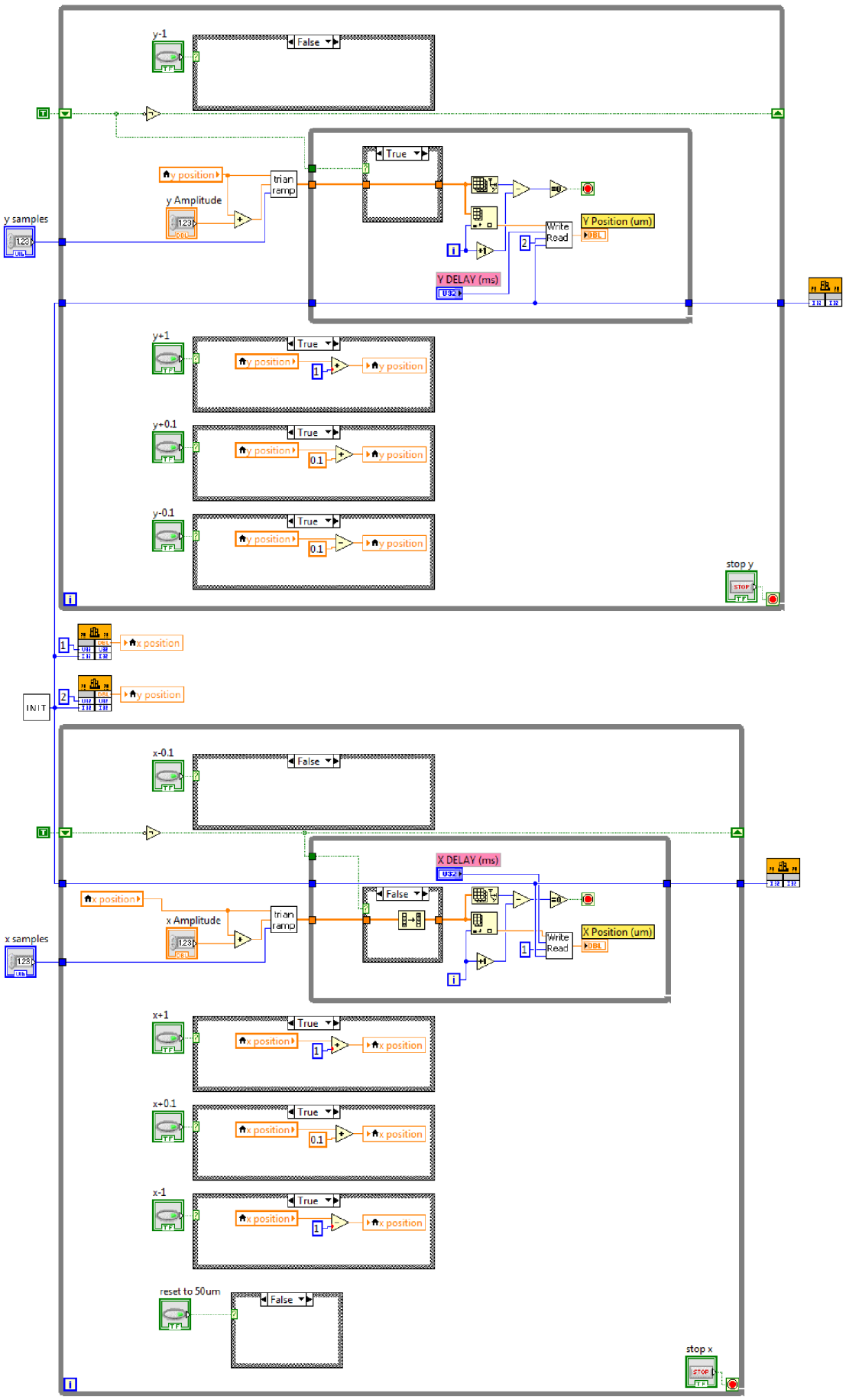

Figure A.4: Magnetic tweezers code - the block diagram.

A.4 Blinking behaviour modelling

The blinking behaviour is modelled using the code below. The video from this modelling is compared with the videos taken from experiments. The two videos match each others' behaviour.

Assumptions: 1. Fluorophores don't bind/unbind to the DNA during the movie - at all times, a dye is either on DNA or in liquid. 2. Binding positions on the DNA and in liquid are independent, random and have uniform distribution (with different probability for on DNA and in liquid). 3. Dyes in liquid undergo Brownian motion. 4. The time that a dye flash lasts also is independent, random and has uniform distribution. 5. Dyes recover from dark state with probability of 66.7%. The rest irreversibly bleach. 6. Pixel size is 120 nm by 120 nm. 7. DNA and dye concentration are kept to experimental values: 0.159nM (DNA) and 10uM (Yoyo), 50uM (Syto). However, only one DNA is displayed.

```
(*DNA length in 160nm*)
l = 100.;
(*standard deviation of laser spot at focal plane in 160nm*)

R = 100.;
(*standard deviation of dye flash spot in 160nm*)
r = 1.;
(*FWHM of laser spot in 160nm*)
FWHM = 2 Sqrt[2 Log[2]] R;
(*FWHM of dye flash spot in 160nm*)
fwhm = 2 Sqrt[2 Log[2]] r;
(*Total pixel number*)
nPixel = 512 512;
(*Proportion of dye in liquid*)
p = 0.001;
(*Number of dye on DNA, assuming 1 dye per ~100bp*)
nDyeDNA = 12000;
(*Total dye number in flow chamber. This is assuming 5\[Mu]l 10\[Mu]M \
dye.*)
nDye = 3 10^13;
(*The amount of time a dye molecule flash lasts in second. Assume \
\[Tau]Bright is constant.*)
\[Tau]Bright = 40. 10^-3;
(*The mean time a dye molecule dark state lasts in second. Assume \
\[Tau]Dark follows exponential decay.*)
\[Tau]Dark = 280. 10^-3;
(*Frame rate in Hz*)
FrameRate = 20.;
(*Movie length in second*)
\[Tau]Movie = 20.;
(*Frame length in second*)
\[Tau]Frame = 1/FrameRate;
```

```
(*Exposure time in second*)
\[Tau]Exposure = 40. 10^-3;
(*Neutral density filter*)
ND = 2.;
(*Probability of irreversible bleaching*)
pBleach = 0.33;
(*If there is noise*)
ElectronicNoise = "Present";
Autofluoresecence = "Absent";
PSFNoise = "Absent";
Export["Z:\\shared\\Data\\Simulation\\DoNotReadme.xlsx", {l, R, r,
   FWHM, fwhm, nPixel, p, nDyeDNA, nDye, \[Tau]Bright, \[Tau]Dark,
   FrameRate, \[Tau]Movie, \[Tau]Frame, \[Tau]Exposure, ND, pBleach,
   ElectronicNoise, Autofluoresecence, PSFNoise}];

(*The number of times the dyes on DNA goes into dark state before \
irreversally bleaching.*)

flashes =
  RandomChoice[1/3 Table[(2/3)^i, {i, 0, 29}] -> Range[0, 29],
   nDyeDNA];
(*Lengths of dark states for all dark states of each dye*)

timeDark = Table[Null, {nDyeDNA}];
Table[timeDark[[i]] =
   RandomVariate[
    MixtureDistribution[{50,
      1}, {ExponentialDistribution[1/\[Tau]Dark],
      TriangularDistribution[{0, 20}, 0]}], flashes[[i]]], {i, 1,
   nDyeDNA}];
(*Durations of alternating bright and dark states of each dye*)
\
lengths = Table[Null, {nDyeDNA}]; i = 1;
While[i <= nDyeDNA,
  lengths[[i]] = {\[Tau]Bright};
  If[timeDark[[i]] == {}, Null,
   Table[lengths[[i]] =
     Join[lengths[[i]], {timeDark[[i, j]], \[Tau]Bright}], {j, 1,
     Length[timeDark[[i]]]}]];
  lengths[[i]] = Accumulate[lengths[[i]]];
  i++];
ClearAll[i];
(*On/off of dyes as a function of time*)
states =
 Table[Null, {nDyeDNA}]; i = 1;
While[i <= nDyeDNA,
```

```
  piece = {{1, 0 <= t <= lengths[[i, 1]]}};
  Table[
   piece =
    Append[piece, {0, lengths[[i, j]] < t <= lengths[[i, j + 1]]}];
   piece =
    Append[piece, {1,
      lengths[[i, j + 1]] < t <= lengths[[i, j + 2]]}];,
   {j, 1, Length[lengths[[i]]] - 2, 2}];
  states[[i]] = Piecewise[piece];
  i++];
ClearAll[i];
(*Exposure of camera as a function of time*)

exposure = {{1, 0 <= t <= \[Tau]Exposure}};
Table[
  exposure =
   Append[exposure, {0,
     1/FrameRate i + \[Tau]Exposure < t <= 1/FrameRate (i + 1)}];
  exposure =
   Append[exposure, {1,
     1/FrameRate (i + 1) < t <=
      1/FrameRate (i + 1) + \[Tau]Exposure}];,
  {i, 0, FrameRate (\[Tau]Movie - \[Tau]Exposure)}];
exposure = Piecewise[exposure];
(*Multiply on/off function and exposure function together to get a \
function for effective on/off states*)

EffectiveStates = states exposure;
EffectiveStates = Simplify[EffectiveStates];
Table[EffectiveStates[[i]] =
   List @@ EffectiveStates[[i, 1, 1, 2]], {i, 1, nDyeDNA}];
Table[EffectiveStates[[i]] =
   Apply[List, #] & /@ EffectiveStates[[i]], {i, 1, nDyeDNA}];
Table[EffectiveStates[[i]] = Flatten@EffectiveStates[[i]], {i, 1,
   nDyeDNA}];
Table[EffectiveStates[[i]] = DeleteCases[EffectiveStates[[i]], t], {i,
    1, nDyeDNA}];
Table[EffectiveStates[[i]] =
   DeleteCases[EffectiveStates[[i]], LessEqual], {i, 1, nDyeDNA}];
Table[EffectiveStates[[i]] =
   DeleteCases[EffectiveStates[[i]], Less], {i, 1, nDyeDNA}];

   (*Initialise the matrix to house signal duration information for each \
pixel and each frame*)

ESPerFrame = Table[0, {nDyeDNA}, {\[Tau]Movie FrameRate}];
```

```
(*Finialise the matrix by filling in  signal duration information for \
each pixel and each frame*)
i = 1;
While[i <= nDyeDNA,
 (*Give EffectiveStates[[i]] a short name to save space*)

 ES = EffectiveStates[[i]];
 (*Take values in odd numbered positions - they are the time points \
for signal starts*)
 Start = Table[ES[[j]], {j, 1, Length[ES], 2}];
 (*Calculate the position of each signal in term of frame number, and \
the number of signals in a given frame*)

 temp = Transpose[Tally[Floor[Start, \[Tau]Frame]]];
 fNumber = temp[[1]]/\[Tau]Frame + 1;
 fNumber = fNumber /. (401. -> 400.);
 nSignal = temp[[2]];
 (*Put signal duration in each pixel in each frame into ESPerFrame*)

 duration = Table[ES[[i + 1]] - ES[[i]], {i, 1, Length[ES], 2}];
 acc = Accumulate[nSignal];
 ESPerFrame[[i, fNumber[[1]]]] = Total[Take[duration, acc[[1]]]];
 j = 2;
 While[j <= Length[acc],
  ESPerFrame[[i, fNumber[[j]]]] =
   Total[Take[duration, {acc[[j - 1]] + 1, acc[[j]]}]]; j++]; i++;]
ESPerFrame = Transpose[ESPerFrame];

Export["Z:\\shared\\Data\\Simulation\\data6.txt", {Join[{"Dark"},
    Flatten[timeDark]],
   DeleteCases[Join[{"Flash"}, Flatten[ESPerFrame]], 0]}];

(*Dye positions on DNA, assuming one position can maximally have one \
dye*)
positions = Table[206 + x, {x, 0, 100, 0.34/160}];
positions = RandomSample[positions, nDyeDNA];
(*Establish analytical expression of focal plane intensity profile:*)

LaserSpot[x_, y_] := Exp[-(((x - 256)^2 + (y - 256)^2)/(2 R^2))];
DyeSpot = Table[0, {\[Tau]Movie FrameRate}, {nDyeDNA}];
Table[Table[
   DyeSpot[[k, i]] =
    ESPerFrame[[k,
      i]] Exp[-(((x - positions[[i]])^2 + (y - 256)^2)/(2 r^2))], {i,
    1, nDyeDNA}], {k, 1, \[Tau]Movie FrameRate}];
DyeSpot = Total /@ DyeSpot;
```

```
width = 120; height = 6;
DyeIntensity = Table[0, {\[Tau]Movie FrameRate}];
Monitor[Table[
   DyeIntensity[[k]] =
    Module[{frame, i = 257 - height/2, j = 257 - width/2},
     frame =
      Table[0, {\[Tau]Movie FrameRate}, {512}, {512}];(*Initialise \
512 by 512 pixel frames*)
     While[i < 257 + height/2,
      While[j < 257 + width/2, x = j - 0.5; y = 512.5 - i;
       frame[[k, i, j]] = DyeSpot[[k]]; j++];
      i++; j = 257 - width/2;];
     frame[[k, 257 - height ;; 256 + height,
      257 - width ;; 256 + width]]
     ], {k, 1, \[Tau]Movie FrameRate}];, k]
Save["Z:\\shared\\Data\\Simulation\\FinalData6.txt", DyeIntensity]

(*Add in noise and generate movie*)

noise = Abs@
   RandomVariate[
    NormalDistribution[0.005, 0.001], {\[Tau]Movie FrameRate, 2 height,
     2 width}];
DyeIntensity = DyeIntensity + noise;
data = Table[
   Image[DyeIntensity[[i]]/Max[DyeIntensity[[1]]]], {i,
    1, \[Tau]Movie FrameRate}];
Export["Z:\\shared\\Data\\Simulation\\movie6.tif", data];
```

List of acronyms

AFM	Atomic force microscopy
AOD	Acousto-optical deflector
AT	Acoustic tweezers
ATP	Adenosine triphosphate
BALM	Binding activated localisation microscopy
BaLM	Bleaching/binding assisted localisation microscopy
BFP	Back focal plane
BSA	Bovine serum albumin
DNA	Deoxyribonucleic acid
EMCCD	Electron multiplying charge-coupled device
FLIP	Fluorescence loss in photobleaching
FRAP	Fluorescence recovery after photobleaching
FRET	Forster resonance energy transfer
HOT	Holographic optical tweezers
LG	Laguerre-Gaussian
MT	Magnetic tweezers
NA	Numerical aperture
NIR	Near infrared
OT	Optical tweezers
PALM	Photoactivated localisation microscopy
PCR	Polymerase chain reaction
PSD	Power spectral density
PSF	Point spread function
QPD	Quadrant photodiode
RNA	Ribonucleic acid
sd	Standard deviation
SLM	Spatial light modulator
SNR	Single-to-noise ratio
SSIM	Saturated structured illumination microscopy
STED	Stimulated emission depletion
STORM	Stochastic optical reconstruction microscopy
TIRF	Total internal reflection fluorescence

Bibliography

[1] MS Smyth and JHJ Martin. x ray crystallography. *Journal of Clinical Pathology*, 53(1):8, 2000.

[2] R Shulman. *Biological applications of magnetic resonance*. Elsevier, 2012.

[3] RM Simmonst, JT Finer, HM Warrick, B Kralik, S Chu, and JA Spudich. Force on single actin filaments in a motility assay measured with an optical trap. In *Mechanism of Myofilament Sliding in Muscle Contraction*, pages 331–337. Springer, 1993.

[4] Steven M Block, Bruce J Schnapp, and Lawrence SB Goldstein. Bead movement by single kinesin molecules studied with optical tweezers. *Nature*, 348(6299):348, 1990.

[5] Karel Svoboda and Steven M Block. Force and velocity measured for single kinesin molecules. *Cell*, 77(5):773–784, 1994.

[6] Jan Lipfert, Daniel A Koster, Igor D Vilfan, Susanne Hage, and Nynke H Dekker. Single-molecule magnetic tweezers studies of type ib topoisomerases. *DNA Topoisomerases: Methods and Protocols*, pages 71–89, 2009.

[7] G Charvin, TR Strick, D Bensimon, and V Croquette. Tracking topoisomerase activity at the single-molecule level. *Annu. Rev. Biophys. Biomol. Struct.*, 34:201–219, 2005.

[8] Hiroyasu Itoh, Akira Takahashi, Kengo Adachi, Hiroyuki Noji, Ryohei Yasuda, Masasuke Yoshida, and Kazuhiko Kinosita. Mechanically driven atp synthesis by f1-atpase. *Nature*, 427(6973):465–468, 2004.

[9] Joshua W Shaevitz, Elio A Abbondanzieri, Robert Landick, and Steven M Block. Backtracking by single rna polymerase molecules observed at near-base-pair resolution. *Nature*, 426(6967):684–687, 2003.

[10] Elio A Abbondanzieri, William J Greenleaf, Joshua W Shaevitz, Robert Landick, and Steven M Block. Direct observation of base-pair stepping by rna polymerase. *Nature*, 438(7067):460–465, 2005.

[11] Gijs JL Wuite, Steven B Smith, Mark Young, David Keller, and Carlos Bustamante. Single-molecule studies of the effect of template tension on t7 dna polymerase activity. *Nature*, 404(6773):103–106, 2000.

[12] Steven B Smith, Laura Finzi, and Carlos Bustamante. Direct mechanical measurements of the elasticity of single dna molecules by using magnetic beads. *Science*, 258(5085):1122–1126, 1992.

[13] Steven B Smith, Yujia Cui, and Carlos Bustamente. Overstretching b-dna: the elastic response of individual double-stranded and single-stranded dna molecules. *Science*, 271(5250):795, 1996.

[14] Graeme A King, Peter Gross, Ulrich Bockelmann, Mauro Modesti, Gijs JL Wuite, and Erwin JG Peterman. Revealing the competition between peeled ssdna, melting bubbles, and s-dna during dna overstretching using fluorescence microscopy. *Proceedings of the National Academy of Sciences*, 110(10):3859–3864, 2013.

[15] Xinghua Zhang, Hu Chen, Shimin Le, Ioulia Rouzina, Patrick S Doyle, and Jie Yan. Revealing the competition between peeled ssdna, melting bubbles, and s-dna during dna overstretching by single-molecule calorimetry. *Proceedings of the National Academy of Sciences*, 110(10):3865–3870, 2013.

[16] TR Strick, JF Allemand, D Bensimon, A Bensimon, and V Croquette. The elasticity of a single supercoiled dna molecule. *Science*, 271(5257):1835, 1996.

[17] Aurélien Crut, Daniel A Koster, Ralf Seidel, Chris H Wiggins, and Nynke H Dekker. Fast dynamics of supercoiled dna revealed by single-molecule experiments. *Proceedings of the National Academy of Sciences*, 104(29):11957–11962, 2007.

[18] JF Leger, G Romano, A Sarkar, J Robert, L Bourdieu, D Chatenay, and JF Marko. Structural transitions of a twisted and stretched dna molecule. *Physical review letters*, 83(5):1066, 1999.

[19] Jean-Francois Leger, Jerome Robert, Laurent Bourdieu, Didier Chatenay, and John F Marko. Reca binding to a single double-stranded dna molecule: a possible role of dna conformational fluctuations. *Proceedings of the National Academy of Sciences*, 95(21):12295–12299, 1998.

[20] G Zuccheri, R Th Dame, M Aquila, I Muzzalupo, and B Samori. Conformational fluctuations of supercoiled dna molecules observed in real time with a scanning force microscope. *Applied Physics A: Materials Science & Processing*, 66:S585–S589, 1998.

[21] Iddo Heller, Tjalle P Hoekstra, Graeme A King, Erwin JG Peterman, and Gijs JL Wuite. Optical tweezers analysis of dna–protein complexes. *Chemical reviews*, 114(6):3087–3119, 2014.

[22] Martin L Bennink, Sanford H Leuba, Gregory H Leno, Jordanka Zlatanova, Bart G de Grooth, and Jan Greve. Unfolding individual nucleosomes by stretching single chromatin fibers with optical tweezers. *Nature Structural & Molecular Biology*, 8(7):606–610, 2001.

[23] Gregory J Gemmen, Ronald Sim, Karl A Haushalter, Pu Chun Ke, James T Kadonaga, and Douglas E Smith. Forced unraveling of nucleosomes assembled on heterogeneous dna using core histones, nap-1, and acf. *Journal of molecular biology*, 351(1):89–99, 2005.

[24] Remus T Dame, Maarten C Noom, and Gijs JL Wuite. Bacterial chromatin organization by h-ns protein unravelled using dual dna manipulation. *Nature*, 444(7117):387–390, 2006.

[25] Sophie Dumont, Wei Cheng, Victor Serebrov, Rudolf K Beran, Ignacio Tinoco, Anna Marie Pyle, and Carlos Bustamante. Rna translocation and unwinding mechanism of hcv ns3 helicase and its coordination by atp. *Nature*, 439(7072):105–108, 2006.

[26] Daniel S Johnson, Lu Bai, Benjamin Y Smith, Smita S Patel, and Michelle D Wang. Single-molecule studies reveal dynamics of dna unwinding by the ring-shaped t7 helicase. *Cell*, 129(7):1299–1309, 2007.

[27] EA Ash and G Nicholls. Super-resolution aperture scanning microscope. 1972.

[28] E Betzig, M Isaacson, and A Lewis. Collection mode near-field scanning optical microscopy. *Applied physics letters*, 51(25):2088–2090, 1987.

[29] Stefan W Hell and Jan Wichmann. Breaking the diffraction resolution limit by stimulated emission: stimulated-emission-depletion fluorescence microscopy. *Optics letters*, 19(11):780–782, 1994.

[30] Thomas A Klar and Stefan W Hell. Subdiffraction resolution in far-field fluorescence microscopy. *Optics letters*, 24(14):954–956, 1999.

[31] Volker Westphal and Stefan W Hell. Nanoscale resolution in the focal plane of an optical microscope. *Physical review letters*, 94(14):143903, 2005.

[32] Gerald Donnert, Jan Keller, Rebecca Medda, M Alexandra Andrei, Silvio O Rizzoli, Reinhard Lührmann, Reinhard Jahn, Christian Eggeling, and Stefan W Hell. Macromolecular-scale resolution in biological fluorescence microscopy. *Proceedings of the National Academy of Sciences*, 103(31):11440–11445, 2006.

[33] Katrin I Willig, Robert Kellner, Rebecca Medda, Birka Hein, Stefan Jakobs, and Stefan W Hell. Nanoscale resolution in gfp-based microscopy. *Nature Methods*, 3(9):721–723, 2006.

[34] Stefan W Hell, Marcus Dyba, and Stefan Jakobs. Concepts for nanoscale resolution in fluorescence microscopy. *Current opinion in neurobiology*, 14(5):599–609, 2004.

[35] Michael Hofmann, Christian Eggeling, Stefan Jakobs, and Stefan W Hell. Breaking the diffraction barrier in fluorescence microscopy at low light intensities by using reversibly photoswitchable proteins. *Proceedings of the National Academy of Sciences of the United States of America*, 102(49):17565–17569, 2005.

[36] Mats GL Gustafsson. Nonlinear structured-illumination microscopy: wide-field fluorescence imaging with theoretically unlimited resolution. *Proceedings of the National Academy of Sciences of the United States of America*, 102(37):13081–13086, 2005.

[37] Michael J Rust, Mark Bates, and Xiaowei Zhuang. Sub-diffraction-limit imaging by stochastic optical reconstruction microscopy (storm). *Nature methods*, 3(10):793–796, 2006.

[38] Eric Betzig, George H Patterson, Rachid Sougrat, O Wolf Lindwasser, Scott Olenych, Juan S Bonifacino, Michael W Davidson, Jennifer Lippincott-Schwartz, and Harald F

Hess. Imaging intracellular fluorescent proteins at nanometer resolution. *Science*, 313(5793):1642–1645, 2006.

[39] Samuel T Hess, Thanu PK Girirajan, and Michael D Mason. Ultra-high resolution imaging by fluorescence photoactivation localization microscopy. *Biophysical journal*, 91(11):4258–4272, 2006.

[40] Ingmar SCHOEN, Jonas RIES, Enrico KLOTZSCH, Helge EWERS, and Viola VOGEL. Binding-activated localization microscopy of dna structures. *Nano letters*, 11(9):4008–4011, 2011.

[41] Dylan T Burnette, Prabuddha Sengupta, Yuhai Dai, Jennifer Lippincott-Schwartz, and Bechara Kachar. Bleaching/blinking assisted localization microscopy for superresolution imaging using standard fluorescent molecules. *Proceedings of the National Academy of Sciences*, 108(52):21081–21086, 2011.

[42] Lubert Stryer and Richard P Haugland. Energy transfer: a spectroscopic ruler. *Proceedings of the National Academy of Sciences*, 58(2):719–726, 1967.

[43] M Edidin, Y Zagyansky, and TJ Lardner. Measurement of membrane protein lateral diffusion in single cells. *Science*, 191(4226):466–468, 1976.

[44] Daniel Axelrod, Peter Ravdin, DE Koppel, J Schlessinger, WW Webb, EL Elson, and TR Podleski. Lateral motion of fluorescently labeled acetylcholine receptors in membranes of developing muscle fibers. *Proceedings of the National Academy of Sciences*, 73(12):4594–4598, 1976.

[45] Nelson b Cole, Carolyn L Smith, Noah Sciaky, Mark Terasaki, et al. Diffusional mobility of golgi proteins in membranes of living cells. *Science*, 273(5276):797, 1996.

[46] Marijn TJ van Loenhout, MV de Grunt, and Cees Dekker. Dynamics of dna supercoils. *Science*, 338(6103):94–97, 2012.

[47] R Bruce Wallace, J Shaffer, RF Murphy, J Bonner, T Hirose, and K Itakura. Hybridization of synthetic oligodeoxyribonucleotides to ϕx 174 dna: the effect of single base pair mismatch. *Nucleic acids research*, 6(11):3543–3558, 1979.

[48] Richard E Dickerson. Crystal structure analysis of a complete turn of b-dna. *Nature*, 287:755–758, 1980.

[49] Friedrich Otto. Dapi staining of fixed cells for high-resolution flow cytometry of nuclear dna. *Methods in cell biology*, 33:105–110, 1990.

[50] AI Dragan, R Pavlovic, JB McGivney, JR Casas-Finet, ES Bishop, RJ Strouse, MA Schenerman, and CD Geddes. Sybr green i: fluorescence properties and interaction with dna. *Journal of fluorescence*, 22(4):1189–1199, 2012.

[51] Sophia Y Breusegem, Frank G Loontiens, Peter Regenfuss, and Robert M Clegg. Kinetics of binding of hoechst dyes to dna studied by stopped-flow fluorescence techniques. *Methods in enzymology*, 340:212–233, 2001.

[52] Seog K Kim and Bengt Nordén. Methyl green: a dna major-groove binding drug. *FEBS letters*, 315(1):61–64, 1993.

[53] Marc van Dijk and Alexandre MJJ Bonvin. 3d-dart: a dna structure modelling server. *Nucleic acids research*, 37(suppl 2):W235–W239, 2009.

[54] Walter Fiers and Robert L Sinsheimer. The structure of the dna of bacteriophage φx174: Iii. ultracentrifugal evidence for a ring structure. *Journal of molecular biology*, 5(4):424–434, 1962.

[55] John Cairns. The chromosome of escherichia coli. In *Cold Spring Harbor Symposia on Quantitative Biology*, volume 28, pages 43–46. Cold Spring Harbor Laboratory Press, 1963.

[56] Rossitza N Irobalieva, Jonathan M Fogg, Daniel J Catanese Jr, Thana Sutthibutpong, Muyuan Chen, Anna K Barker, Steven J Ludtke, Sarah A Harris, Michael F Schmid, Wah Chiu, et al. Structural diversity of supercoiled dna. *Nature communications*, 6, 2015.

[57] Carlos Bustamante, John F Marko, Eric D Siggia, S Smith, et al. Entropic elasticity of lambda-phage dna. *SCIENCE-NEW YORK THEN WASHINGTON-*, pages 1599–1599, 1994.

[58] John F Marko and Eric D Siggia. Stretching dna. *Macromolecules*, 28(26):8759–8770, 1995.

[59] Tongcang Li. Physical principle of optical tweezers. In *Fundamental Tests of Physics with Optically Trapped Microspheres*, pages 9–20. Springer, 2013.

[60] Simon Parkin, Gregor Knöner, Wolfgang Singer, Timo A Nieminen, Norman R Heckenberg, and Halina Rubinsztein-Dunlop. Optical torque on microscopic objects. *Methods in cell biology*, 82:525–561, 2007.

[61] Arthur La Porta and Michelle D Wang. Optical torque wrench: angular trapping, rotation, and torque detection of quartz microparticles. *Physical review letters*, 92(19):190801, 2004.

[62] Sergey S Shevkoplyas, Adam C Siegel, Robert M Westervelt, Mara G Prentiss, and George M Whitesides. The force acting on a superparamagnetic bead due to an applied magnetic field. *Lab on a Chip*, 7(10):1294–1302, 2007.

[63] Francesco Mosconi, Jean François Allemand, and Vincent Croquette. Soft magnetic tweezers: A proof of principle. *Review of scientific instruments*, 82(3):034302, 2011.

[64] Alexander D Rowe, Mark C Leake, Hywel Morgan, and Richard M Berry. Rapid rotation of micron and submicron dielectric particles measured using optical tweezers. *Journal of modern optics*, 50(10):1539–1554, 2003.

[65] TB Jones. Influence of scale on electrostatic forces and torques in ac particulate electrokinetics. In *IEE Proceedings-Nanobiotechnology*, volume 150, pages 39–46. IET, 2003.

[66] Philippe Cluzel, Anne Lebrun, Christoph Heller, Richard Lavery, Jean-Louis Viovy, Didier Chatenay, and François Caron. Dna: an extensible molecule. *Science*, pages 792–794, 1996.

[67] Sangjin Kim, Paul C Blainey, Charles M Schroeder, and X Sunney Xie. Multiplexed single-molecule assay for enzymatic activity on flow-stretched dna. *Nature methods*, 4(5):397–399, 2007.

[68] Gerd Binnig, Calvin F Quate, and Ch Gerber. Atomic force microscope. *Physical review letters*, 56(9):930, 1986.

[69] Gil U Lee, Linda A Chrisey, Richard J Colton, et al. Direct measurement of the forces between complementary strands of dna. *SCIENCE-NEW YORK THEN WASHINGTON-*, pages 771–771, 1994.

[70] Charles RP Courtney, Christine EM Demore, Hongxiao Wu, Alon Grinenko, Paul D Wilcox, Sandy Cochran, and Bruce W Drinkwater. Independent trapping and manipulation of microparticles using dexterous acoustic tweezers. *Applied Physics Letters*, 104(15):154103, 2014.

[71] Feng Guo, Zhangming Mao, Yuchao Chen, Zhiwei Xie, James P Lata, Peng Li, Liqiang Ren, Jiayang Liu, Jian Yang, Ming Dao, et al. Three-dimensional manipulation of single cells using surface acoustic waves. *Proceedings of the National Academy of Sciences*, 113(6):1522–1527, 2016.

[72] Ekaterina I Galanzha, Mark G Viegas, Taras I Malinsky, Alexander V Melerzanov, Mazen A Juratli, Mustafa Sarimollaoglu, Dmitry A Nedosekin, and Vladimir P Zharov. In vivo acoustic and photoacoustic focusing of circulating cells. *Scientific reports*, 6:21531, 2016.

[73] Kai Melde, Andrew G Mark, Tian Qiu, and Peer Fischer. Holograms for acoustics. *Nature*, 537(7621):518–522, 2016.

[74] Antoine Riaud, Michael Baudoin, Olivier Bou Matar, Loic Becerra, and Jean-Louis Thomas. Selective manipulation of microscopic particles with precursor swirling rayleigh waves. *Physical Review Applied*, 7(2):024007, 2017.

[75] Arthur Ashkin. Forces of a single-beam gradient laser trap on a dielectric sphere in the ray optics regime. *Biophysical journal*, 61(2):569–582, 1992.

[76] Timo A Nieminen, Vincent LY Loke, Alexander B Stilgoe, Gregor Knöner, Agata M Brańczyk, Norman R Heckenberg, and Halina Rubinsztein-Dunlop. Optical tweezers computational toolbox. *Journal of Optics A: Pure and Applied Optics*, 9(8):S196, 2007.

[77] Erwin JG Peterman, Frederick Gittes, and Christoph F Schmidt. Laser-induced heating in optical traps. *Biophysical journal*, 84(2):1308–1316, 2003.

[78] Les Allen, Marco W Beijersbergen, RJC Spreeuw, and JP Woerdman. Orbital angular momentum of light and the transformation of laguerre-gaussian laser modes. *Physical Review A*, 45(11):8185, 1992.

[79] S Sato, M Ishigure, and H Inaba. Optical trapping and rotational manipulation of microscopic particles and biological cells using higher-order mode nd: Yag laser beams. *Electronics letters*, 27(20):1831–1832, 1991.

[80] J1 Durnin, JJ Miceli Jr, and JH Eberly. Diffraction-free beams. *Physical review letters*, 58(15):1499, 1987.

[81] Grigorii S Sokolovskii, Vladislav V Dudelev, Sergey N Losev, KK Soboleva, Anton G Deryagin, VI Kuchinskii, W Sibbett, and EU Rafailov. Optical trapping with bessel beams generated from semiconductor lasers. In *Journal of Physics: Conference Series*, volume 572, page 012039. IOP Publishing, 2014.

[82] V Garces-Chavez, David McGloin, H Melville, Wilson Sibbett, and Kishan Dholakia. Simultaneous micromanipulation in multiple planes using a self-reconstructing light beam. *Nature*, 419(6903):145–147, 2002.

[83] Jun Chen, Jack Ng, Zhifang Lin, and CT Chan. Optical pulling force. *Nature photonics*, 5(9):531–534, 2011.

[84] Andrey Novitsky, Cheng-Wei Qiu, and Haifeng Wang. Single gradientless light beam drags particles as tractor beams. *Physical review letters*, 107(20):203601, 2011.

[85] Christopher Deufel, Scott Forth, Chad R Simmons, Siavash Dejgosha, and Michelle D Wang. Nanofabricated quartz cylinders for angular trapping: Dna supercoiling torque detection. *Nature methods*, 4(3):223–225, 2007.

[86] Jennifer E Curtis, Brian A Koss, and David G Grier. Dynamic holographic optical tweezers. *Optics communications*, 207(1):169–175, 2002.

[87] Brian J Roxworthy, Kaspar D Ko, Anil Kumar, Kin Hung Fung, Edmond KC Chow, Gang Logan Liu, Nicholas X Fang, and Kimani C Toussaint Jr. Application of plasmonic bowtie nanoantenna arrays for optical trapping, stacking, and sorting. *Nano letters*, 12(2):796–801, 2012.

[88] Pamela Korda, Gabriel C Spalding, Eric R Dufresne, and David G Grier. Nanofabrication with holographic optical tweezers. *Review of Scientific Instruments*, 73(4):1956–1957, 2002.

[89] Ritesh Agarwal, Kosta Ladavac, Yael Roichman, Guihua Yu, Charles M Lieber, and David G Grier. Manipulation and assembly of nanowires with holographic optical traps. *Optics Express*, 13(22):8906–8912, 2005.

[90] Hong Cai and Andrew W Poon. Optical manipulation and transport of microparticles on silicon nitride microring-resonator-based add–drop devices. *Optics letters*, 35(17):2855–2857, 2010.

[91] Mathieu L Juan, Maurizio Righini, and Romain Quidant. Plasmon nano-optical tweezers. *Nature Photonics*, 5(6):349–356, 2011.

[92] Helen Miller, Zhaokun Zhou, Jack Shepherd, Adam JM Wollman, and Mark C Leake. Single-molecule techniques in biophysics: a review of the progress in methods and applications. *arXiv preprint arXiv:1704.06837*, 2017.

[93] Frederick Gittes and Christoph F Schmidt. Interference model for back-focal-plane displacement detection in optical tweezers. *Optics letters*, 23(1):7–9, 1998.

[94] Ashley R Carter, Gavin M King, Theresa A Ulrich, Wayne Halsey, David Alchenberger, and Thomas T Perkins. Stabilization of an optical microscope to 0.1 nm in three dimensions. *Applied Optics*, 46(3):421–427, 2007.

[95] Frederick Gittes and Christoph F Schmidt. Signals and noise in micromechanical measurements. *Methods in cell biology*, 55:129–156, 1997.

[96] Amit D Mehta, Ronald S Rock, Matthias Rief, James A Spudich, Mark S Mooseker, and Richard E Cheney. Myosin-v is a processive actin-based motor. *Nature*, 400(6744):590–593, 1999.

[97] Michelle D Wang, Hong Yin, Robert Landick, Jeff Gelles, and Steven M Block. Stretching dna with optical tweezers. *Biophysical journal*, 72(3):1335–1346, 1997.

[98] Douglas E Smith, Sander J Tans, Steven B Smith, Shelley Grimes, Dwight L Anderson, and Carlos Bustamante. The bacteriophage ϕ29 portal motor can package dna against a large internal force. *Nature*, 413(6857):748–752, 2001.

[99] Ronald D Vale, Thomas S Reese, and Michael P Sheetz. Identification of a novel force-generating protein, kinesin, involved in microtubule-based motility. *Cell*, 42(1):39–50, 1985.

[100] Belinda Bullard, Charles Ferguson, Ave Minajeva, Mark C Leake, Mathias Gautel, Dietmar Labeit, Linlin Ding, Siegfried Labeit, Joseph Horwitz, Kevin R Leonard, et al. Association of the chaperone αb-crystallin with titin in heart muscle. *Journal of Biological Chemistry*, 279(9):7917–7924, 2004.

[101] Mark C Leake, Anika Grützner, Martina Krüger, and Wolfgang A Linke. Mechanical properties of cardiac titin's n2b-region by single-molecule atomic force spectroscopy. *Journal of structural biology*, 155(2):263–272, 2006.

[102] Keir C Neuman and Attila Nagy. Single-molecule force spectroscopy: optical tweezers, magnetic tweezers and atomic force microscopy. *Nature methods*, 5(6):491, 2008.

[103] TR Strick, D Bensimon, and V Croquette. Micro-mechanical measurement of the torsional modulus of dna. *Genetica*, 106(1-2):57–62, 1999.

[104] Jan Lipfert, Matthew Wiggin, Jacob WJ Kerssemakers, Francesco Pedaci, and Nynke H Dekker. Freely orbiting magnetic tweezers to directly monitor changes in the twist of nucleic acids. *Nature communications*, 2:439, 2011.

[105] Alfredo Celedon, Ilana M Nodelman, Bridget Wildt, Rohit Dewan, Peter Searson, Denis Wirtz, Gregory D Bowman, and Sean X Sun. Magnetic tweezers measurement of single molecule torque. *Nano letters*, 9(4):1720–1725, 2009.

[106] Jan Lipfert, Jacob WJ Kerssemakers, Tessa Jager, and Nynke H Dekker. Magnetic torque tweezers: measuring torsional stiffness in dna and reca-dna filaments. *Nature methods*, 7(12):977–980, 2010.

[107] Xander JA Janssen, Jan Lipfert, Tessa Jager, Renier Daudey, Jaap Beekman, and Nynke H Dekker. Electromagnetic torque tweezers: a versatile approach for measurement of single-molecule twist and torque. *Nano letters*, 12(7):3634–3639, 2012.

[108] Andreas R Bausch, Florian Ziemann, Alexei A Boulbitch, Ken Jacobson, and Erich Sackmann. Local measurements of viscoelastic parameters of adherent cell surfaces by magnetic bead microrheometry. *Biophysical journal*, 75(4):2038–2049, 1998.

[109] Xavier Trepat, Mireia Grabulosa, Lara Buscemi, Felix Rico, Ben Fabry, Jeffrey J Fredberg, and Ramon Farré. Oscillatory magnetic tweezers based on ferromagnetic beads and simple coaxial coils. *Review of scientific instruments*, 74(9):4012–4020, 2003.

[110] Charlie Gosse and Vincent Croquette. Magnetic tweezers: micromanipulation and force measurement at the molecular level. *Biophysical journal*, 82(6):3314–3329, 2002.

[111] G Romano, L Sacconi, M Capitanio, and FS Pavone. Force and torque measurements using magnetic micro beads for single molecule biophysics. *Optics Communications*, 215(4):323–331, 2003.

[112] Hayden Huang, Chen Y Dong, Hyuk-Sang Kwon, Jason D Sutin, Roger D Kamm, and Peter TC So. Three-dimensional cellular deformation analysis with a two-photon magnetic manipulator workstation. *Biophysical journal*, 82(4):2211–2223, 2002.

[113] Chi-Han Chiou, Yu-Yen Huang, Meng-Han Chiang, Huei-Huang Lee, and Gwo-Bin Lee. New magnetic tweezers for investigation of the mechanical properties of single dna molecules. *Nanotechnology*, 17(5):1217, 2006.

[114] Jay K Fisher, Jeremy Cribb, Kalpit V Desai, Leandra Vicci, Benjamin Wilde, Kurtis Keller, Russell M Taylor, Julian Haase, Kerry Bloom, E Timothy O'Brien, et al. Thin-foil magnetic force system for high-numerical-aperture microscopy. *Review of Scientific Instruments*, 77(2):023702, 2006.

[115] Iwijn De Vlaminck, Thomas Henighan, Marijn TJ van Loenhout, Indriati Pfeiffer, Julius Huijts, Jacob WJ Kerssemakers, Allard J Katan, Anja van Langen-Suurling, Emile van der Drift, Claire Wyman, et al. Highly parallel magnetic tweezers by targeted dna tethering. *Nano letters*, 11(12):5489–5493, 2011.

[116] Cyril Claudet and Jan Bednar. Magneto-optical tweezers built around an inverted microscope. *Applied optics*, 44(17):3454–3457, 2005.

[117] Simone Schuerle, Sandro Erni, Maarten Flink, Bradley E Kratochvil, and Bradley J Nelson. Three-dimensional magnetic manipulation of micro-and nanostructures for applications in life sciences. *IEEE transactions on magnetics*, 49(1):321–330, 2013.

[118] BP Hills. A generalized langevin equation for the angular velocity of a spherical brownian particle from fluctuating hydrodynamics. *Physica A: Statistical Mechanics and its Applications*, 80(4):360–368, 1975.

[119] U Lei, CY Yang, and KC Wu. Viscous torque on a sphere under arbitrary rotation. *Applied physics letters*, 89(18):181908, 2006.

[120] Lora Nugent-Glandorf and Thomas T Perkins. Measuring 0.1-nm motion in 1 ms in an optical microscope with differential back-focal-plane detection. *Optics letters*, 29(22):2611–2613, 2004.

[121] Matthew J Lang, Charles L Asbury, Joshua W Shaevitz, and Steven M Block. An automated two-dimensional optical force clamp for single molecule studies. *Biophysical journal*, 83(1):491–501, 2002.

[122] Mark C Leake, David Wilson, Belinda Bullard, and Robert M Simmons. The elasticity of single kettin molecules using a two-bead laser-tweezers assay. *FEBS letters*, 535(1-3):55–60, 2003.

[123] Wolfgang A Linke and Mark C Leake. Multiple sources of passive stress relaxation in muscle fibres. *Physics in medicine and biology*, 49(16):3613, 2004.

[124] Russell E Thompson, Daniel R Larson, and Watt W Webb. Precise nanometer localization analysis for individual fluorescent probes. *Biophysical journal*, 82(5):2775–2783, 2002.

[125] Hyun-Ik Kim, In-Je Joo, Seok-Ho Song, Pill-Soo Kim, Kang-Bin Im, and Cha-Hwan Oh. Dependence of the optical trapping efficiency on the ratio of the beam radius-to-the aperture radius. *Journal of the Korean Physical Society*, 43(3):348–351, 2003.

[126] Mohammed Mahamdeh, Citlali Pérez Campos, and Erik Schäffer. Under-filling trapping objectives optimizes the use of the available laser power in optical tweezers. *Optics express*, 19(12):11759–11768, 2011.

[127] Zhaokun Zhou, Helen Miller, Adam JM Wollman, and Mark C Leake. Developing a new biophysical tool to combine magneto-optical tweezers with super-resolution fluorescence microscopy. In *Photonics*, volume 2, pages 758–772. Multidisciplinary Digital Publishing Institute, 2015.

[128] Lucien P Ghislain, Neil A Switz, and Watt W Webb. Measurement of small forces using an optical trap. *Review of Scientific Instruments*, 65(9):2762–2768, 1994.

[129] Harald Felgner, Otto Müller, and Manfred Schliwa. Calibration of light forces in optical tweezers. *Applied optics*, 34(6):977–982, 1995.

[130] M Capitanio, G Romano, R Ballerini, M Giuntini, FS Pavone, D Dunlap, and L Finzi. Calibration of optical tweezers with differential interference contrast signals. *Review of Scientific Instruments*, 73(4):1687–1696, 2002.

[131] A Pralle, E-L Florin, EHK Stelzer, and JKH Hörber. Local viscosity probed by photonic force microscopy. *Applied Physics A: Materials Science & Processing*, 66:S71–S73, 1998.

[132] Stefan Maus, Susan Macmillan, Susan McLean, Brian Hamilton, A Thomson, M Nair, and C Rollins. The us/uk world magnetic model for 2010-2015. 2010.

[133] Michael Plank, George Howard Wadhams, and Mark Christian Leake. Millisecond timescale slimfield imaging and automated quantification of single fluorescent protein molecules for use in probing complex biological processes. *Integrative Biology*, 1(10):602–612, 2009.

[134] Adam JM Wollman and Mark C Leake. Single-molecule narrow-field microscopy of protein–dna binding dynamics in glucose signal transduction of live yeast cells. *Chromosome Architecture: Methods and Protocols*, pages 5–15, 2016.

[135] Helen Miller, Adam JM Wollman, and Mark C Leake. Designing a single-molecule biophysics tool for characterising dna damage for techniques that kill infectious pathogens through dna damage effects. In *Biophysics of Infection*, pages 115–127. Springer, 2016.

[136] Nathan A Tanner and Antoine M van Oijen. Chapter eleven-visualizing dna replication at the single-molecule level. *Methods in enzymology*, 475:259–278, 2010.

[137] Joseph N Zadeh, Conrad D Steenberg, Justin S Bois, Brian R Wolfe, Marshall B Pierce, Asif R Khan, Robert M Dirks, and Niles A Pierce. Nupack: analysis and design of nucleic acid systems. *Journal of computational chemistry*, 32(1):170–173, 2011.

[138] Mark C Leake, David Wilson, Mathias Gautel, and Robert M Simmons. The elasticity of single titin molecules using a two-bead optical tweezers assay. *Biophysical journal*, 87(2):1112–1135, 2004.

[139] Ricardo Henriques, Mickael Lelek, Eugenio F Fornasiero, Flavia Valtorta, Christophe Zimmer, and Musa M Mhlanga. Quickpalm: 3d real-time photoactivation nanoscopy image processing in imagej. *Nature methods*, 7(5):339–340, 2010.

[140] Eric J Rees, Miklos Erdelyi, Gabriele S Kaminski Schierle, Alex Knight, and Clemens F Kaminski. Elements of image processing in localization microscopy. *Journal of Optics*, 15(9):094012, 2013.

[141] Mark C Leake, Nicholas P Greene, Rachel M Godun, Thierry Granjon, Grant Buchanan, Shuyun Chen, Richard M Berry, Tracy Palmer, and Ben C Berks. Variable stoichiometry of the tata component of the twin-arginine protein transport system observed by in vivo single-molecule imaging. *Proceedings of the National Academy of Sciences*, 105(40):15376–15381, 2008.

[142] Nicolas J Delalez, George H Wadhams, Gabriel Rosser, Quan Xue, Mostyn T Brown, Ian M Dobbie, Richard M Berry, Mark C Leake, and Judith P Armitage. Signal-dependent turnover of the bacterial flagellar switch protein flim. *Proceedings of the National Academy of Sciences*, 107(25):11347–11351, 2010.

[143] JA Högbom. Aperture synthesis with a non-regular distribution of interferometer baselines. *Astronomy and Astrophysics Supplement Series*, 15:417, 1974.

[144] Yeonee Seol and Keir C Neuman. Single-molecule measurements of topoisomerase activity with magnetic tweezers. *Single Molecule Enzymology: Methods and Protocols*, pages 229–241, 2011.

[145] Eric C Greene, Shalom Wind, Teresa Fazio, Jason Gorman, and Mari-Liis Visnapuu. Dna curtains for high-throughput single-molecule optical imaging. *Methods in enzymology*, 472:293–315, 2010.

[146] Peter Gross, Géraldine Farge, Erwin JG Peterman, and Gijs JL Wuite. Combining optical tweezers, single-molecule fluorescence microscopy, and microfluidics for studies of dna–protein interactions. *Methods in enzymology*, 475:427–453, 2010.

[147] Jens-Christian Meiners and Stephen R Quake. Direct measurement of hydrodynamic cross correlations between two particles in an external potential. *Physical review letters*, 82(10):2211, 1999.

[148] Piero R Bianco, Laurence R Brewer, Michele Corzett, Rod Balhorn, Yin Yeh, Stephen C Kowalczykowski, and Ronald J Baskin. Processive translocation and dna unwinding by individual recbcd enzyme molecules. *Nature*, 409(6818):374–378, 2001.

[149] Paul Lebel, Aakash Basu, Florian C Oberstrass, Elsa M Tretter, and Zev Bryant. Gold rotor bead tracking for high-speed measurements of dna twist, torque and extension. *Nature methods*, 11(4):456–462, 2014.

[150] Johannes Stigler, Gamze Ö Çamdere, Douglas E Koshland, and Eric C Greene. Single-molecule imaging reveals a collapsed conformational state for dna-bound cohesin. *Cell reports*, 15(5):988–998, 2016.

[151] Justin Llandro, Dongwook Lee, Thanos Mitrelias, Justin J Palfreyman, Thomas J Hayward, Jos Cooper, JAC Bland, Crispin HW Barnes, Martin Lees, et al. Magnetic measurements of suspended functionalised ferromagnetic beads under dc applied fields. *Journal of Magnetism and Magnetic Materials*, 321(14):2129–2134, 2009.

[152] L Sacconi, G Romano, R Ballerini, M Capitanio, M De Pas, M Giuntini, D Dunlap, L Finzi, and FS Pavone. Three-dimensional magneto-optic trap for micro-object manipulation. *Optics letters*, 26(17):1359–1361, 2001.

[153] Marijn TJ van Loenhout, Iwijn De Vlaminck, Benedetta Flebus, Johan F den Blanken, Ludovit P Zweifel, Koen M Hooning, Jacob WJ Kerssemakers, and Cees Dekker. Scanning a dna molecule for bound proteins using hybrid magnetic and optical tweezers. *PLoS One*, 8(6):e65329, 2013.

[154] Anita Jannasch, Ahmet F Demirörs, Peter DJ Van Oostrum, Alfons Van Blaaderen, and Erik Schäffer. Nanonewton optical force trap employing anti-reflection coated, high-refractive-index titania microspheres. *Nature Photonics*, 6(7):469–473, 2012.

[155] MEJ Friese, AG Truscott, H Rubinsztein-Dunlop, and NR Heckenberg. Three-dimensional imaging with optical tweezers. *Applied optics*, 38(31):6597–6603, 1999.

[156] Keir C Neuman and Steven M Block. Optical trapping. *Review of scientific instruments*, 75(9):2787–2809, 2004.

[157] A Pralle, M Prummer, Ernst-Ludwig Florin, EHK Stelzer, et al. Three-dimensional high-resolution particle tracking for optical tweezers by forward scattered light. *Microscopy research and technique*, 44(5):378–386, 1999.

[158] Alexander Rohrbach and Ernst HK Stelzer. Trapping forces, force constants, and potential depths for dielectric spheres in the presence of spherical aberrations. *Applied optics*, 41(13):2494–2507, 2002.